May 2017

Spacer Casting Method for Synthesis of Magnesium Alloy Foam

Sara Karp
University of Wisconsin-Milwaukee

SPACER CASTING METHOD FOR SYNTHESIS OF A MAGNESIUM ALLOY FOAM

by

Sara C. Karp

A Thesis Submitted in

Partial Fulfillment of the

Requirements for the Degree of

Master of Science

in Engineering

at

The University of Wisconsin-Milwaukee

May 2017

ABSTRACT

SPACER CASTING METHOD FOR SYNTHESIS OF A MAGNESIUM ALLOY FOAM

by

Sara C. Karp

The University of Wisconsin-Milwaukee, 2017
Under the Supervision of Professor Pradeep Rohatgi

In this work, a new spacer material is developed for casting of magnesium AZ91D foam. An ideal spacer material should meet the following requirements, would not react with magnesium, would withstand the melting temperature of magnesium, be easy to remove, be abundantly available and cost effective, hold its shape during infiltration, and be extrudable. The material that was found to meet these requirements was a mixture of calcium carbonate and flour that went through a heat treatment to yield a porous calcium oxide structure for infiltration. The new spacer material was extrudable and easily removed without harming the magnesium foam. Magnesium foams were produced with relative densities of 0.62-0.72. The magnesium foam showed deformation behavior typical of metal foams. The magnesium foams yield stress, 19.95-57.7 MPa, exhibited an increase to a decrease in pore size. The magnesium foams showed a linear relationship between the yield stress and the calculated relative stress, indicating valid correlation of data. Microstructures of the foams showed little evidence of grain refinement in the region of the cell walls. Some dissolution of calcium from calcium oxide was observed in

the case of the smallest pore size, potentially due to the high surface area of the spacer material in that specimen.

TABLE OF CONTENTS

LIST OF FIGURES

LIST OF TABLES

LIST OF EQUATIONS

LIST OF ABBREVIATIONS

calcium carbonate ($CaCO_3$)

calcium ethoxide ($Ca(OC_2H_5)_2$)

carbon dioxide (CO_2)

densification strain (ε_d)

density of the cell wall material (ρ_s)

density of the cellular material (ρ)

differential scanning calorimetry-thermal gravimetric analysis (DSC-TGA)

energy dispersive spectrometer (EDS)

ethanol (C_2H_5OH)

gigapascals (GPa)

magnesium (Mg) or (ε)

megapascals (MPa)

$Mg_{17}Al_{12}$ (γ)

outer diameter (OD)

pascals (Pa)

plastic (peak) stress (σ_p)

plateau stress (σ_{pl})

relative density $\left(\frac{\rho}{\rho_s}\right)$,

relative stress $\left(\frac{\sigma_{pl}}{\sigma_{ys}}\right)$

scanning electron microscope (SEM)

sodium chloride (NaCl)

standard deviation (StDev)

sulfur hexafluoride (SF_6)

water (H_2O)

yield stress (σ_{ys})

ACKNOWLEDGMENTS

Thank you to my committee for their support and help throughout this research, Dr. Pradeep Rohatgi Research Advisor, Dr. Benjamin Schultz, Dr. Benjamin Church, and Dr. Joseph Aldstadt III. I appreciate all the learning opportunities and advise my committee provided.

Thank you to Ozan Emsun, SURF student for helping with preparing and running experiments. Thank you, Dr. Rohatgi research group.

I wouldn't have been able to get through this research without the support, encouragement, and help of my friends and family. Thank you to my dad, Greg Karp, Victoria Fisher, Skyler Keough, and Ryan Hansch for helping with late nights in the lab, writing, and practice presentations. Thank you for reminding me that there was more than research to focus on. Thank you, Emily Gerstein, and Alexis Cera for taking on more responsibility with American Foundry Society UWM Student Chapter so that I could focus on completing my research.

CHAPTER ONE: INTRODUCTION

1.1 INTRODUCTION

Metal foams are a unique class of a hybrid materials that exhibit reduced weight, increased dampening capacity, and increased specific mechanical properties. Their properties are tailorable through a combination of material selection and pore size shape, orientation, and volume control. Magnesium foams are of special interest due to the ultra-light capability. Unfortunately industrially viable process of producing a tailorable magnesium foam structures are lacking. The development of new, low cost process to produce tailorable metal foam is essential for a successful wide spread implementation of metal foams.

1.2 RESEARCH GOAL

The goal of this research was to develop a spacer material that could be used for creating a controlled open cell structure for magnesium foams by an infiltration casting technique. The spacer material should be easy to remove without damaging the magnesium structure. In order for this novel spacer material to function it must:

1. Be non-reactive with magnesium.
2. Withstand the melting temperature of magnesium (680ºC)
3. Be easily removed.
4. Be abundant enough for easy sourcing and cost effective to use.
5. Hold its shape while being infiltrated with magnesium.
6. Be extrudable, allowing for conventual industrial scale production of desired shapes

If successful, this material and methodology could be implemented via additive manufacturing to create complex shapes not attainable through the current materials and process.

1.3 THESIS ORGANIZATION

This thesis begins with a short introduction on metal foams and open cell foams that explores the current stat of the art in producing magnesium foams. The sections are as follows: background, materials, results and discussion, conclusion, and future research. The research is broken into three main research aspects: the spacer material creation, dissolving study of the spacer material, and the magnesium foam product.

CHAPTER TWO: LITERATURE REVIEW

2.1 BACKGROUND

Metal foams are a class of metallic materials that derive their unique properties from their highly porous structure. Making an alloy into a metal foam can lead to an increase in specific characteristics such as compressive strength, vibration dampening capacity, heat transfer, and energy absorption. Metal foams are also significantly less dense when compared to the solid ingot. Due to their unique structure and properties metal foams are attractive candidates in automotive, transportation, aerospace, biomedical and water treatment industries, among others.

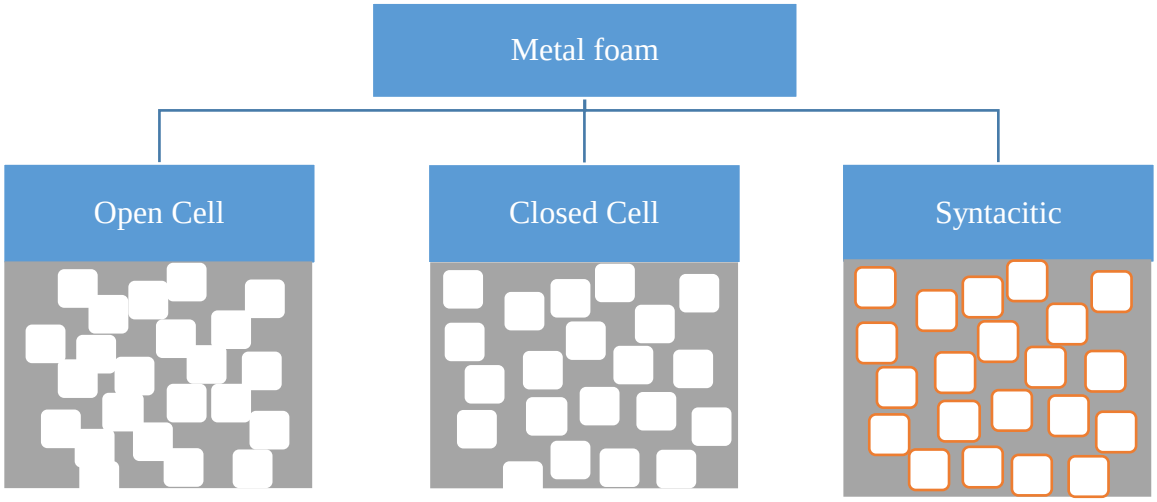

Figure 1: Schematic diagram of the different types of metal foams.

There are three main types of metal foams and each yields a different type of structure. The three different types of foams also have slightly different properties due to the design of the pores and the process used to make those pores (Ashby, et al., 2000). The three types of metal foams are syntactic, open cell, and closed cell foams, see Figure 1. By controlling the pores type, size, orientation, and material one can tailor the mechanical properties of the foam to a specific application.

2.1.1 CLOSED CELL FOAMS

Closed cell foam can be made from a variety of methods such as melt gas injection, gas releasing particle decomposition in the melt, gas-releasing particle decomposition in semi-solids, and gas entrapment expansion. To create a closed cell foam, the alloy chosen to be melted needs to have a high viscosity and a low reaction rate with gases, such as hydrogen and oxygen (Gupta, 2015). A low reaction rate to common gases, i.e. magnesium reacts violently with oxygen when in its liquid state and aluminum does not, is needed due to the previous stated methods of creating a closed cell foam involve producing or forcing a gas through the melt. Melt gas injection method involves injecting a gas into the melt creating bubbles. The foamed metal is then drained from furnace and allowed to solidify. Gas releasing particle decomposition in a melt and gas-releasing particle decomposition in a semi-solid are similar processes that introduces a material that vaporizes at a high temperature to create a gas inside of the alloy melt. With the application of pressure during the solidification period the final product is a metal foam. The main difference between the gas-releasing particle decomposition in a melt and the gas-releasing particle decomposition in semi-solids is the temperature at which the melt is brought to before solidification occurs. Gas entrapment methods is a powder metallurgy technique that use an inert gas pressure chamber that contains a mixture of metal powder and spacer material. When heated the spacer material is vaporized creating a pore. The foam is cold rolled after this process to create uniformity in the structure.

2.1.2 SYNTACTIC FOAMS

Syntactic foams are made by co-compaction process. In this process, a bed of leachable particles are infiltrated via pressure or stirred into an alloy melt. This leads to a closed pore system with reinforced cell walls. A variety of potential materials can be used to reinforce the

cell shape and change the properties of classic metal foams. This can create a longer plateau region and an increase in the impact energy the metal foam can absorb.

2.1.3 OPEN CELL FOAMS

Open cell foams are commonly formed using a polymer or precursor as a template, metal deposition on cellular preforms, and co-compaction of two materials. The polymer or precursor process involves coating the polymer or wax with a ceramic coating and then pressure infiltrating the melted alloy around the preform. After solidification, the preform material is knocked out of the metal. In metal deposition on a cellular preform a metal vapor is introduced into a closed heated system with a preform. The system is cooled condensing the metal vapor on to the preform. The preform is then melted out leaving an open cell metal. In the co-compaction of two materials a leachable material is interconnected via a sintering process and then liquid metal is poured or pressure infiltrated into the leachable material. Once the metal has solidified the leachable material is removed via dissolving or impact vibrations.

2.1.4 CHARACTERIZATION AND PROPERTIES

Classic metallography techniques can be used to characterize the structure, shape, cell size, microstructure, and composition of a metal foam. For closed cell foams scanning electron microscope (SEM) may lead to inaccurate energy dispersive spectrometer (EDS) results due to the porous structure of the material.

When compression testing a prism or cylinder shape a height to diameter ratio of around 1.5 is considered ideal (Ashby, et al., 2000) although there is research that shows that a ratio as low as one also is acceptable for testing (Gupta, 2015). Compression testing yields a stress strain

graph with a plateau region and is generally ended once the densification point has become equal to the peak stress, see Figure 2.

The compression curves for metal foams have four main points of interest, the plastic

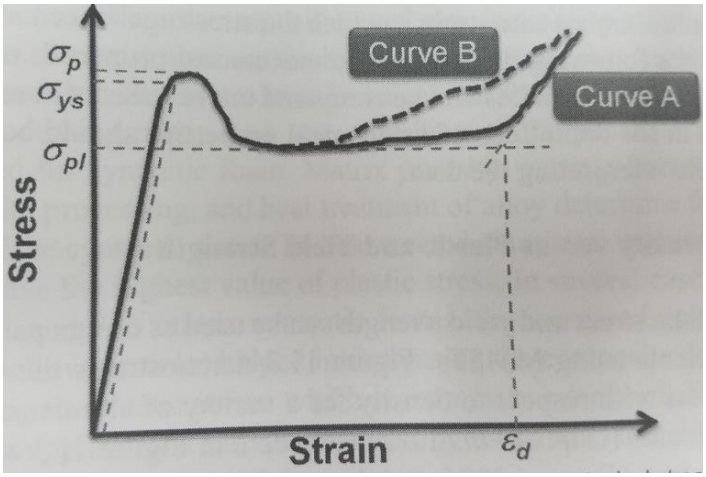

Figure 2: Ideal metal foam compression stress-strain curve (curve A) and a poorly defined plateau region stress strain curve (curve B). This image was taken from (Gupta, 2015)p.309

(peak) stress (σ_p), yield stress (σ_{ys}), plateau stress (σ_{pl}), and densification strain (ε_d). The plateau region is what makes metal foams unique in compression testing. This region is where foams absorb the most energy. The densification strain is dependent on the total porosity in a sample. The densification strain can be considered where the linear trend line of densification intersects the plateau stress line (Figure 2) or as being equal to the peak stress.

The relative stress $\frac{\sigma_{pl}}{\sigma_{ys}}$, and the relative density $\frac{\rho}{\rho_s}$, (ρ=density of the cellular material and ρ_s= density of the cell wall material) have a power relationship, as shown in Equation 1.

Equation 1: Relative stress and relative density relation. C is a constant that is equal to 0.3 for cellular metals. (Yamada, et al., 1999)

$$\frac{\sigma_{pl}}{\sigma_{ys}} = C \times \left(\frac{\rho}{\rho_s}\right)^{\frac{3}{2}}$$

When yield stress, vs calculated relative stress (Equation 1) is graphed a linear relationship should be observed due to the dependence yield stress has on the relative density. This is a way to determine if the data has a valid correlation, (Zhang, Li, Li, & Sun, 2014).

The dampening capacity of metal foams tends to be five to ten times larger than the metal they originate from due to the cell wall compression, increase surface area, and densification properties (Ashby, et al., 2000). The specific heat, melting temperature, and expansion coefficient of the metal foams are the same as the base material they are made of (Ashby, et al., 2000). The thermal conductivity and resistivity of a metal foam are different from the base metal and are related to the relative density of the foam via a power relationship. The density of the metal foam greatly effects several of the mechanical properties. As the density of a foam increases the Young's modulus, and compressive strength will increase as well (Ashby, et al., 2000).

2.2 MAGNESIUM OPEN CELL FOAMS

Due to magnesium's attractive mechanical properties it has drawn of interest as a candidate material for the development of a metal foam. The most difficult aspect to overcome with magnesium for creating a metal foam is its high chemical reactivity. This severely limits the processes that may be used to produce a magnesium metal foam due to most current metal foam production leading to exposer to reactive materials and corrosive chemicals.

2.2.1 SINTERING METALLURGY

C.E. Wen and fellow researchers studied the compressibility of a powder metallurgy technique producing an open cell foam. The magnesium foam was produced by sintering a mixture of pure magnesium powder and carbamide particle spacers. The carbamide particles

were vaporized during the sintering process to create an average magnesium foam porosity of 33-55%.

The research yielded a mostly open cell structure and some closed cell pores were found. The closed cell nature of the foam increased with decreasing porosity. The Young's modulus and peak stress increased with a decrease in porosity (Wen, et al., 2004). The highest peak stress measured was 16-17 MPa. The researchers did find carbon residue on the cell walls of the structure left by the spacer material. The focus of the research was to determine if the magnesium foam has the mechanical properties to be a potential bone scaffolding and the conclusion was that magnesium foams would be a valid metal foam for bone scaffolding.

Hao, Han, and Li researched a similar powder metallurgy and carbamide rounded particle spacers in 2008. The residue carbon was reduced by dissolving the carbamide out of the magnesium after green compaction. The percent porosity of the foams was calculated using Equation 2

Equation 2: Percent porosity calculation ρ_f is the porosity of the foam and P_a is the percent porosity of the foam. (Hao, Han, & Li, 2009)

$$P_a = \left(1 - \frac{\rho_f}{1.74}\right) \times 100$$

Hao and associates found a relationship of the elastic limit stress and the plateau height are directly correlated and that these two mechanical properties appeared to be independent of the pore size. The magnesium foam that was created was brittle in nature which can be determined from the serrated plateau region of the stress-strain curve (Hao, Han, & Li, 2009). The longer the strain range of the plateau region of the stress-strain curve indicates a higher ductility in the foam.

Powder metallurgically formed samples are known for having decreased mechanical properties compared to cast metal foams, due the oxide layer that forms on the powder metal during manufacturing and sintering. Hao and coworkers tried to reduce this effect by breaking some of the oxide layer during the green compaction phase of the process. Hao and coworkers compacted the samples with 300 MPa verses the 100 MPa that C.E. Wen and companions used. A success or failure of this technique was not confirmed.

Zhang, et. al developed a different sintering technique for creating an open cell foam by using magnesium ribbon and no spacer material in 2012. Magnesium ribbon was orientated in a specific pattern and hot pressed to be sintered together. This created a uniform cell wall and structure. The Young's modulus of the structure averaged to be 0.1-0.37 GPa, which is significantly lower than then what was found for conventional powder metallurgy methods (Wen, et al., 2004) who observed a Young's modulus pf 1.3-1.8 GPa.

Solid metal sintering techniques run into several issues with regards to the final structures produced. In the case of powder metallurgy, the biggest concern is that the oxide layer that naturally forms on the particle and prevents a true metallurgical bond, weakening the overall mechanical properties, The concern with spacer materials is the residue that can be left behind or the reaction of the spacer material with the magnesium.

2.2.2 FOAMING

Haibin, Gueangchun, and Hongbin created an open cell magnesium foam by foaming a magnesium melt with calcium, titanium hydride, and powder aluminum in 2007. The aluminum and calcium were added to the process to help prevent magnesium from oxidizing and increase the viscosity of the melt. The melt process was done completely under argon gas to prevent the ignition of magnesium and the titanium hydride is the foaming agent. The foaming method

created a magnesium foam and had rupture bubbles after foaming for 3 minutes (Haibin, Guangchun, & Hongbin, 2007). This pore size in this process was not controllable beyond prevention of bubble rupture and mechanical testing was not done on the foam. The concern with foaming is that the pore size and orientation cannot be controlled. This can lead to a variety of pore sizes and an open cell, closed cell or mixed cell foam structure.

2.2.3 INFILTRATION OF SPACER MATERIAL

One of the first magnesium foams developed via infiltration spacer material method was with a polyurethane spacer. This method creates an open cell structure with cell walls of 0.35-4.5 mm. This was researched by many different groups in 1999 through 2001. A polyurethane spacer was created and has a ceramic coating placed on it. The magnesium was then poured around the ceramic. After solidifying the ceramic was knocked out via vibrations. This can leave a residue of ceramic left in the cell walls.

Kirkland and associates magnesium foam was created with a sodium chloride spacer from vacuum infiltration process. The sodium chloride is removed by a sodium hydroxide solution to reduce the degradation of magnesium during sodium chloride's ionization (Kirkland, Kolbeinsson, Woodfield, & Staiger, 2011). The pore structure generated using rapid prototyping structure that had a sodium chloride paste filled structure. The polymer was then burned out and sodium chloride was sintered. Magnesium was then infiltrated into the sodium chloride using pressure infiltration methods. The cell wall uniformity and pore size and shape were dependent on the original particle size of the sodium chloride and sinter time of the sodium chloride.

A pressure infiltration method that mimics investment casting processes was investigated by Yue and Hur. The spacer material that was used was a mixture of salt, plaster, and pearlite powder with polyvinyl acetate as a binder. This mixture was made into 1.70 to 3.36 mm

diameter spheres. These granules were removed from the magnesium by running water and air through the pore structure. The magnesium was cast while under a sulfur hexafluoride, SF_6 and carbon dioxide, CO_2, atmosphere. They found that the ideal pressure for infiltration for the fluidity of magnesium is 6000 Pa (Yue & Hur, 2012). Running water over magnesium can be an issue due the high reactivity of magnesium in water. Water can also be used as an etchant for magnesium making water less than ideal as a dissolving fluid.

Jiang and He used titanium wire as the spacer material for the magnesium foam they developed. Magnesium was melted and the titanium wire was aligned and dipped into the magnesium melt while ultrasonic vibrations were applied. The vibrations helped to infiltrate the magnesium into the spaces between the titanium wire. The wire bundle was then slowly pulled from the melt under a controlled atmosphere. To remove the titanium the casting was submerged in 40% hydrofluoric solution. The dissolving process for removal of the titanium wire took 72 hours. Due to this type of dissolving, a layer of magnesium difluoride was formed on the magnesium foam. The Young's modulus of the material ranged from 0.5-1 GPa (Jiang & He, 2014). The magnesium foam did not show an elongated stress plateau region when tested in compression, indicating that the foam will not be able to absorb energy as well as some of the previous foams discussed.

Also in 2014 Wang and researchers created a magnesium foam by mixing flour and sodium chloride together into a pellet and then vaporizing the flour while sintering the sodium chloride. The magnesium was then infiltrated around the salt preform. Finally the salt was dissolved out with 0.001M sodium hydroxide. The group did not report the pH of the solution after solution of the salt and did not report any evidence of corrosion of the magnesium specimen. Wang at al observed both macroscopic and microscopic infiltrations, where the

magnesium not only filled spaces between the spheres but also infiltrated pores within the sintered sodium chloride spheres (voids remaining after vaporization of the flour). The compressive yield strength of the foams ranged from 3.57 to 8.65 MPa (Wang, Li, Haung, Wang, & Han, 2014).

Sodium hydroxide tends to be the solution of choice for dissolving out sodium chloride due to its low reactivity with magnesium. There are several studies investigated the effects of sodium chloride on the corrosion of magnesium, however most of the reported literature on magnesium foams produced using sodium chloride spacers do not report observations of reaction of the magnesium with chloride ions. Often the corrosive behavior of magnesium is tested using a sodium chloride solution of various strengths (Guohua, Fan, Gao, Zhai, & Zhu, 2005). These studies suggest that sodium chloride may not in fact be an ideal spacer material for the production of magnesium foams commercially.

2.2.4 APPLICATIONS OF MAGNESIUM FOAM

Magnesium foams are attractive materials for the automotive, transportation, and aerospace industries due to their light weight and tailorable mechanical properties. In particular, their high energy absorption in compression, and vibration damping capabilities make them ideally suitable for panels, frame elements and crash-box structures. These materials can lead to improved fuel economy, safety, and comfort in the transportation sector. The elongated stress plateau that most magnesium foams exhibit indicates that these materials can absorb more energy at lower loads at a reduced weight (Mukai, et al., 1999). It has also been shown that the yield stress of magnesium foams is directly related to the strain rate in compression, suggesting that the high strain rates exhibited during a crash or blast event would lead to an increase in the yield stress (Mukai, et al., 1999). This could lead to improved crashworthiness of components in

the aerospace, automotive, and transportation industries. Kanahashi et al. found that solutionizing and aging heat treatments reduced the strain rate dependence of Mg-AZ91D foams, allowing for more consistent properties over a wide range of strain rates (Kananhashi, et al., 2001).

Magnesium foams have also been investigated as a potential material for orthopedic implants. Magnesium is a promising system for development of biodegradable alloys as the human body can tolerate a larger amount of Mg ions released into the surrounding tissues than Fe or Zn, which are other common candidates for biodegradable metal alloys. Magnesium foam bone scaffolds have been investigated by several researchers, as the Young's modulus of cancellous bone is 0.01-2 GPa and 0.2-80 MPa, which is in the range of the mechanical properties for magnesium foam (Wen, et al., 2004). Being able to create a bone scaffold close to the mechanical properties of bone would yield less stress concentration in the bone due to the implant, and potentially a faster recovery time for patients. Depending on the alloy chemistry and the morphology of the implant, implants can last from weeks to months allowing for trauma to heal safely.

CHAPTER THREE: EXPERIMENTAL METHODS AND PROCEDURES

3.1 CALCIUM CARBONATE SPACER MATERIAL

A 1:3 weight ratio of semolina flour to calcium carbonate was mixed with 26 mL of deionized water using a Resodyn Acoustic Mixer LABRAM at a frequency of 61 Hz and acceleration of 90 Gs, for 20 minutes. This ratio was developed by adding calcium carbonate to flour and deionized water mixture and qualitatively evaluating the mixture's "workability". One gram of calcium carbonate was added at a time to the flour-water mixture until the green strength of the dough made it too brittle for the subsequent extrusion process. Once one gram of calcium carbonate was added to the mixture, the mixture was mixed at the same frequency and acceleration stated above for two minutes and then the container was flipped 180-degrees and mixed for an additional two minutes to ensure the calcium carbonate was evenly dispersed in the mixture. Water was added into the dough mixture as needed.

Once the dough was made it was extruded into a noodle form using a manual Marcato Atlas Wellness 150 Pasta Machine. The hydrated mixture was run through the rolling extrude three times to achieve a thickness of approximately 4.8mm and then either rolled through the cutting die at 6.35mm or 1.58 mm, which also decreased the thickness of the samples to 2.03 mm or 1.52 mm respectively. The noodles were then cut to create three different spacer sizes (Figure 3). The three cross-sectional areas of the noodle sizes were:

- 6.35mm X 6.35mm (large)
- 6.35mm X 3.175mm (medium)

- 3.175mm X 1.58mm (small)

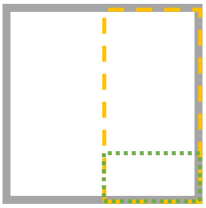

Figure 3: The sample sizes in relation to each other. The gray box represents the large sample, the yellow the medium and the small the green.

Once cut, the noodles were placed on a clean baking sheet in a furnace at 70 °C for an hour to dry before storing. If not properly dried and stored the noodles would mold and become unusable.

The flour, calcium carbonate powder and resulting mixture was tested via differential scanning calorimetry-thermal gravimetric analysis (DSC-TGA) using a TA Instruments SDT2960. An alumina crucible for each type of sample was used to measure out a small amount of flour, calcium carbonate, and the dried mixture (coarsely crushed). The samples were run at a ramp of 10ºC/min under normal air atmosphere, carbon dioxide atmosphere, and air/CO_2 switched atmosphere to determine when phase transitions occurred and how the flour effects the transformation of calcium carbonate to calcium oxide.

To create the spacer, shape the noodles were misted with deionized water to temporarily rehydrate them. This allowed for a slurry to form between the noodles of $CaCO_3$ and water to create an initial adherence between the noodles. The rehydrated noodles were placed into an alumina cylinder with a kaowool stopper to be heat treated, see Figure 4.

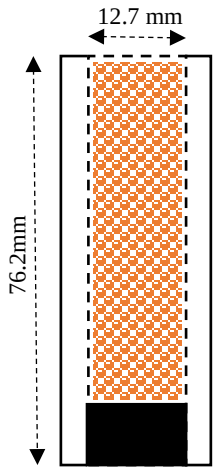

Figure 4: Alumina tube with graphite or Kaowool stopper (black) and spacer material (orange) set up for sintering.

The assembly shown in Figure 4 was then brought to 755°C for 5 hours to burn off the flour, dry the noodles, and create a bond between the noodle particles. During the 5 hours at 755°C the calcium carbonate formed calcium oxide, see Equation 3. The furnace set up can be seen below in Figure 5.

Equation 3: Calcium Carbonate decomposition reaction.

$$CaCO_3 \rightarrow CaO + CO_2$$

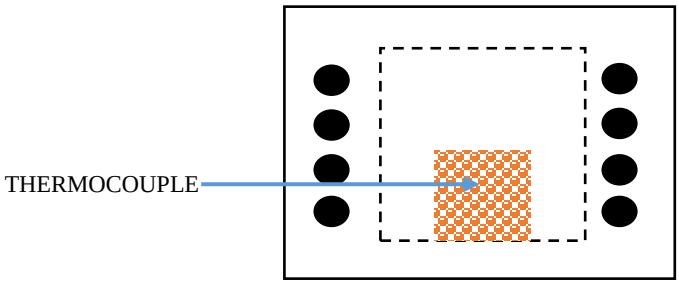

Figure 5: Sinter furnace set up, the orange pattern represents the sample, the white block beneath represents alumina used to prop the sample into the hot zone of the furnace.

The noodles do not sinter together because the process is not under CO_2 gas. The water from rehydration creates a slurry that loosens some of the $CaCO_3$ particles and hydrates the flour proteins to create an adherence layer between the noodles. Once the water and flour are burned out the noodles are held together by electrostatic adherence (Figure 6 through Figure 8). Due to the electrostatic nature of the adherence the bond is strong enough to survive infiltration but one

must be careful when working with the samples as they are fragile. Once cooled the samples were transferred to a steel tube for magnesium infiltration.

Figure 6: Large spacer material after heat treatment.

Figure 7: Medium spacer material after heat treatment.

Figure 8:Small spacer material after heat treatment.

3.2 MAGNESIUM FOAM INFILTRATION

A threaded steel pipe with one end closed via a cap was used as the mold for infiltration of the CaO preforms with magnesium as shown schematically in Figure 9. The steel pipe was cleaned and the inside was coated with graphite. The void created by the cap pipe fitting was filled with kaowool sandwiched between two clean steel washers. The cap inset was then sprayed with graphite to prevent the magnesium from infiltrating into the threads of the cap and to prevent the magnesium from infiltrating into the threads of the cap and to prevent the

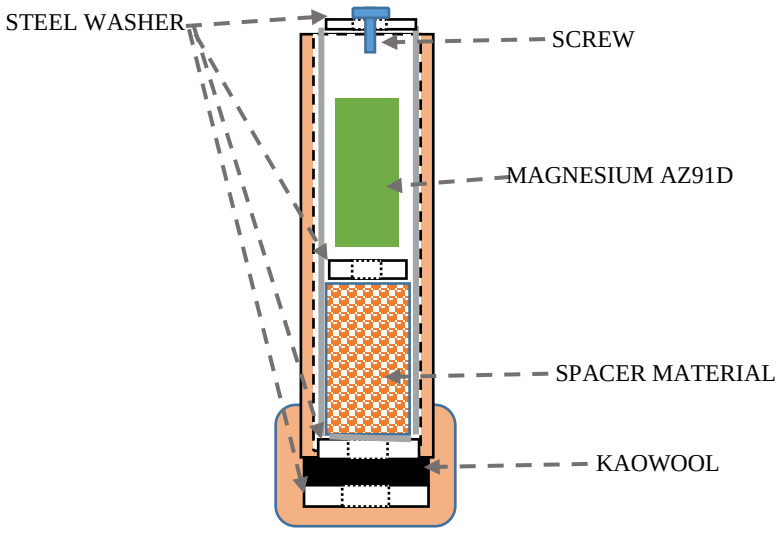

Figure 9: Setup of steel tube with steel cab for near vacuum infiltration.

magnesium from sticking to the cap during removal. The cap was put onto the tube and screwed tight. The spacer material was then carefully placed into the tube. A steel washer was placed on top of the spacer material to help break up the oxides of the metal during infiltration. An ingot of magnesium AZ91D was placed on top of the steel washer and an additional steel washer and screw were up on top of the steel pipe to act as a chill to evaporate magnesium. The full assembly can be seen in Figure 9. Care was taken to reduce the amount of time the magnesium was held in the molten state as it was found to condensate on the chill can be shown in Figure 10. The nominal composition of AZ91D consist of 0.35-1% zinc, 8.3-9.7% aluminum, and balance magnesium.

Figure 10: Condensed magnesium on chill system for infiltration process.

The assembly was hung in a vertical quartz tube processing chamber so that the steel tube would be in the hot zone of the furnace. The infiltration equipment is shown schematically in Figure 11. The chamber is first evacuated with a roughing pump to approximately 10^{-3} Torr while the furnace was ramped to 680°C and held for 30 minutes. After the allotted time, the vacuum valve was shut and argon gas was released into the process chamber at an initial pressure of 517 Torr to infiltrate the preform. To cool the specimen, furnace was turned off, and the quartz process chamber was lifted from the furnace. Samples were pressed out of the steel tubes

and then treated to remove the CaO. The steel tubes and caps could be reused after cleaning and recoating with graphite spray.

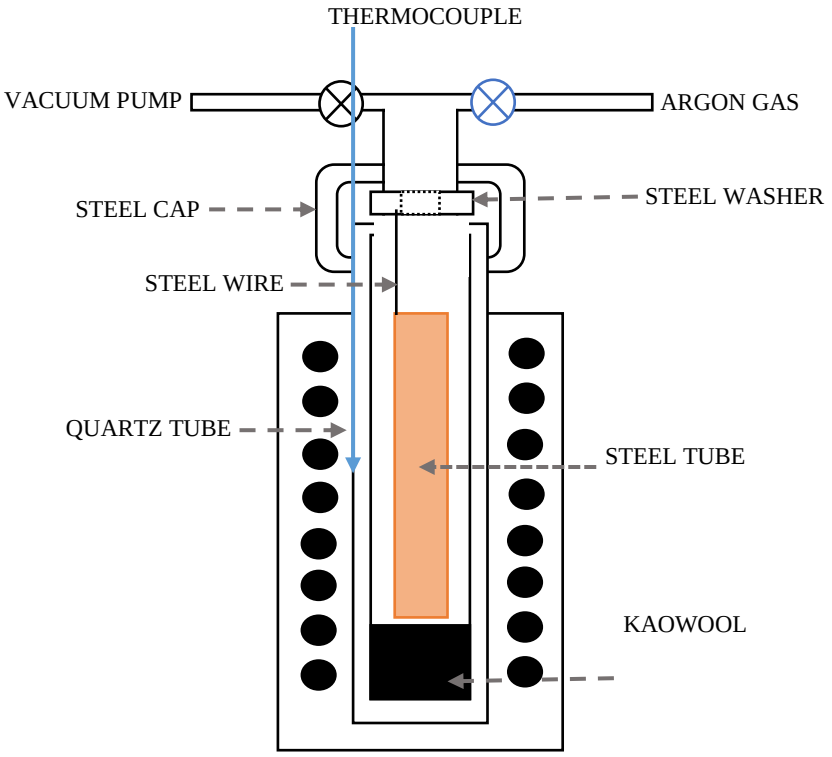

Figure 11: Near Vacuum infiltration tube furnace setup.

3.3 DISSOLVING

The magnesium foam samples were machined to the size needed for compression testing prior to dissolving, by using a lathe. The spacer material did not sit in the center of the tube which caused excess porosity on the edges of some of the samples making samples, causing samples to break during machining. Foams with medium size pores had excessive surface porosity making machining difficult and therefore the outer cast surfaces were not machined. Specimens of the solid cast magnesium, as well as simple tube shaped magnesium were also machined for comparison. Magnesium tubes were produced with inner and outer diameter dimensions of 6.35 mm and 12.7 mm respectively. Specimens with an L/D ratio of 1 were machined for each specimen type, with diameters ranging from 12.7 mm to 14.3 mm. Care was taken to ensure that the ends of the specimen were parallel. Due to the brittle nature of the CaO

preform, mechanical vibrations during removal from the casting setup and subsequent machining caused a portion of the spacer material to break and fall out.

To remove the rest of the CaO the sample was placed in ethanol. MgAZ91 does not react with high purity ethanol readily. CaO on the other hand does react with ethanol readily, see Equation 4. Equation 6 was expected reaction to occur with ethanol and calcium oxide.

$$CaO + 2C_2H_5OH \rightarrow Ca(OC_2H_5)_2 + H_2O$$

Equation 4: Calcium oxide reaction with ethanol.

To offset the acid being created at least four times the moles of calcium ethoxide, $Ca(OC_2H_5)_2$, needs to be added in addition to the ethanol to react the CaO, which is a 2:1 mol ratio of C_2H_5OH:CaO. The samples were submerged in ethanol, C_2H_5OH, (100mL) with a stir rod and no additional heat was added, see Figure 12.

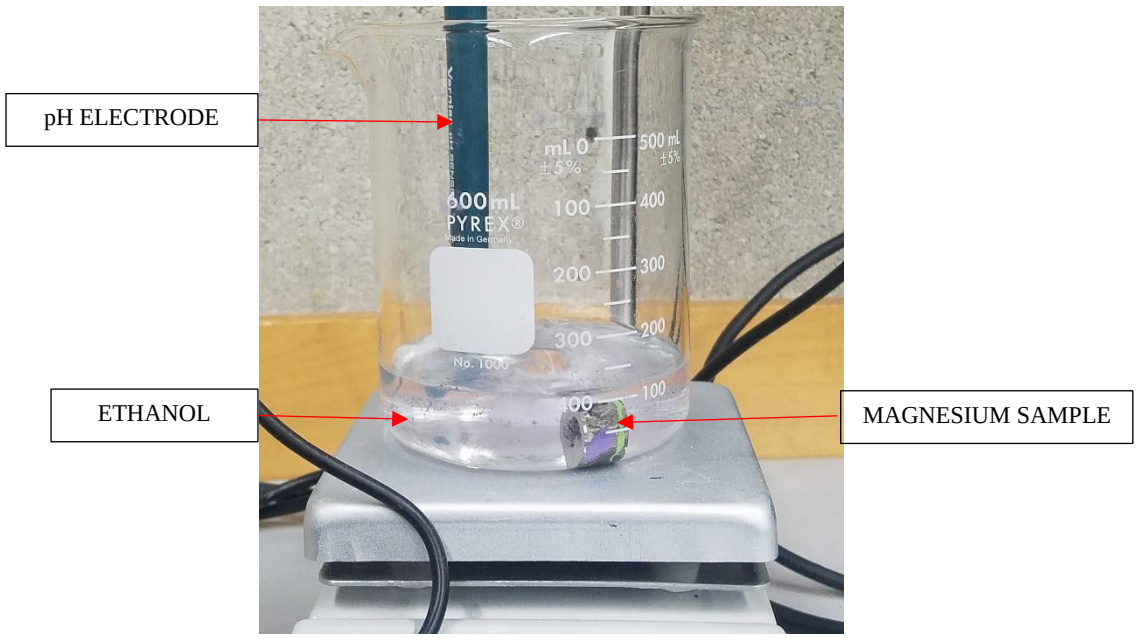

Figure 12: Stir plate spacer dissolving set up.

After the pH had stabilized the samples were pulled out to dry. Dry compressed air was used to blow through the open cell structure to push out any potential residue from the spacer

material from the dissolving process. This process with the stir plate was used on the medium samples and took an average of 8 hours.

Once the pH change was understood from the above process, the samples were put into a sealed container and placed in the acoustic mixer as shown in Figure 13,with a frequency of 61Hz and acceleration of 25 Gs, for 15-60 minutes to dissolve and break out the spacer material without causing damage to the magnesium foam.

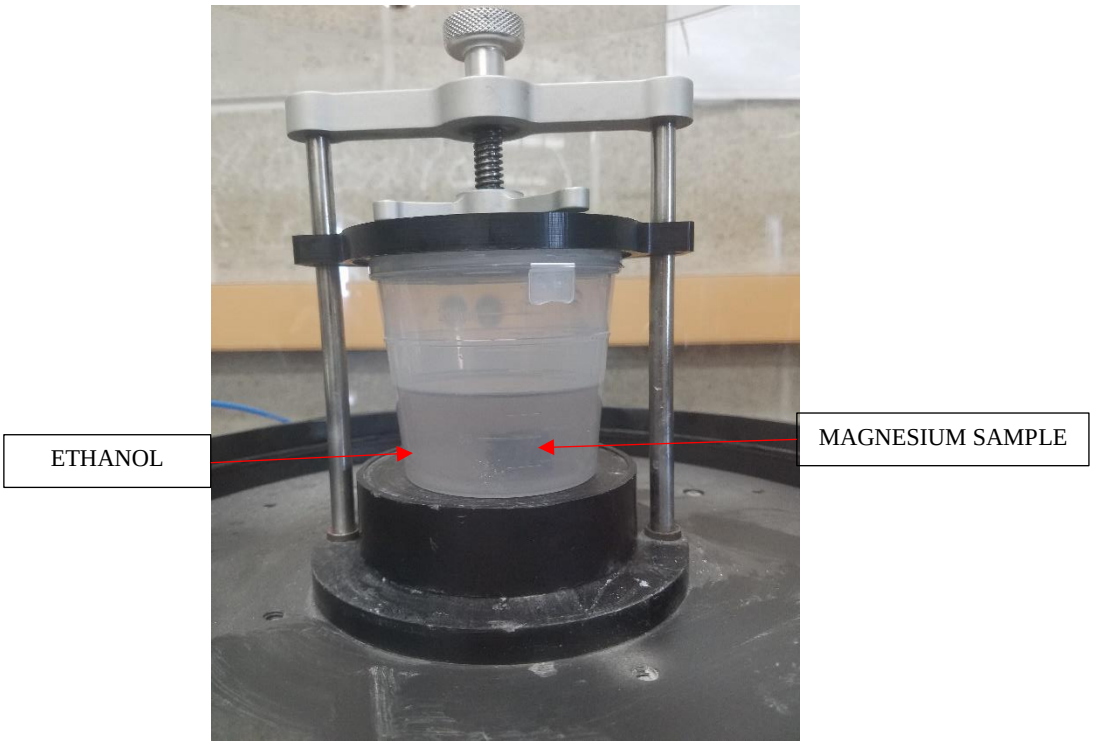

Figure 13: Acoustic mixer spacer dissolving set up.

3.4 MECHANICAL TESTING

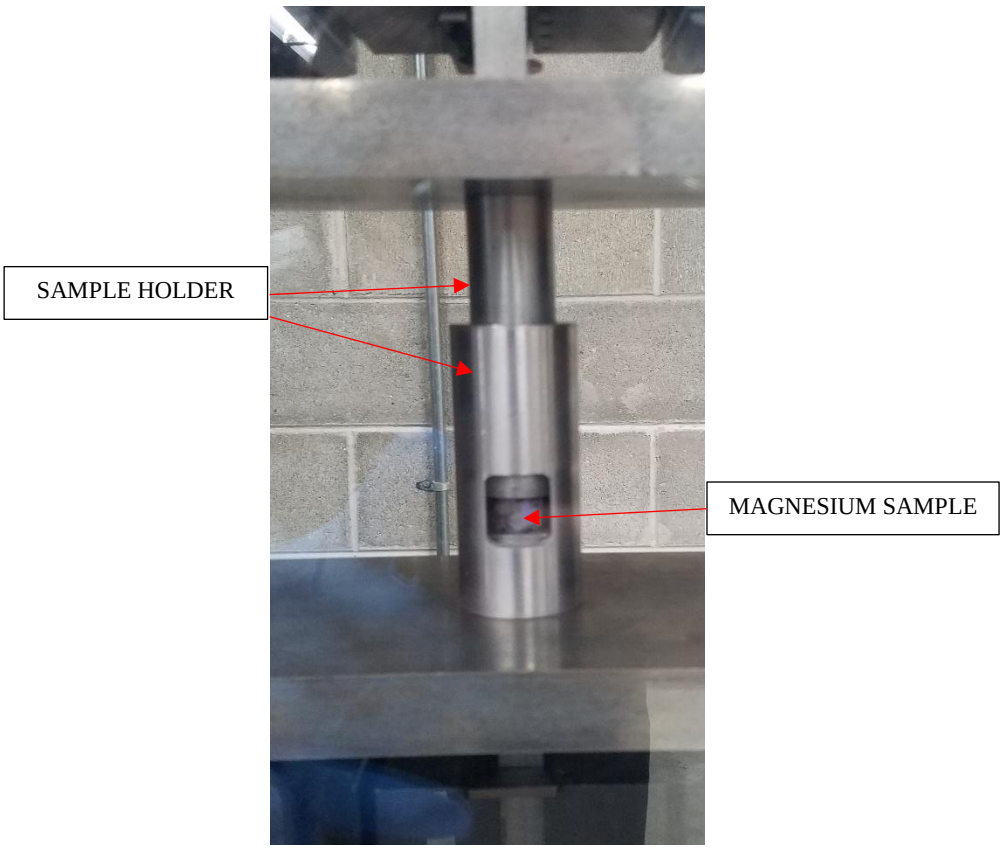

Figure 14: Compression Testing setup.

The samples were then compression tested using an Instron 250kN universal testing system. A compression fixture was used to ensure alignment between the top and bottom platen against the specimen for the duration of the test. The samples were placed into the center of the fixture as shown in Figure 14. The samples were compression tested at a strain rate of $10^{-3}\ ^{1}/_{sec}$. Figure 15 and Figure 16 show the medium sample before and after the compression testing respectively.

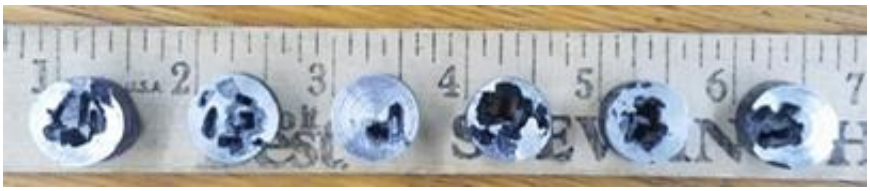

Figure 15:Medium pore size samples before compression.

Figure 16: Compressed medium pore size samples

Samples from the large, medium, and small spacer size, solid cast magnesium, and the tube cast magnesium were cut and mounted into thermoplastic molds. These samples then were ground and polished using 320, 400, 800, and 1200 grit SiC paper from Buehler. The samples were polished using a white silk pad with 1 µm diamond slurry from PACE Industries. During the grinding and polishing the samples were cleaned in the ultrasonic bath submerged in Sigma Aldrich ethanol 99.5% purity. The samples were then air dried. The etchant used was 150 mL ethanol, 50 mL deionized water and 1 mL glacier acetic acid. The samples were held submerged in the etchant solution for 45-120 seconds with slight agitation, rinsed with ethanol, and dried using an air gun (Maltais, Dube, Fiset, Laroche, & Turgeon, 2004). Once etched the macroscopic structure of the foams was examined with a Zeiss Stemi2000-S stereomicroscope and the microstructure was observed under polarized light AX10-Zeiss Optical Microscope. The grain

size was determined with the optical microscope using classic line intersection calculations. Phase chemistries were evaluated using JEOL JSM-6460 LV scanning electron microscope with energy dispersive spectrometer.

CHAPTER FOUR: RESULTS AND DISCUSSION

4.1 CALCIUM CARBONATE SPACER MATERIAL

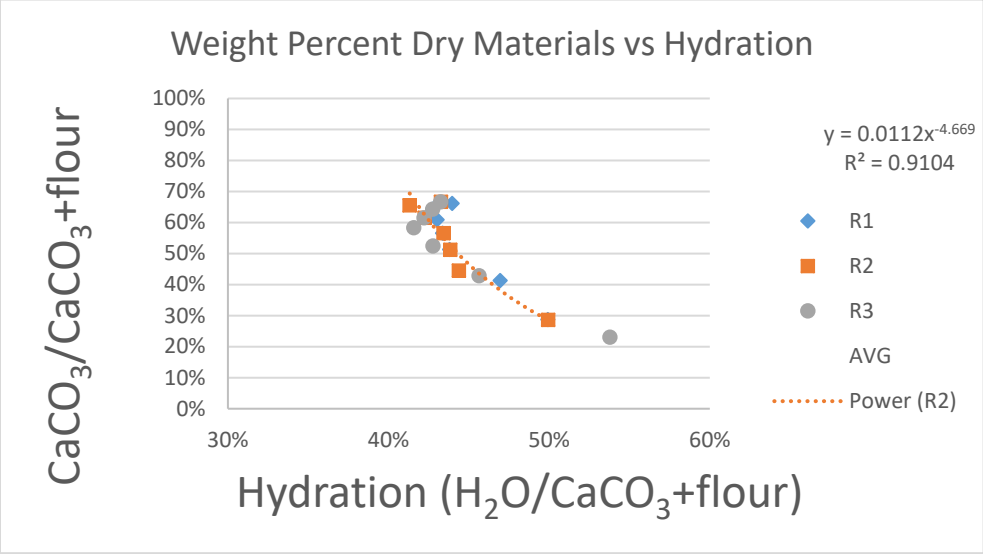

Figure 17: $CaCO_3/CaCO_3$+Flour vs percent hydration of noodles.

It was found that above the 1:3 ratio of flour to calcium carbonate the dough did not retain enough of its plastic and elastic properties to be extruded through the noodle maker. The above graph (Figure 17) shows the ratio of the dry to wet components of the dough. At this ratio tearing is already occurring at approximately 50% hydration as visible in Figure 18.

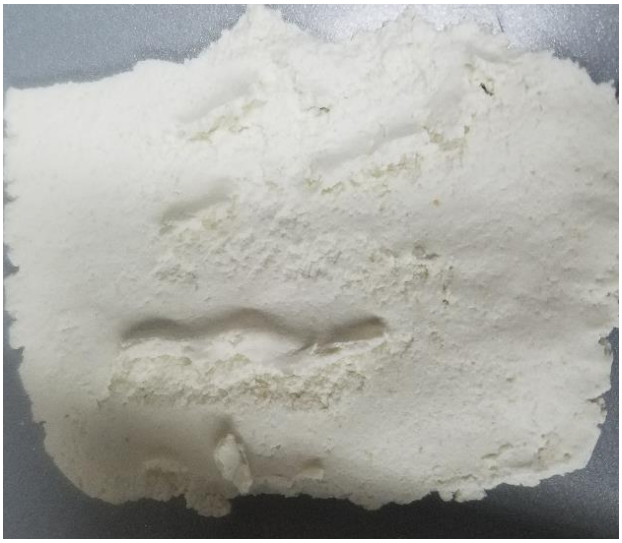

Figure 18: $CaCO_3$ dough after being passed through the smooth roller of the noodle maker once.

Table 1 below, shows that having flour and calcium carbonate mixed together changes the temperature for conversion in the carbon degradation in the flour and the formation of calcium oxide and carbon dioxide for the calcium carbonate degradation. This could be a result of the composite mixture acting as an impurity which can reduce the temperature of transformation.

Table 1: The first derevative of the weight/time from the DSC-TGA. The table shows the temperature for the reaction changes for the varity of samples tested in air atmosphere.

	dWt%/dt Temperature (°C)				
Sample type		Water Evaporated	Flour to Carbon	Carbon Degradation	$CaCO_3 \rightarrow CaO + CO_2$
Flour (powder)	Average	77	304	497	N/A
	StDev	8	0.4	3	N/A
$CaCO_3$ (powder)	Average	N/A	N/A	N/A	812.71
	StDev	N/A	N/A	N/A	4
Flour-$CaCO_3$	Average	86	305	468	789
	StDev	3	0.2	4	0.5

Flour is bonded together via a variety of covalent bonds that are activated when water is introduced to the glutenin-to-gliadin chains (Wieser, 2007). Once hydrate gliadin is responsible for the viscosity and extensibility and glutenin is responsible for the cohesive and elastic properties of the dough. The calcium carbonate gets distributed throughout the glutenin-to-gliadin chains. This weakens the chains and decreases the elastic and plastic mechanical properties of the dough. Increasing the amount of water can help compensate for the weakening of the bonds but eventually the calcium carbonate will interrupt the protein chains, reducing

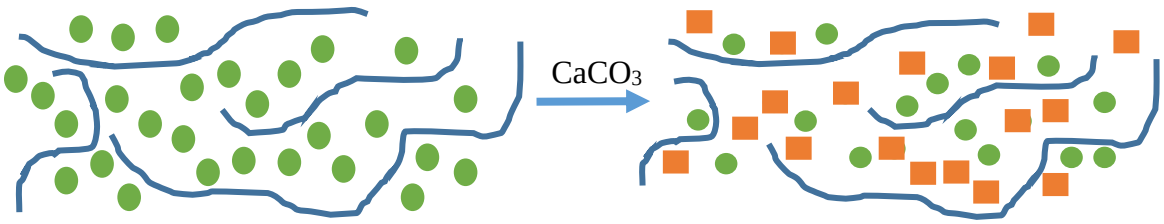

Figure 19: Schematic depiction of how calcium carbonate (orange squares) is reaction with the glutenin (blue lines) and gliadin (green circles).

workable. Although calcium carbonate has two hydrogen acceptors it does not react with water and must be reacting with the glutenin and gliadin. In Figure 19 the calcium carbonate is represented as the orange squares, the gliadin being the green circles and the glutenin is represented as the blue lines. The figure shows how the calcium carbonate can act as a spacer, lengthening and weakening the bonds between the glutenin and gliadin.

4.2 DISSOLVING STUDY

During dissolution in ethanol, the foam samples appear to have a pH increase that correlates to the mass of the spacer material. Shown in Table 2 and Table 3.

Table 2: Average pH from dissolving the different samples in ethanol.

	Small	Medium	Large
Average	9.15	8.96	8.19
StDev	1.8	0.08	0.3

Table 3: The theoretical weight of the heat treated noodles compared to the actual weight of the heat treated noodles for all sample sizes.

	Weight of noodles (g)	Flour (g)	CaCO3 (g)	CaO(g)	CO2(g)	Final Weight	Difference
Average	4.50	1.50	3.00	1.68	1.32	2.45	0.76
StDev	0.8	0.3	0.5	0.3	0.2	0.3	0.2

This pH increase was not originally hypothesized. The reason for a pH increase is theorized to be that calcium ethoxide would react with the water that is being created from the reaction and from the water in the 99.5% pure 200 proof anhydrous ethanol to create calcium hydroxide, which is basic. This is not a concern because the water will readily react with calcium over magnesium due to calcium having a higher reactivity and magnesium can readily be used in weak alkali bases, which is the classification calcium hydroxide falls into.

It was observed that a combination of mechanical agitation and dissolution lead to a more effect removal of the spacer material. For example, the medium samples that were dissolved using the stir bar took an average of 8.03 hours to dissolve, with a standard deviation (StDev) of 4 hours. The acoustic mixer dissolving set up for these specimens took an average of 0.5 hours, with a StDev of 0.2.

4.3 MAGNESIUM FOAM

The samples were compression tested, viewed under polarized light using an optical microscope, and chemically analyzed using a JEOL SEM-EDS / INCAx-sight. Analyzing this data can give insight into the grain size, chemistry, yield stress, peak stress, plateau stress, relative stress, relative density and deformation strain. Polished and mounted samples seen under a Zeiss Stemi2000-C Stereomicroscope at 6.5X magnification, after being etched can be seen in Figure 20 and Figure 21. In Figure 20 the cast magnesium and the cast magnesium machined into a tube (tube) can be seen showing the general circular shape and structure of the samples. Very little porosity was observed in these specimens.

Figure 20: Cast magnesium (left) and cast magnesium machined tube (right) etched and seen under a Zeiss Stemi2000-C Stereomicroscope at 6.5x to see the general shape and structure of the material.

Figure 21 shows a comparison of the pore size and structure of the different spacer sizes used. The foams produced with the largest spacers had pores with rough edges, indicative of solidification shrinkage. The foams produced with medium size spacers show evidence of both shrink and incomplete infiltration near the center of the sintered preform and the mold wall. This could be due to the sinter material being pressed against the side of the steel pipe. Specimens with this type of defect were reserved for microscopy studies and were not compression tested. The foams produced with the small spacer appeared to have the most uniform structure and the most complete infiltration compared to the other two sizes. There is still some shrinkage evident around the spacer material. It is also observed that the magnesium took the rectangular shape of the spacer material.

Due to these irregularities in the pore structure, care must be taken in machining of test specimens. The medium pore specimens had the largest average outer diameter (15.75 mm, standard deviation (StDev) – 0.3) because massive porosity close to the surface made machining impossible. The small pore specimens had a machined outer diameter average of 14.29 mm and StDev 0.05. The large pore specimens had a machined outer diameter average of 12.39 mm and StDev 0.4. Variations in pore structure often necessitated further reduction of the outer diameter dimension for different foam specimens.

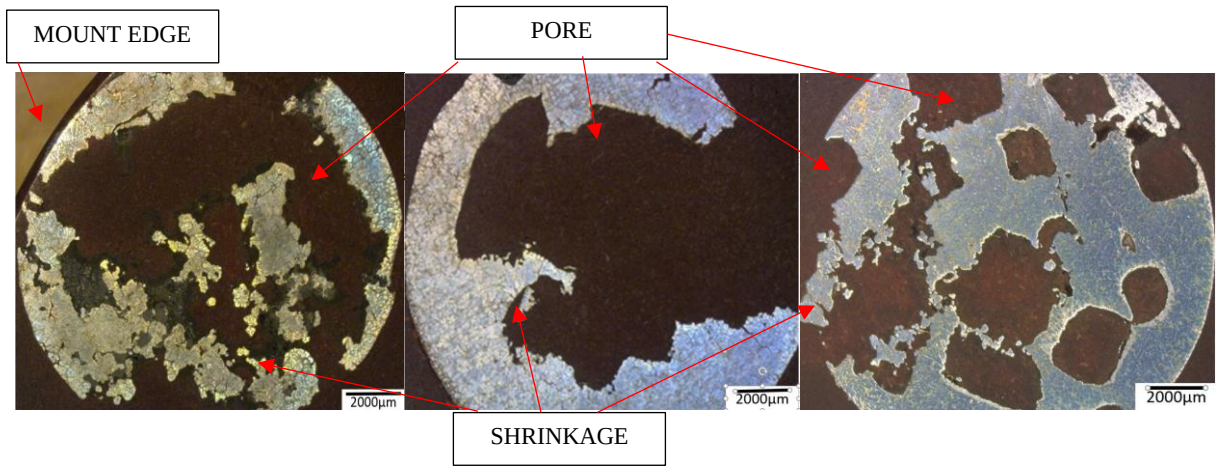

Figure 21: Large pore (left) foam, medium pore (middle) foam, and small pore (right) foam at 6.5x taken with a Zeiss Stemi2000-C Stereomicroscope after being etched. These images show the general shape and structure of the foams.

4.3.1 OPTICAL MICROSCOPE ANALYSIS

The stock ingot optical imaging shows the grain size and dendritic structure. The image shows that there is some porosity in the ingot, see Figure 22.

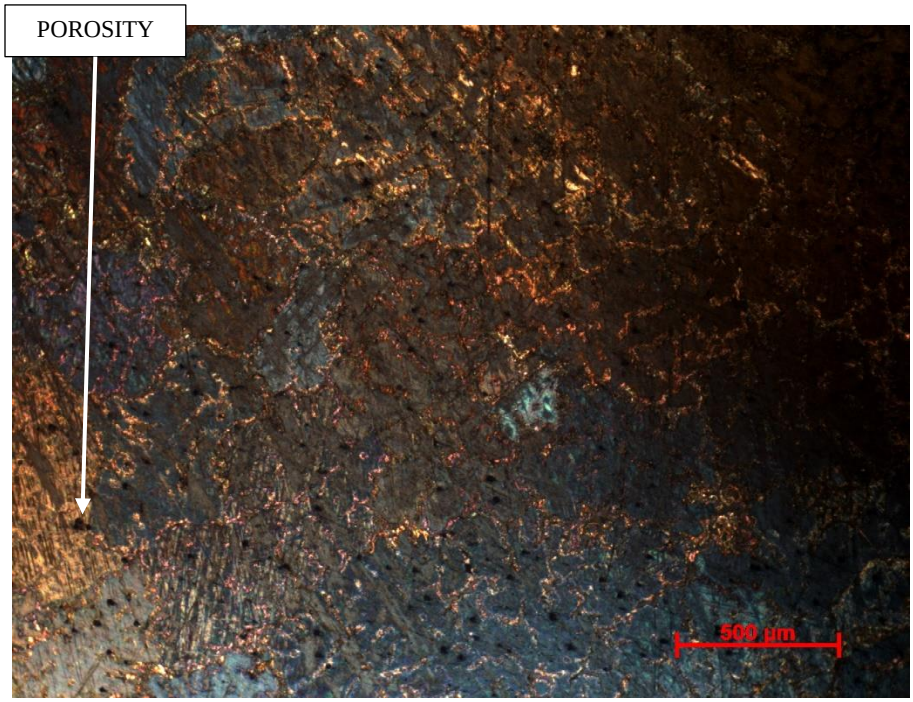

Figure 22: Magnesium stock ingot etched with 150mL ethanol, 50mL deionized water, and 1 mL glacier acetic acid at 50x taken with AX10-Zeiss Microscope under polarized light. This image is showing magnesium stock ingot metal after machining.

Figure 23 shows the machined cast AZ91D magnesium tube. The image shows the grains and dendrites of the samples. The machined inner and outer diameters, ID and OD respectively,

can be seen in the figure. The image also shows small porosity that occurred during solidification of the material.

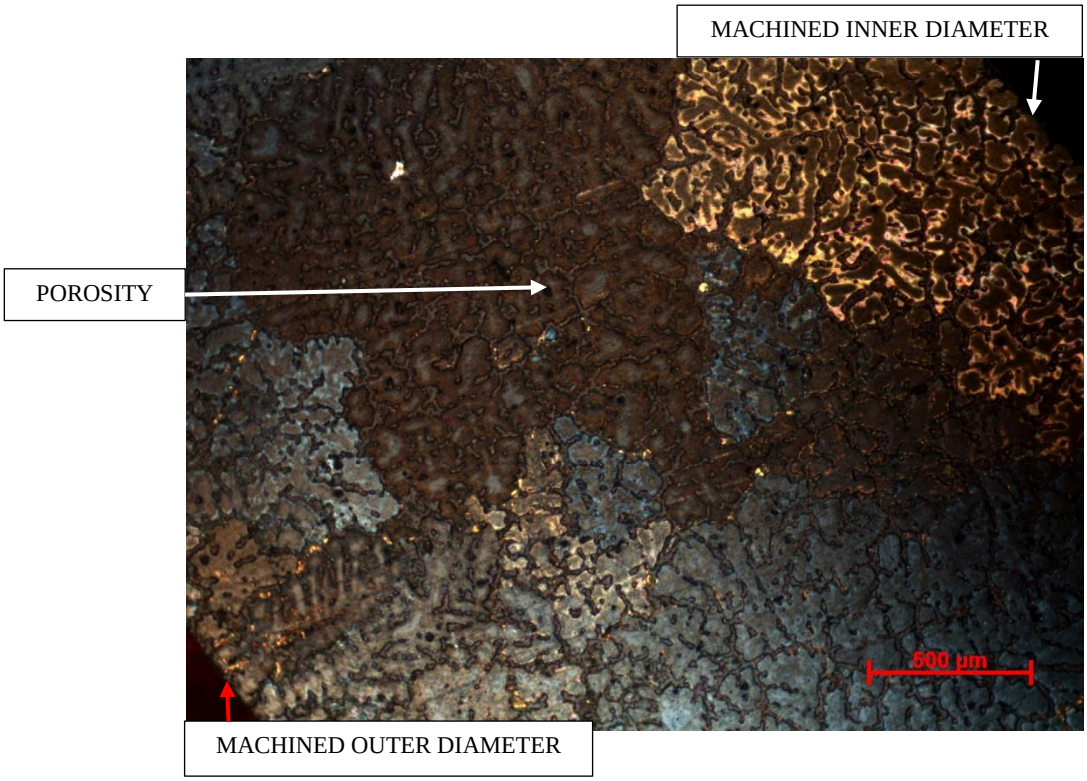

Figure 23: Cast magnesium etched with 150mL ethanol, 50mL deionized water, and 1 mL glacier acetic acid at 50x taken with AX10-Zeiss Microscope under polarized light. This image is showing magnesium metal after being cast using vacuum infiltration processes, a machined outer diameter and a hole drilled to be 6.35 mm in diameter.

The cast magnesium optical images can be seen below (Figure 24 and Figure 25) showing the grain size and dendritic structure. The images also show the machined edges of the samples, some porosity in the material and some cracking on the edge of the sample. The cracking on the edge of the sample could be from the lathe used to machine the samples.

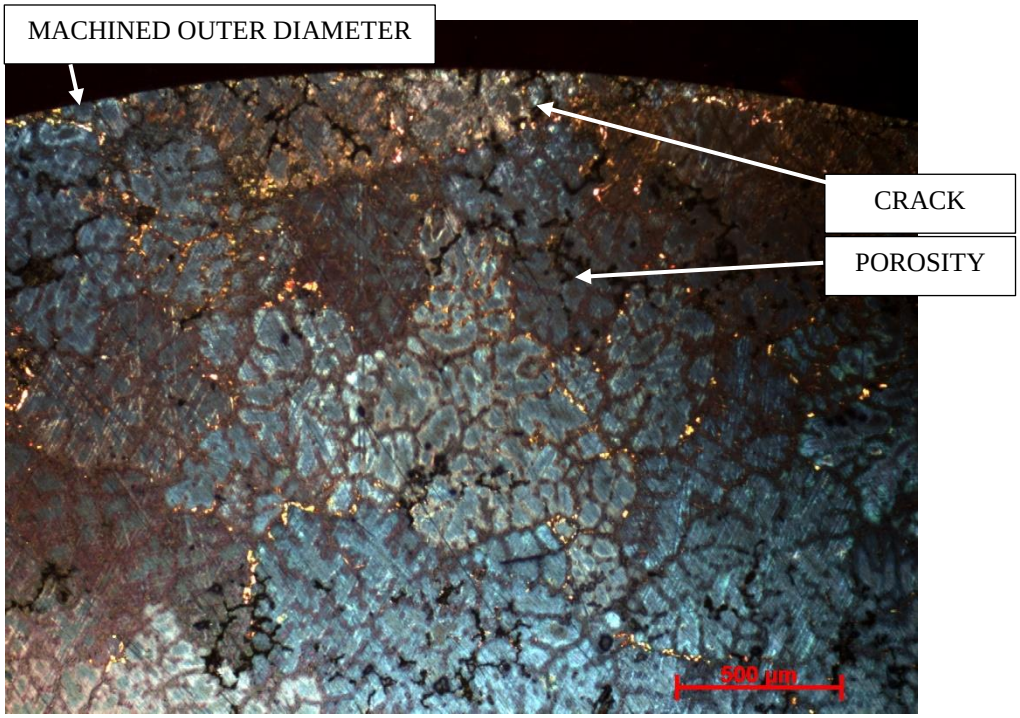

Figure 25:Magnesium casting etched with 150mL ethanol, 50mL deionized water, and 1 mL glacier acetic acid at 50x taken with AX10-Zeiss Microscope under polarized light. This image is showing magnesium metal after being cast using vacuum infiltration processes and machining.

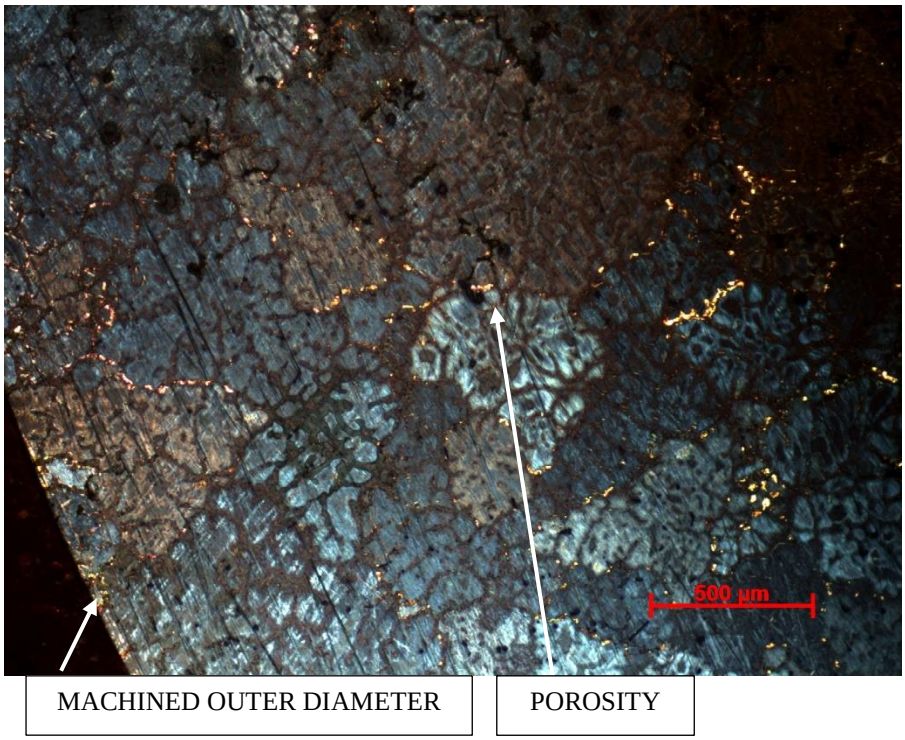

Figure 24:Magnesium casting etched with 150mL ethanol, 50mL deionized water, and 1 mL glacier acetic acid at 50x taken with AX10-Zeiss Microscope under polarized light. This image is showing magnesium metal after being cast using vacuum infiltration process and machining.

Figure 26 shows the large pore size, center of the magnesium casting. In the figure the grains and dendrites can be seen, along with porosity in the grain boundaries. The porosity here is due to the improper feeding the metal would have during solidification in the center of the casting. The edging of these pores all demonstrate shrink during solidification by the spacer material.

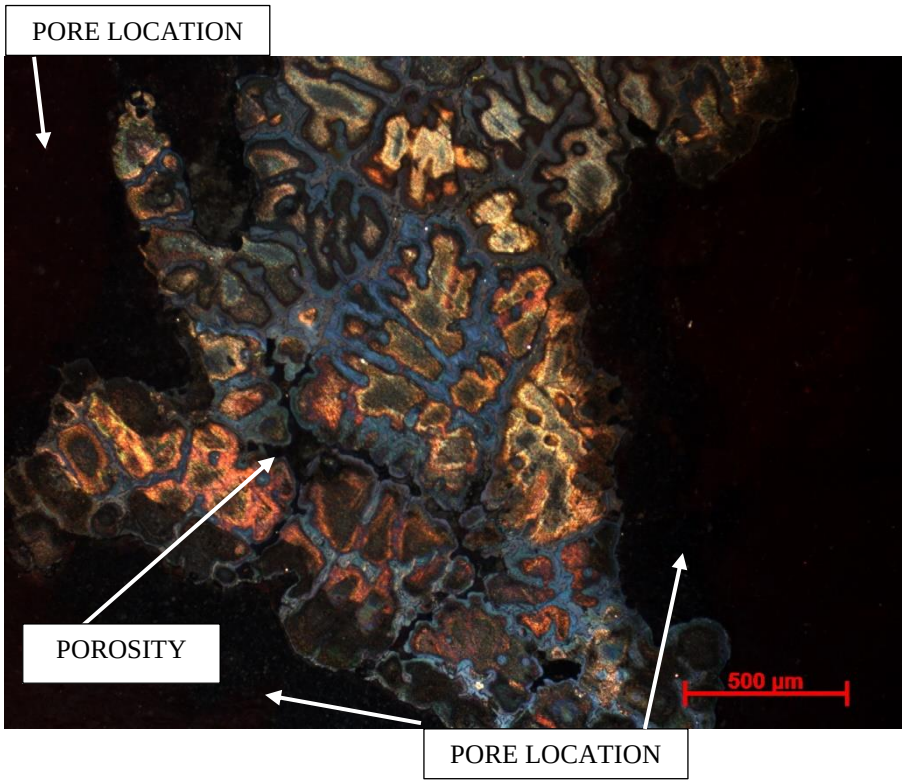

Figure 26: Magnesium large spacer size foam etched with 150mL ethanol, 50mL deionized water, and 1 mL glacier acetic acid at 50x taken with AX10-Zeiss Microscope under polarized light. This image is showing magnesium metal foam after the large spacer material has been dissolved.

Figure 27 shows the center of the magnesium medium pore size's grain and dendritic structure. The sample shows some porosity and scratching as well. The pore in the upper left corner does not demonstrate shrinkage around the spacer material during solidification, where the pore in the lower right corner does. The shrink can be identified by the rough edging of the pore.

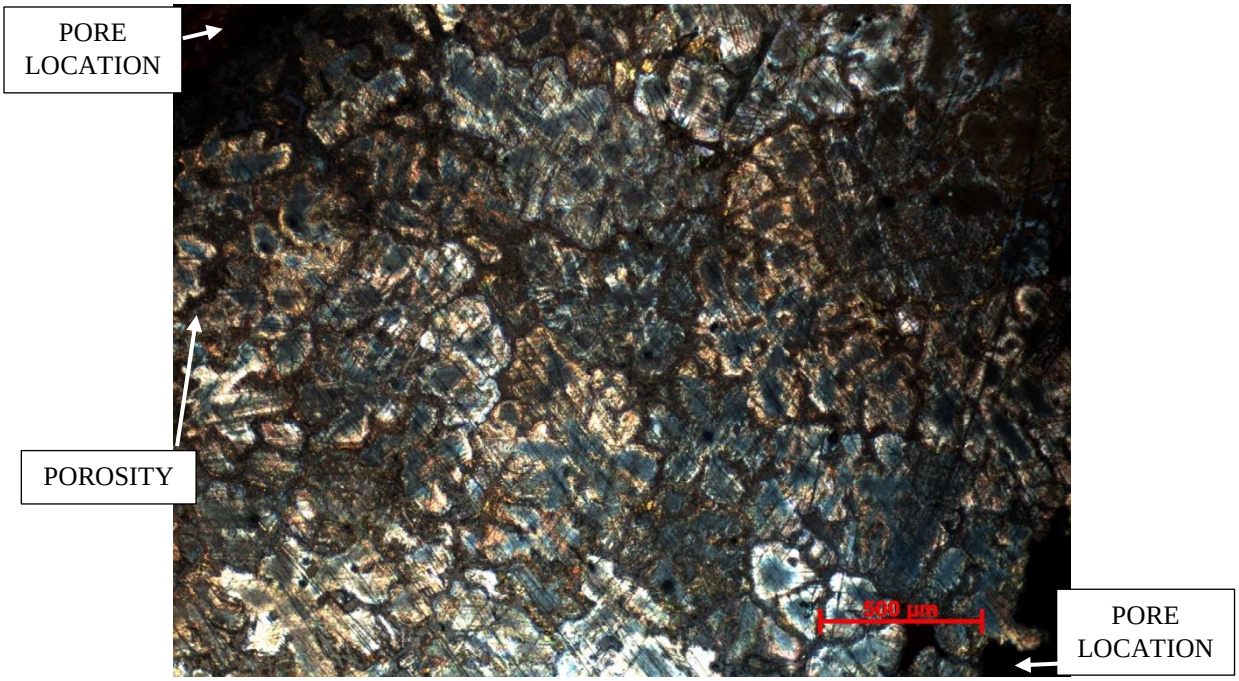

Figure 27: Magnesium medium pore size foam etched with 150mL ethanol, 50mL deionized water, and 1 mL glacier acetic acid at 50x taken with AX10-Zeiss Microscope under polarized light. This image is showing magnesium metal foam after the medium spacer material has been dissolved.

Figure 28 and Figure 29 show the small pore size magnesium foam sample's grain structure and dendritic structure. In the images shrink, porosity, a crack and a scratch can be seen. The small pore size has shrink around the spacer material and other areas where the magnesium did not show shrink around the spacer material and took the shape of the spacer. This can be seen by the smoother edges of the magnesium at a pore.

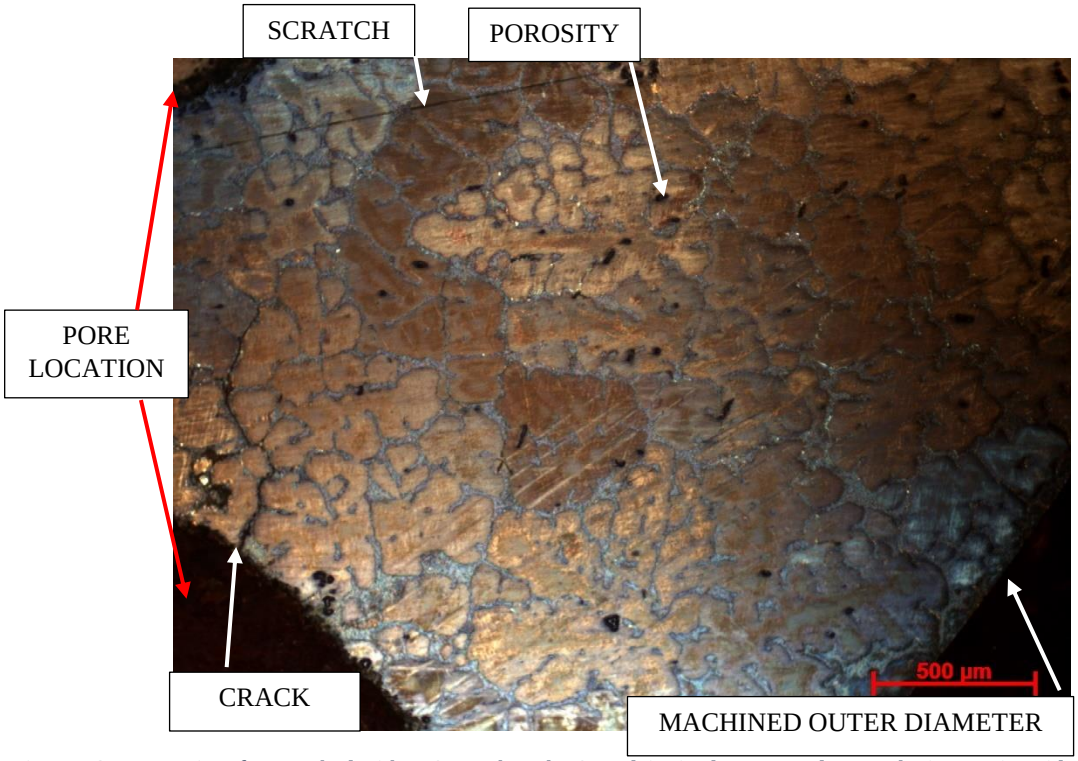

Figure 28: Magnesium foam etched with 150mL ethanol, 50mL deionized water, and 1 mL glacier acetic acid at 50x taken with AX10-Zeiss Microscope. This image is showing magnesium metal foam after the small spacer material has been dissolved and the outer diameter was machined.

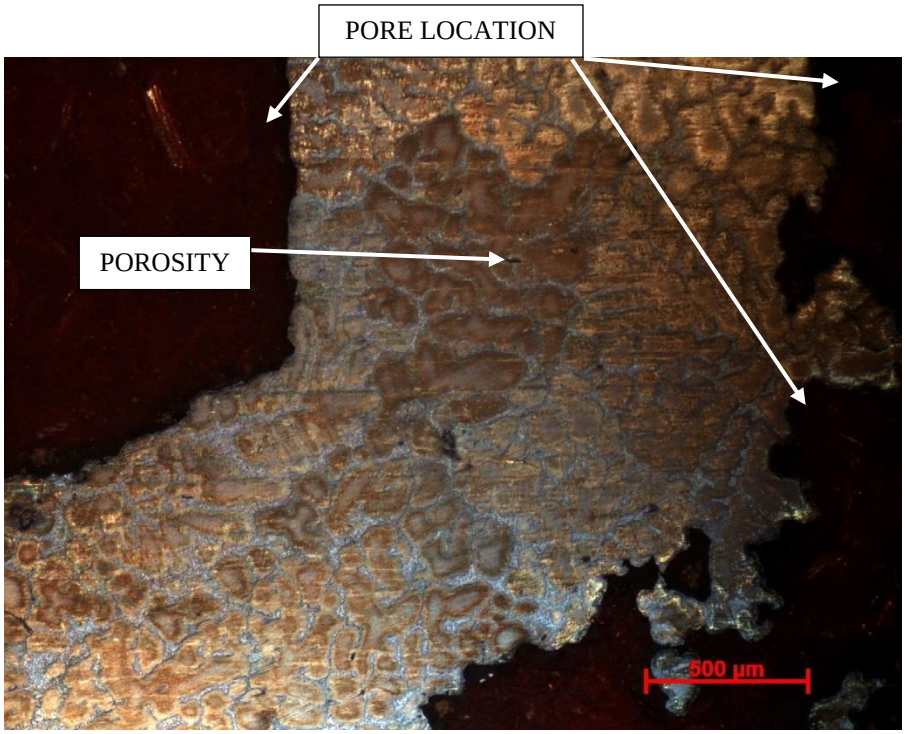

Figure 29: Magnesium foam etched with 150mL ethanol, 50mL deionized water, and 1 mL glacier acetic acid at 50x taken with AX10-Zeiss Microscope. This image is showing magnesium metal foam after the small spacer material has been dissolved and the outer diameter was machined.

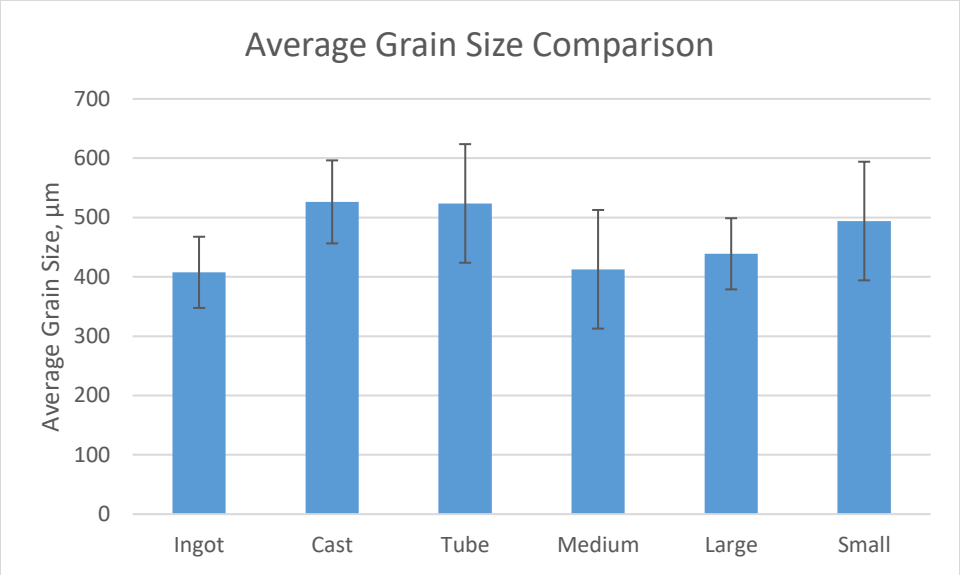

Figure 30: Average grain size of the different magnesium structures.

Statistically there is no large difference between the pore sizes and the grain sizes, Figure 30. The reason that the small pore size may be showing a higher average grain size is that there is more space between and around the spacer material, creating thicker cell wall, for the grains to grow

All the samples were melted and cooled using the same processes. The spacer material would not have acted as a chill because it was brought up to temperature with the AZ91D ingot. The reason for seeing more shrink in the larger pore sizes is theorized to be due to the smaller cell walls and difficulty in getting feed metal to this area during solidification, especially when located in the middle of the casting. Some of the cracks could have been formed during the removal of the samples form the steel tubes and from machining process.

.

4.3.1 JEOL SEM CHEMICAL ANALYSIS

Specimens were examined via scanning electron microscopy (SEM) and energy dispersive spectroscopy (EDS) to investigate the chemistry of AZ91D and its foams, as well as phases formed in the presence of CaO spacer materials. Table 4 presents a summary of the EDS results taken in various locations of the materials developed in this work. The results for the raw ingot (prior to processing) is shown in the first row, followed by the tube specimen (from the processed material), the solid cylinder (from the processed material) and the foams created with large, medium and small spacers respectively. The chemistry of the alloy ingot varies considerably from the nominal composition of the AZ91D alloy (8.3-9.7% Al, 0.35-1.0% Zn, up to 0.3% Other, balance Mg). It is possible that, due to the high vapor pressure of Zn (approximately 10 times that of magnesium at the same temperature), it was lost from the alloy during melting under vacuum. Similarly, the aluminum content ranged from 9.26 – 15.97. Aside from local variations in composition, it is possible and probable that the alloy was altered due to vacuum melting. According to the Mg-Al phase diagram (Figure 31), intermetallics of $Al_{12}Mg_{17}$ should be present in the solidification structure as is indicated in Table 4.

Table 4: EDS results obtained of fields shown in SEM micrographs of Figure 32-Figure 39. The microstructures were found to contain mostly Mg, Al, Ca, and O. Suggested phases are shown, where γ is $Al_{12}Mg_{17}$, and ε is Mg.

Specimen	Location	Phases	Mg	Al	Ca	O
Ingot	Center	γ+ε	84	12.26	0.68	0.18
Tube	Center	γ+ε	85.81	15.02	-	-
Solid Cylinder	Center	γ+ε	84.03	15.97	-	-
Large	Pore	γ+ε	84.42	15.55	0.32	-
	OD	γ+ε	75.58	11.2	13.01	0.2
Medium	Center	γ+ε	84.05	15.53	0.42	-
	Pore	γ+ε	88.34	11.31	0.35	-
Small	Pore 1	γ+ε, Al_4Ca	82.54	15.11	2.79	-
	Pore 2	γ+ε, MgO,CaO	67.18	11.5	2.74	18.59
	OD	γ+ε	81.56	9.26	1.37	7.81

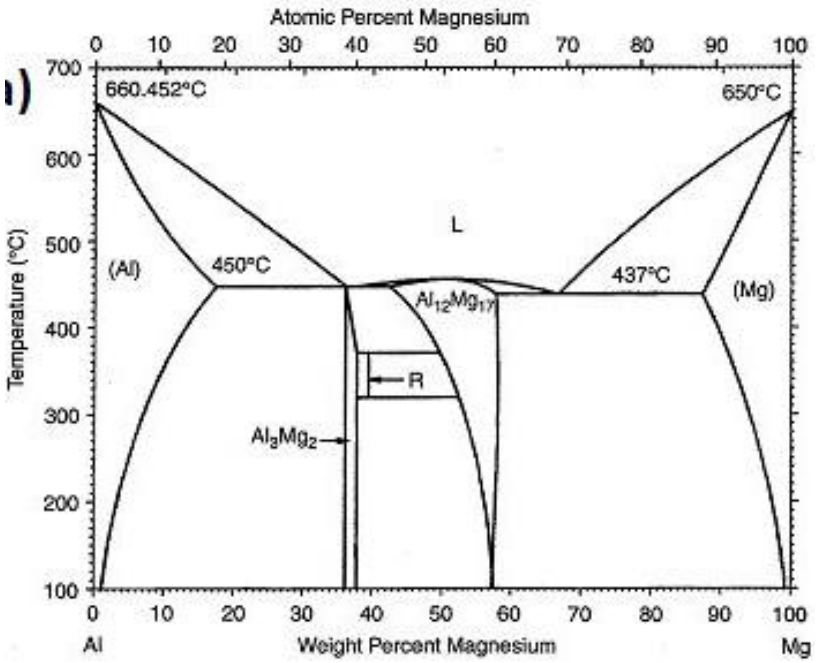

Figure 31: Al-Mg Phase Diagram. (Yang, 2013)

Figure 32 through Figure 39 show SEM micrographs of the materials documented in Table 4. Each specimen showed typical microstructures observed in cast magnesium AZ91D alloys, where primary magnesium dendrites are surrounded by Al-Mg intermetallics. Calcium was not observed in the solid cylinder and tube specimens, however calcium was observed in the ingot, as well as in some of the foam specimens. Likewise, the oxygen content was not significant in most of the specimens apart from in the smallest pore size specimens. The presence of both calcium and oxygen in the foam specimens may indicate that some reaction has occurred with the spacer material, or residual spacer material remains in the specimen. Overall the samples were composed of Mg (ε), and $Mg_{17}Al_{12}$ (γ) as is expected in the Al-Mg binary system. The only samples that showed significant evidence of reaction with the spacer material to form Al_4Ca were foams made using the small spacer material.

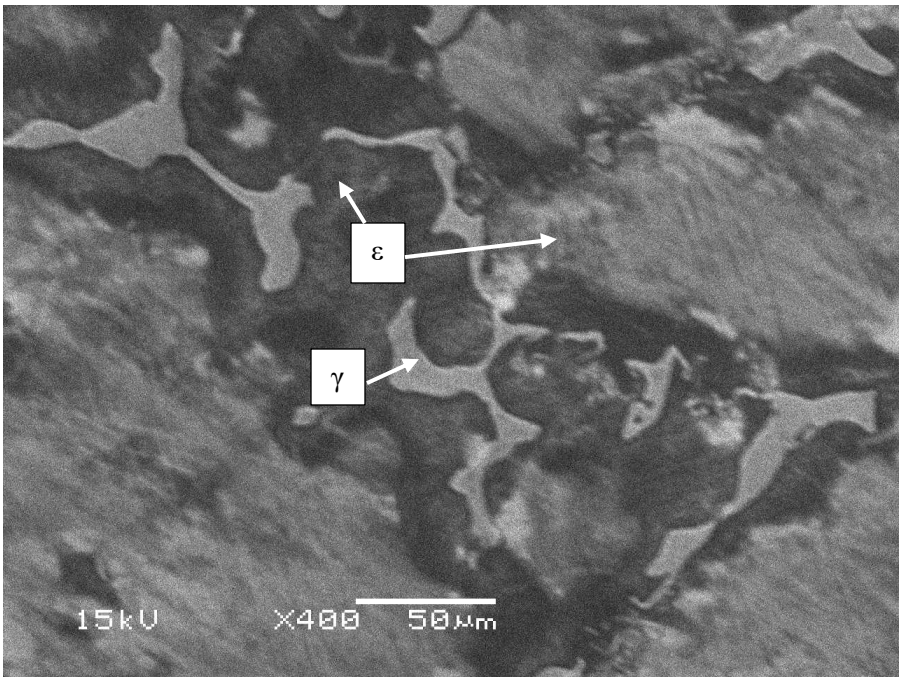

Figure 32: Ingot magnesium JEOL SEM, 400x, WD 15mm, 15vK. Showing the different phases present in the stock ingot AZ91D.

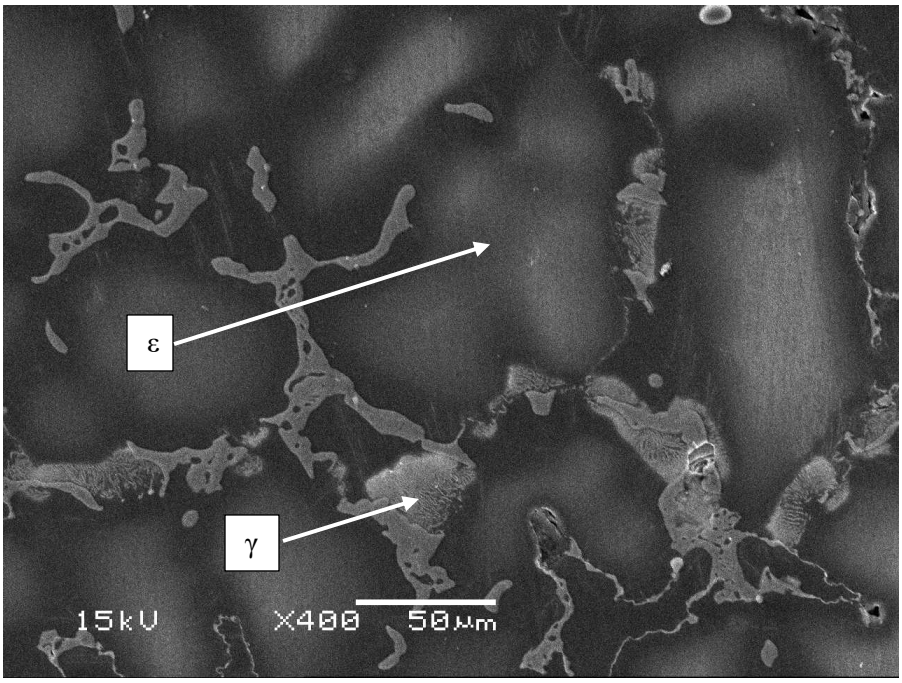

Figure 33: Cast magnesium, JEOL SEM, 400x, WD 12mm, 15vK. Showing the different phases present in the cast AZ91D.

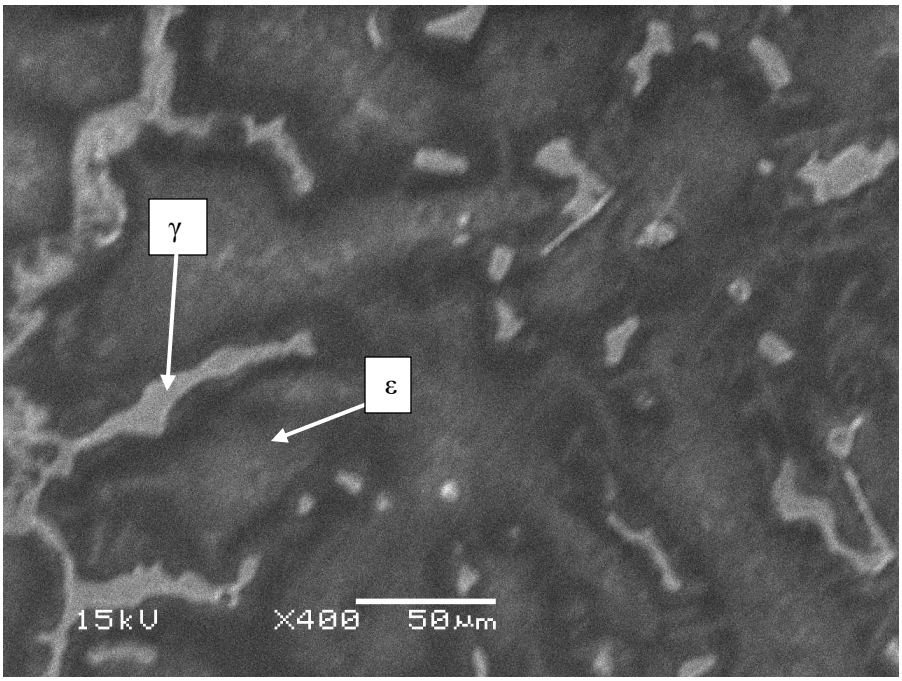

Figure 34: Tube magnesium JEOL SEM, 400x, WD 13mm, 15vK. Showing the different phases present in the cast ingot machined into a tube AZ91D.

The large pore size outer diameter (OD) reading is showing a high calcium reading. This could be because calcium and carbon have similar peaks on the EDS analysis. Due to the way SEM-EDS takes a spectrum, the results can be affected by the material surrounding and beneath the point or rectangle selected in a three-dimensional fashion. The mounting material is a carbon-based polymer and is most likely giving the carbon and potentially contributing to a calcium reading for the porous samples. The large pore size didn't have any calcium readings in the matrix only on the very edges of the specimens which might have been partially infiltrated with the mounting material. SEM and point EDS analysis does not provide evidence of reaction between aluminum and calcium to form Al_2Ca on the edges pores. Rather, calcium is suspected to be present due to undissolved spacer material and proximity to mounting material.

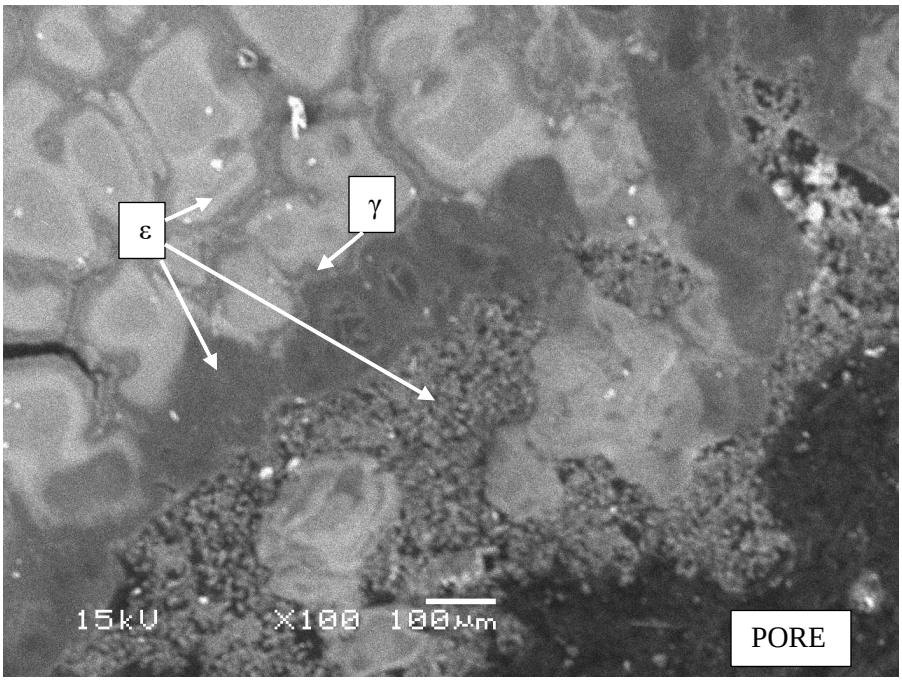

Figure 35: Large pore size foam magnesium JEOL SEM, 100x, WD 15mm, 15vK. Image is showing section of magnesium directly next to a pore. Showing the different phases present in the large pore size casting AZ91D.

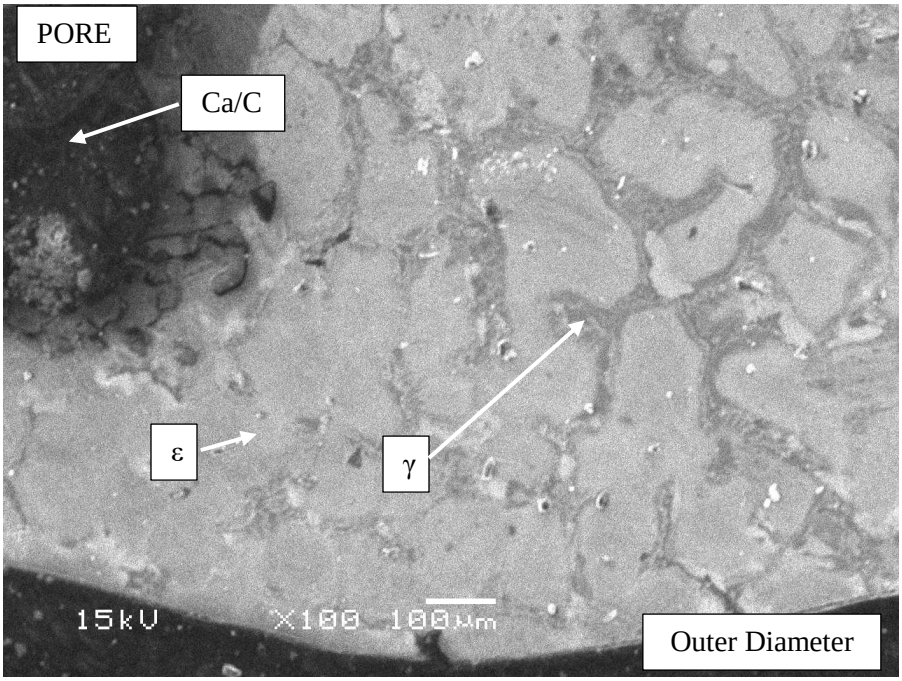

Figure 36: Large pore size foam magnesium JEOL SEM, 100x, WD 13mm, 15vK. Image is showing section of magnesium directly next to a pore and machined outer diameter. Showing the different phases present in the large pore size casting AZ91D.

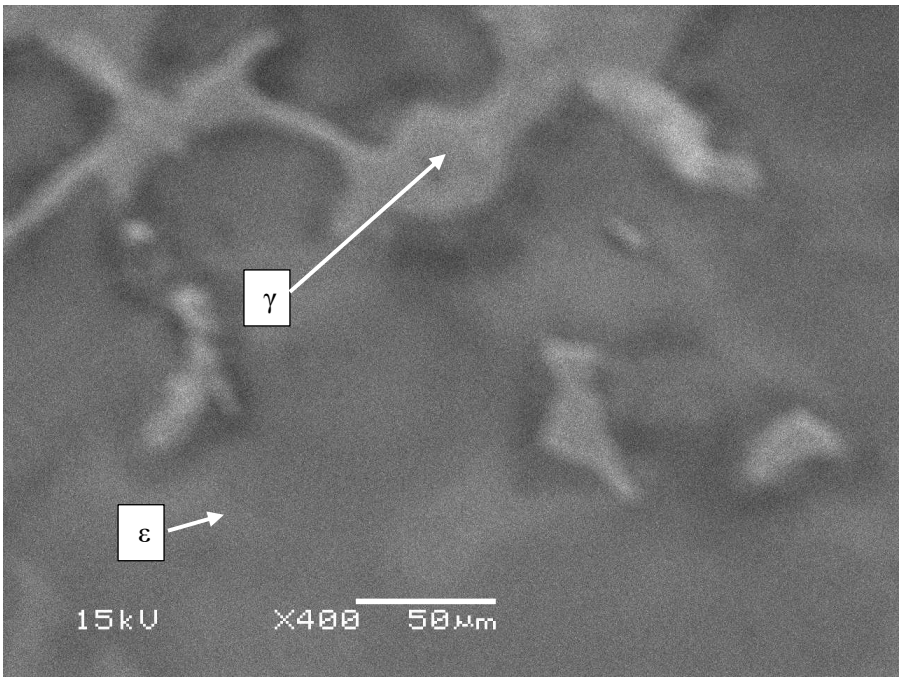

Figure 37: Medium spacer foam magnesium JEOL SEM, 400x, WD 16mm, 15vK. Image is showing the center section of magnesium. Showing the different phases present in the center of the medium pore size casting AZ91D.

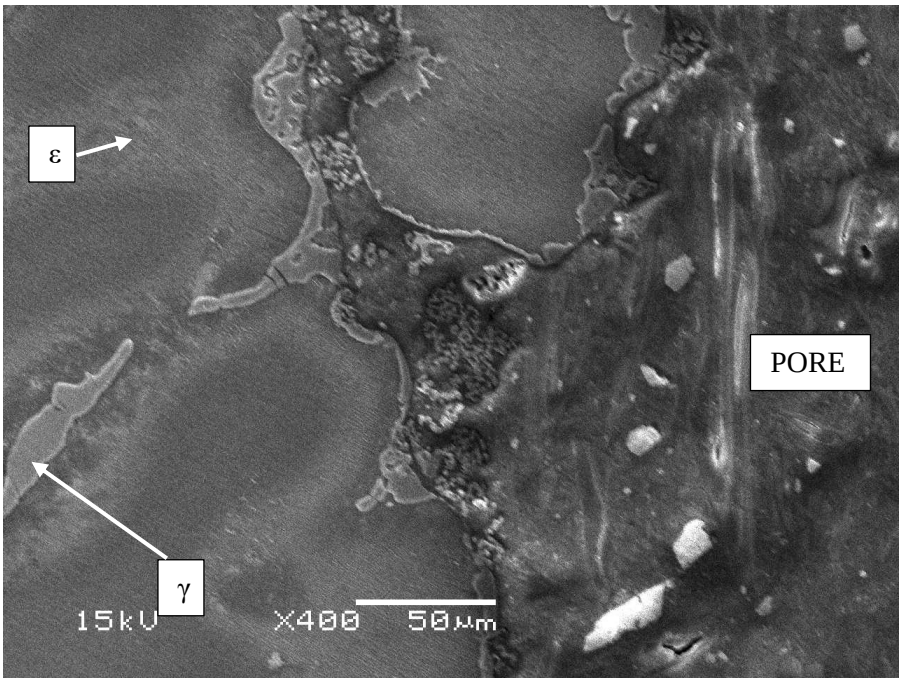

Figure 38: Medium pore size foam magnesium JEOL SEM, 400x, WD 15mm, 15vK. Image is showing a section of magnesium next to a pore. Showing the different phases present in the cast medium pore size AZ91D.

The small pore size specimens also showed an increase in the calcium content from the ingot. The sample shown in Figure 39 was dissolved for 15 minutes using the acoustic mixer

system. Therefore, these increases appear to be from a combination of calcium oxide dissolving into the solute element aluminum in the magnesium base metal creating Al_4Ca phase; see Figure 39 and appendices Figure 82 through Figure 99. The small pore size could contribute to the uptake of Ca surrounding the pores and in the grain boundaries of the sample. This increase of Al_4Ca in the grain boundaries reduces the $Mg_{17}Al_{12}$ in the grain boundaries (Guohua, Fan, Gao, Zhai, & Zhu, 2005). An increase of calcium in the grain boundaries can be seen throughout the sample near other pores and the outer diameter. This uptake of calcium could be due to the high surface area that the small pore size has compared to the other pore sizes used as illustrated in Figure 40. This could have affected the time needed for baking the material from calcium carbonate to calcium oxide. The baking time may need to be extended. The reason for this theory is that calcium oxide is a very stable material and will not readily break down to bond with aluminum but the ionic bond of calcium carbonate would readily break down to form Al_4Ca.

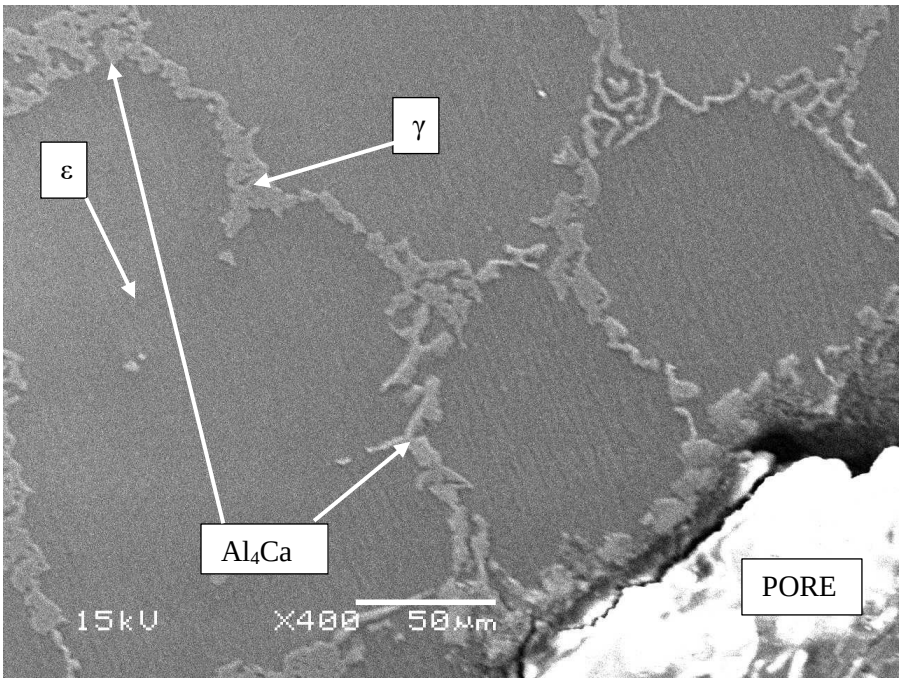

Figure 39: Small pore size foam magnesium JEOL SEM, 400x, WD 16mm, 15vK. Image is showing a section of magnesium next to a pore. Showing the different phases present in the cast small pore size AZ91D.

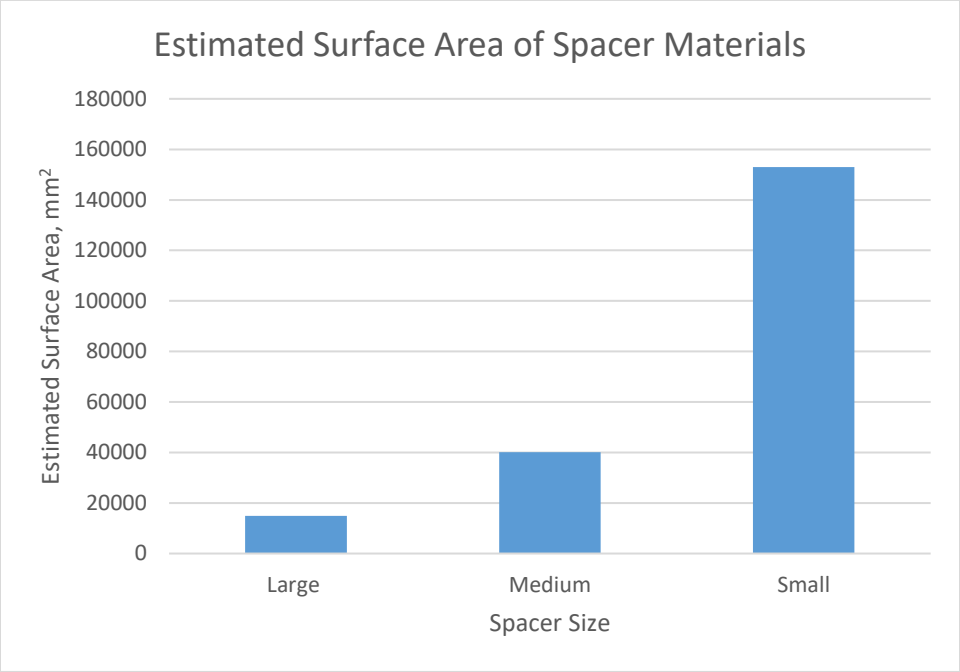

Figure 40: A graph depicting the difference in surface area of the three spacer sizes.

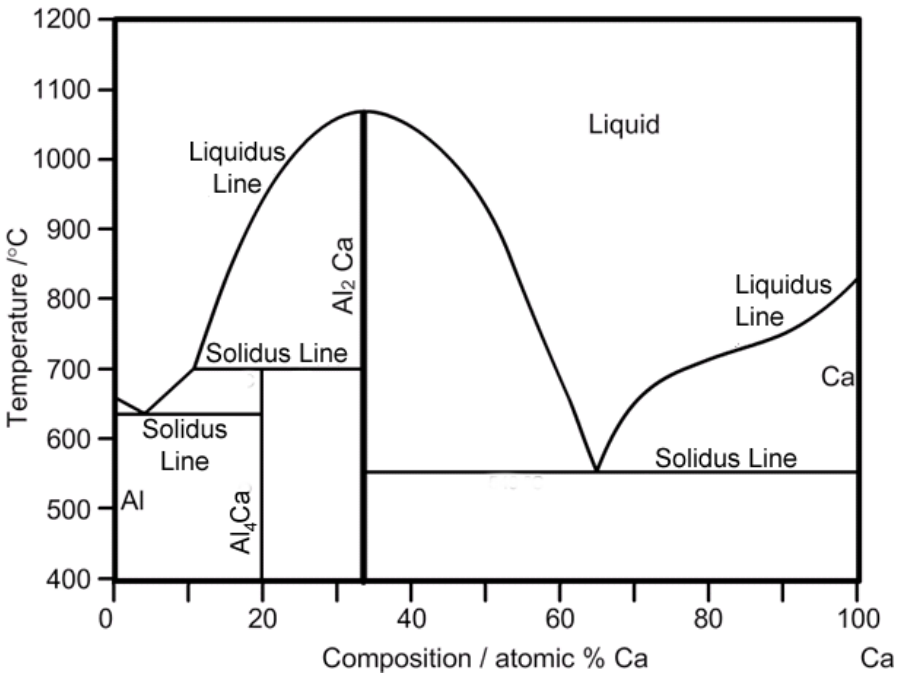

Figure 41: Al-Ca phase diagram. (Impression Across Europe: Solidification, n.d.)

4.3.2 COMPRESSION TESTING ANALYSIS

The compression testing data shows a linear trend of the yield stress verses calculated relative stress (Equation 1) indicating a valid and correlating data set (Figure 42). The individual values for the mechanical properties can be found in Table 5. The relative stress, and porosity were calculated using Equation 1 and Equation 2 respectively.

*Table 5: Average and standard deviations of the mechanical properties of the varies magnesium cast structures. *Note: The tube information was calculated taking the total surface area as if not a tube. ** Deformation strain was calculated by finding the intercept of the plateau line with the linear line of densification.*

		Solid	**Tube***	**Large**	**Medium**	**Small**
Density	Average	1.77	1.58	1.09	1.22	1.28
	StDev	0.012	0.05	0.3	0.04	0.16
Peak Stress	Average	299.09	183.51	34.6	84.85	89
	StDev	10	9	40	5	4
Plateau Stress	Average	N/A	43.65	12.31	32.46	30.42
	StDev	N/A	40	20	13	6
Densification Strain**	Average	N/A	0.36	0.24	0.290	0.28
	StDev	N/A	0.019	0.05	0.0020	0.02
Yield Stress	Average	171.5	73.95	19.95	56.6	57.7
	StDev	40	40	20	10.0	2.00
Relative Stress	Average	N/A	0.49	0.58	0.57	0.53
	StDev	N/A	0.5	0.18	0.2	0.11
Relative Density	Average	1	0.78	0.62	0.69	0.72
	StDev	0	0.03	0.18	0.019	0.09
Porosity Percentage	Average	0	23.73	37.3	30	26.37
	StDev	0	3	20	2	9

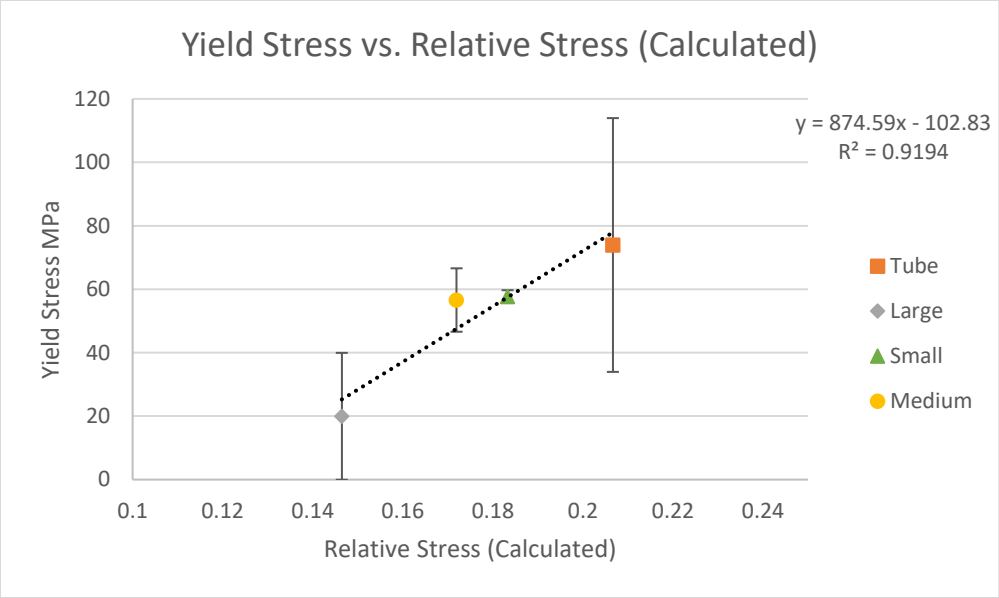

Figure 42: Yield stress vs calculated relative stress showing a linear trend.

The yield stress, peak stress, plateau stress, and densification strain were analyzed from the compression data using the analyzation techniques seen in Figure 43. The yield stress was determined by finding the Young's modulus and comparing the 0.5% offset calculated stress to the actual stress. The densification strain was found by determining the linear trend line with the increase in stress after the plateau region was complete. The average plateau region was then considered to be y and the unknown variable x for the trendline is the densification strain.

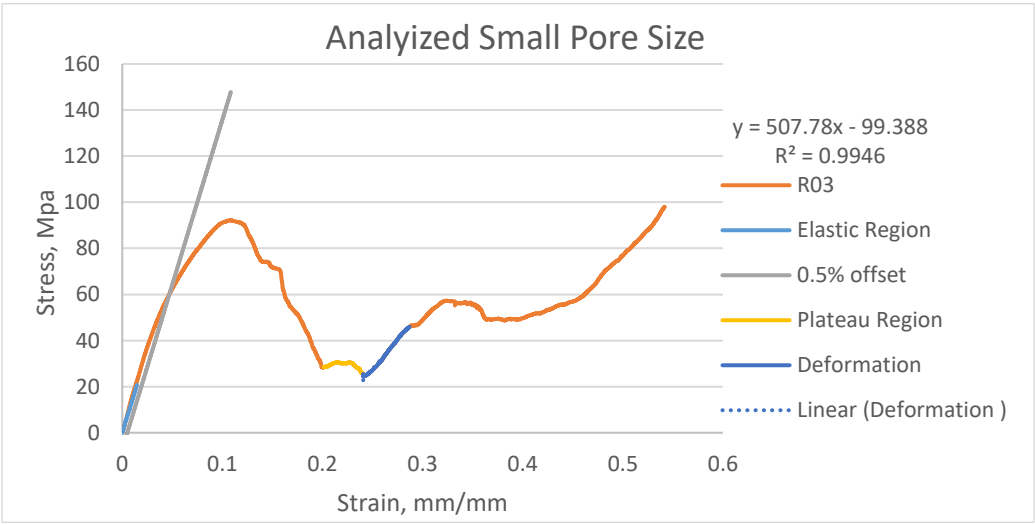

Figure 43: Small pore size compression test analyzed stress-strain curve.

Figure 44 shows a comparison of randomly chosen stress- strain curves for each pore size. The smaller the pore size the higher the peak stress and plateau stress, which is similar to other research by previous authors on magnesium foams. However, the data on the large pore size sample does not follow the trend. The large pore size does not meet the 7 times smaller than the sample size requirement (Ashby, et al., 2000). The sample size for the large pore samples are only 2.13 times larger than the volume of the large pore system, which causes a wide standard deviation of the large results. This ratio being off will contribute to the large pore size having a very large standard deviation.

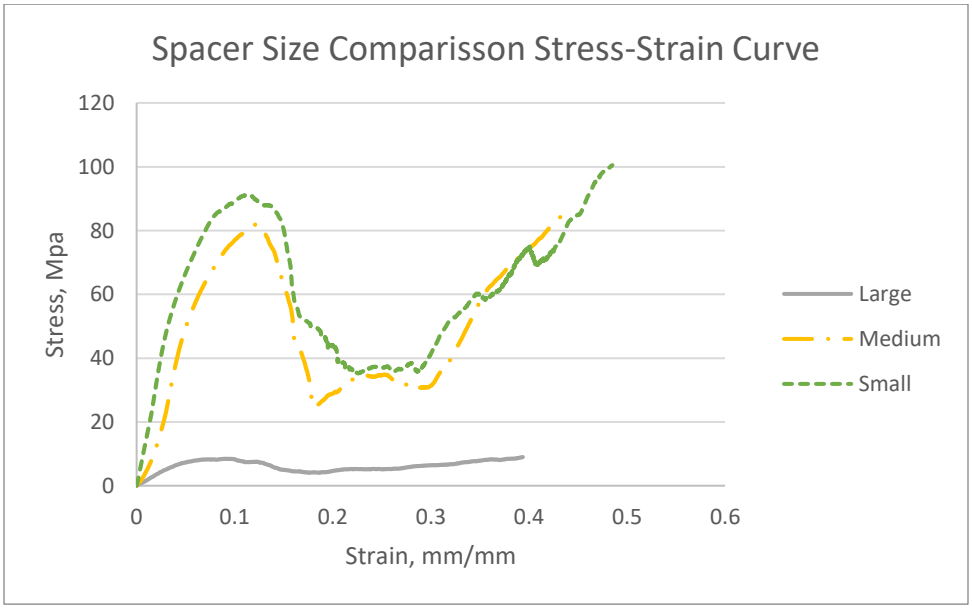

Figure 44: Spacer size comparison in stress strain curve, the data was choosen as general representations of each spacer size.

Figure 45 shows that the statistically the foams do not have a difference in density due to the standard deviations of the samples. The average densities of the AZ91D foam does follow the general trend commonly seen of the smaller the pore size the higher the density, due to cell wall thickness increasing.

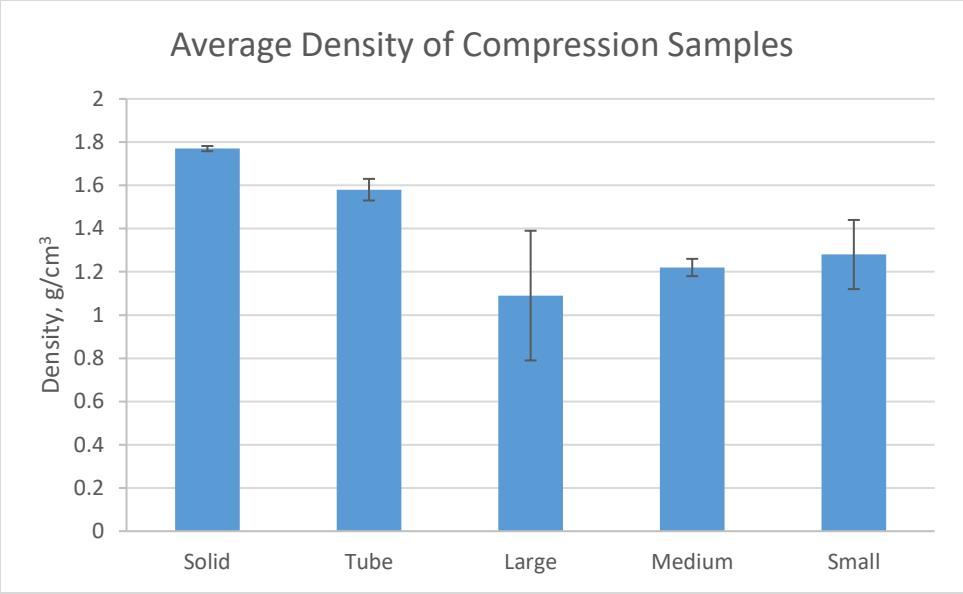

Figure 45: Comparison of the densities of the different magnesium structures.

The trend of the peak stress and yield stress is to have a positive linear correlation with the relative density of the different samples (Figure 46 and Figure 47). These trends show R^2 values close to one indicating a good correlation between data points.

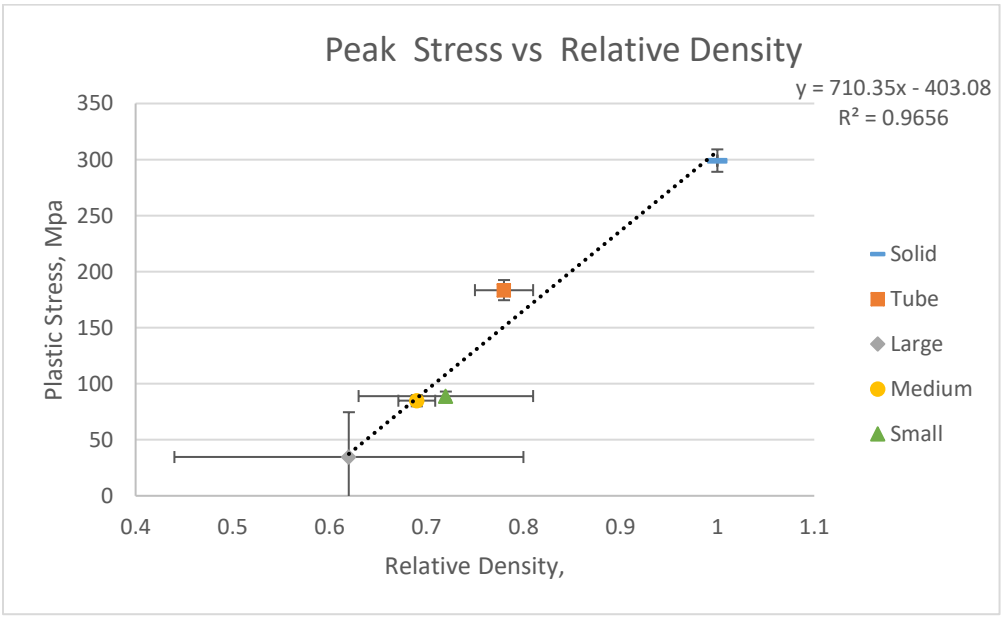

Figure 46:Average peak stress vs density form stress-strain compression curve

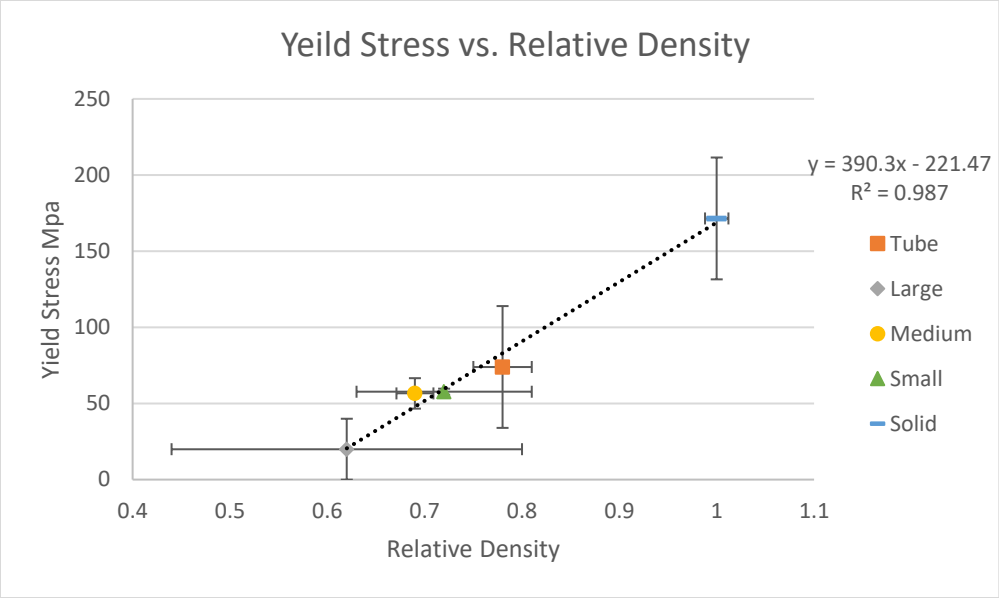

Figure 47: Yield stress vs relative density of the different cast samples.

The tube material behaved in the same trends as if it was a foam even though the "pore" was a singular hole. The tube data is forcing a trend to be seen in the comparison of the plateau stress verse relative density to have a trend (Figure 48). When the tube is not taken into consideration (Figure 49) the plateau stress and relative density have no trend (R^2=0.86) showing that the two properties are independent of each other, which is standard for magnesium foam samples (Hao, Han, & Li, 2009). This shows that the tube magnesium is not following the trends needed to be considered a magnesium foam. this means that the tube will not be considered in the deformation strain

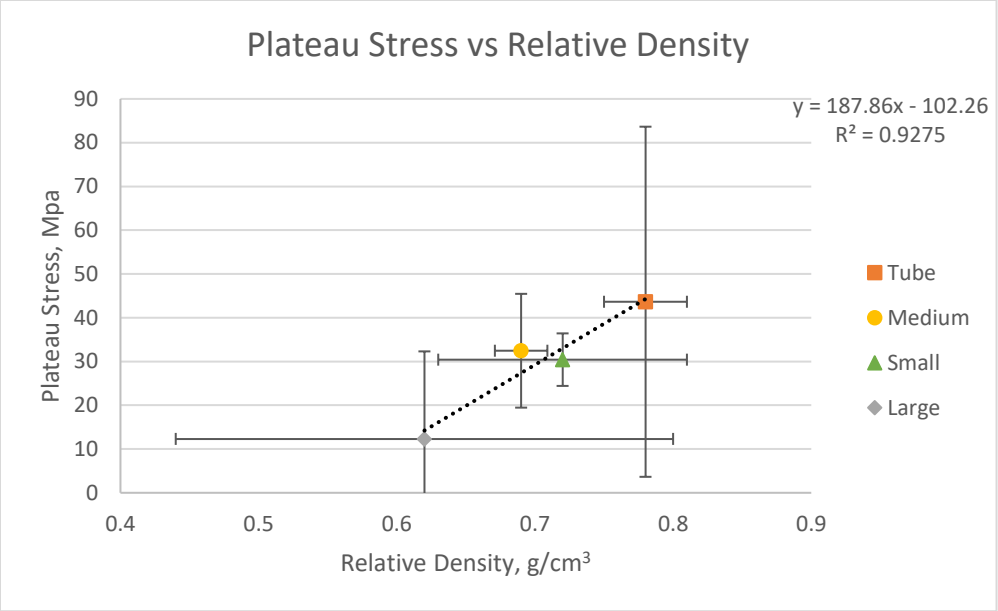

Figure 48: Plateau stress vs relative density, tube data taken into consideration

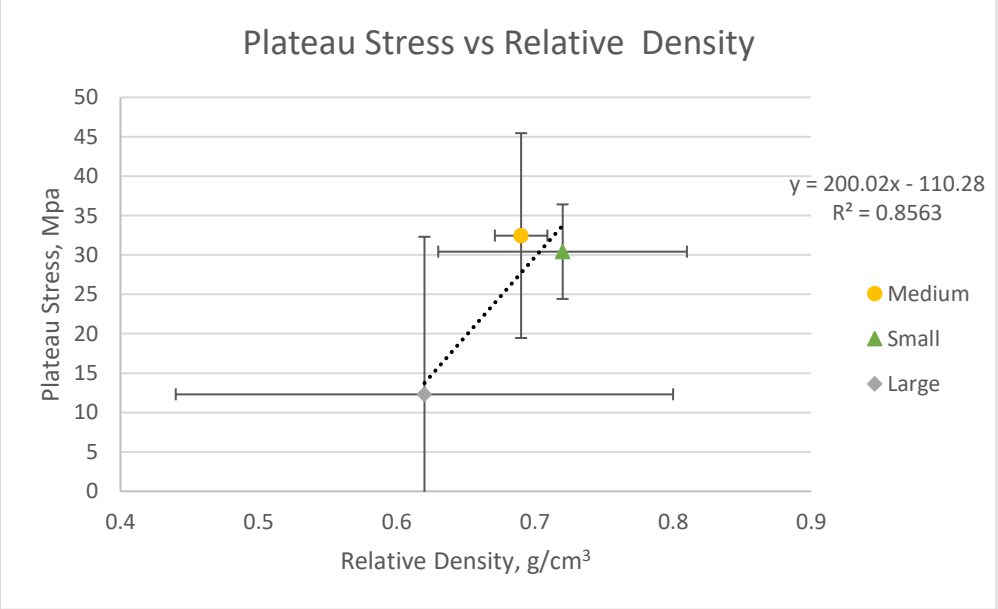

Figure 49: Plateau stress vs relative density, tube data in not taken into consideration

The percent porosity of the samples are not statistically different and the averages have a range of 10.93% for percent porosity and 0.05 for densification strain. Due to this statistical indifference of both properties for the foam samples, the samples do not show a trend for the densification strain verse the percent porosity of the samples (Figure 50).

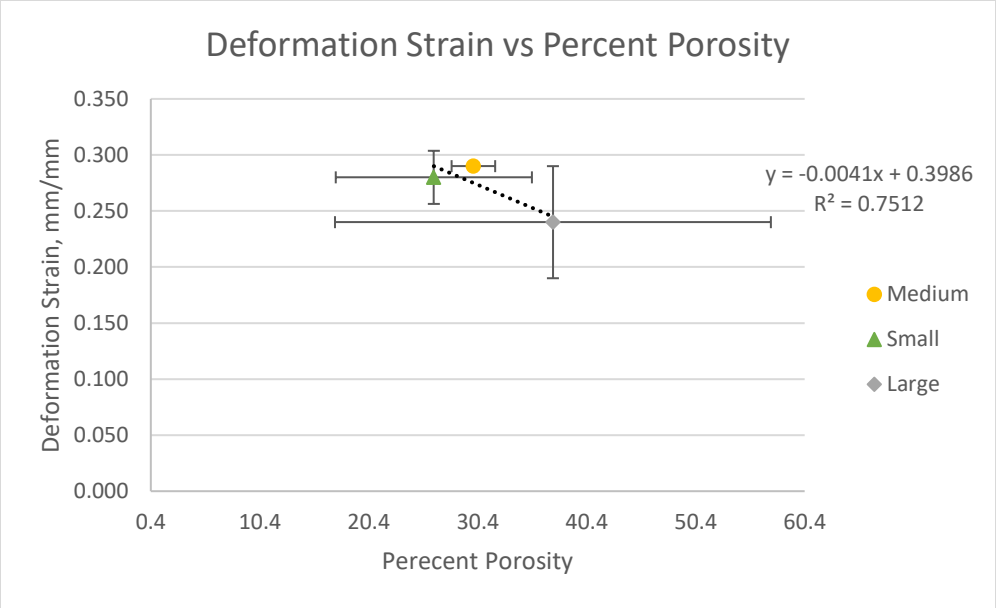

Figure 50: Deformation strain vs Relative Density.

The percent porosity and relative density due have a strong correlation to each other when all the samples are considered (Figure 51). This graph includes the facts that at a relative density of 1 there is zero porosity in the sample and that at a relative density of 0 there is 100% porosity of the sample (no sample).

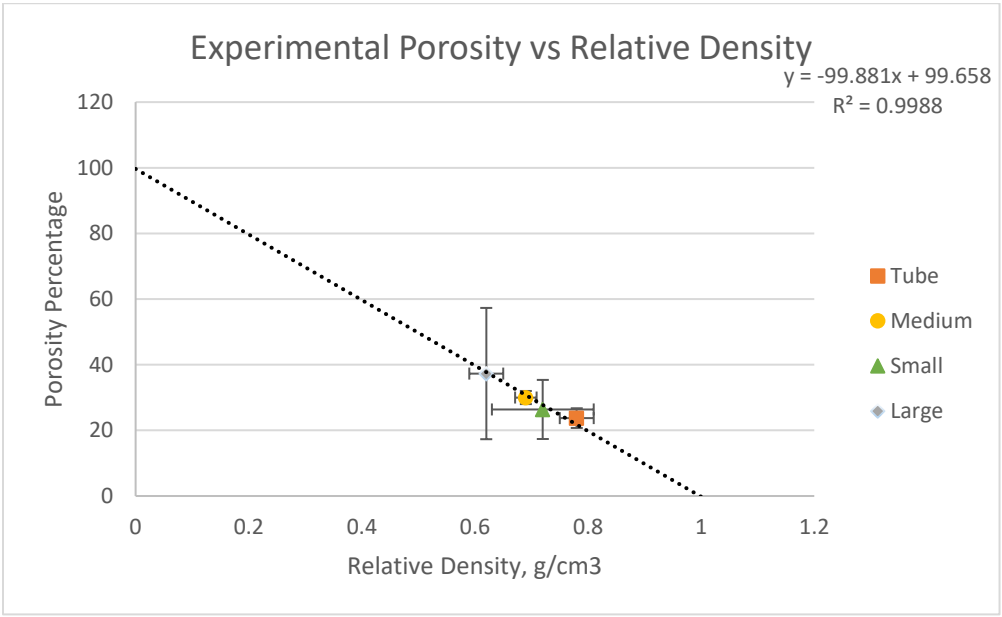

Figure 51: Percent porosity vs relative density.

CHAPTER FIVE: CONCLUSION

In this research produced magnesium foams that were synthesized by a new sacrificial spacer infiltration methods. The spacer material was developed to avoid reactions between the magnesium and spacer material and to be easily removed without damage to the magnesium foam.

1. Magnesium foam was successfully synthesized using the new spacer material. The relative densities for the magnesium alloy tube, and the foams made with small, medium, and large pore sizes are 0.78, 0.72,0.69, and 0.62 respectively.
2. A new material extrudable feed stock was produced for spacer material of magnesium AZ91D foams based on calcium carbonate.
3. Calcium carbonate was found to react to form calcium oxide during sintering as a result of the processing temperatures and atmosphere.
4. Infiltration with magnesium AZ91D result in minimal dissolution of the calcium oxide, except for in the smallest spacer material size, most likely to the increase in surface area.
5. Dissolving and removing the calcium oxide did not appear to degrade the magnesium AZ91D foam as shown by visual inspection and pH measurement.
6. Compression testing of the foam showed typical plateau behavior with an increasing yield stress of 19.95-57.7 MPa, and average pore volume ranges 4.75 x 10^{-3} – 5.1 x 10^{-4} mm^3 for the different spacer material sizes.

5.1 FUTURE RESEARCH

There are several potential paths for the spacer material to take with magnesium foam. The capability to make unique and controlled pore sizes yield the ability to control the mechanical properties desired from the magnesium foam. Some potential future research paths are:

1. Reclamation and recycling
2. Extruding spacer material
3. Pore size limit
4. Alloy development biocompatibility and degradability magnesium foam
5. Surface alloying pore walls
6. Deformation behavior foams of different porosity percentages under a various compression strain rates
7. Tailoring pore size and distribution to fit the desired properties needed in several different applications
8. Study of the kinetics of degradation of the magnesium foam in different environments

REFERENCES

Ashby, M., Evens , A., Fleck, N., Gibsion, L., Hutchinson, J., & Wadley, H. (2000). *Metal Foams: A Design Guild* . Butterworth-Heinemann.

Guohua, W., Fan, Y., Gao, H., Zhai, C., & Zhu, Y. P. (2005). The effect of Ca and rare earth elements on the microstructure, mechanical properties and corrosion properties of AZ91D. *Marerial Science and Engineering*, 255-263.

Gupta, N. (2015). Introduction to Foams. In N. Gupta, & P. Rohatgi, *Metal Matrix Syntactic Foams: Processing, Microstructure, Properties and Applications* (pp. 1-10). Lancaster : DEStretch Publications Inc. .

Haibin, J., Guangchun, Y., & Hongbin, L. (2007). Magnesium foam produced by foaming in melt. *Magnesium Technology* , 139-141.

Hao, G. L., Han, F. S., & Li, W. D. (2009). Processing and mechanical properties of magnesium foam. *Journal of Porous Matter*, 251-256.

Impression Across Europe: Solidification. (n.d.). Retrieved from ESA: http://www.spaceflight.esa.int/impress/text/education/Solidification/Question_Solidification_Immiscibles_Intermetallics_02.html#Top

Jiang, G., & He, G. (2014). A new approach ti the fabrication of porous magnesium with well-controlled 3D pore structure for orthopedic applications. *Material Science and Engineering*, 317-320.

Kalinkin, A., Balyakin, K., & Kalinkina, E. V. (2012). Kinetic and Thermodyanmic Patters of CaZrO3 Formation at sintering Zirconium Dioxide with Calcium Carbonate. *Russain Journal of Gerneral Chemistry* , 1753-1760.

Kananhashi, H., Mukai, T., Yamada, Y., Shinojima, K., Mabuchi, M., Aizawa, T., & Higashi, K. (2001). Experimental study for the improvement of crashworthiness in AZ91 magnesium foam controlling its microstructure. *Materials Science and Enginerring* , 283-287.

Kirkland, N., Kolbeinsson, I., Woodfield, T., & Staiger, G. D. (2011). Sunthesis and properties of topologicallu ordered porous magnesium. *Material Science and Engineering*, 1666-1672.

Maltais, A., Dube, D., Fiset, M., Laroche, G., & Turgeon, S. (2004). Improvements in the metallography of as-cast AZ91 alloy. *Materials Characterization* , 103-119.

Mukai, T., Kanahashi , H., Yamada, Y., Shinojima, K., Mabuchi, M., Nieh, T. G., & Higashi, K. (1999). Dynamic Compressive Behavior of an Ultra-Lightweight Magnesium Foam. *Scripta Materialia*, 365-371.

Someya. (1993). *United States Patent No. 5187125.*

Stephani, G. (2010). Cellular Metals for Functional Applications – an Overview. *World Congress – Foams & Porous Materials.* Fraunhofer-Institute for Manufacturing and Advanced Materials Research . Retrieved from Fraunhofer-Institute for Manufacturing and Advanced Materials Research .

Wang, X., Li, Z., Haung, Y., Wang, X., & Han, F. (2014). Processing of Magnesium Foams by Weakly Corrosive and Highly Flexable Space Holder Material. *Materals and Design*, 324-329.

Wen, C., Yamada, Y., Shimojima, K., Chino, Y., Hosokawa, H., & Mabuchi, M. (2004). Compressibility of porous magnesium foam: dependancy on porosity and pore size. *Materials Letters*, 357-360.

Wieser, H. (2007, April). Chemistry of Gluten Proteins. *Food MIcrobiology, 24*(2), 115-119. Retrieved from Science Direct : http://www.sciencedirect.com/science/article/pii/S0740002006001535

Witte, E., Ulrich, H., Rudert, M., & Willbold, E. (2006). Biodegradable magnesium scaffolds: Part1: appropriate inflammatory response. *Wiley InterScience*.

Yamada, Y., Shimojima, K., Sakaguchi, Y., Mabuchi, M., Nakaurma, M., Asahina, T., . . . Higashi, K. (1999). Processing of an open-cellular AZ91 magnesium alloy with a low density of 0.05g/cm^3. *Material Science Letters*, 1477-1480.

Yang, C.-W. (2013, June 10). *Tensile Mechanical Properties and Failure Behaviors of Friction Stir Processing (FSP) Modified Mg-Al-Zn and Dual-Phase Mg-Li-Al-Zn Alloys.* Retrieved from InTech: https://www.intechopen.com/books/materials-science-advanced-topics/tensile-mechanical-properties-and-failure-behaviors-of-friction-stir-processing-fsp-modified-mg-al-z

Yue, X.-Z., & Hur, B.-Y. (2012). Effect of the holding temperature and vacuum pressure for the open cell Mg alloy foams. *Korea Journal of Materials Research*, 309-314.

Zhang, X., Li, X.-W., Li, J.-G., & Sun, X.-D. (2014). Preparation and mechanical property of a noval 3D porus magnesium scaffold for bone tissue engineering. *Material Science and Engineering* , 362-367.

Zulianit, D. J., & Closset, B. (1989). *Patent No. EP 0343012 A2.*

APPENDIX A

DSC-TGA

Table 6 shows the data from running the flour powder, calcium carbonate powder, and coarse crushed noodles run on the DSC-TGA in CO_2 atmosphere.

Table 6: The first derivative of the weight/time from the DSC-TGA. The table shows the temperature for the reaction changes for the varity of samples tested in CO_2 atmosphere.

CO_2	dWt%/dt Temperature (C)				
Sample type		Water Evaporated	Flour to Carbon	Carbon Degradation	$CaCO_3$-->$CaO + CO_2$
Flour (powder)	Average	96	309	1022	N/A
	StDev	2.3	0.3	5.0	N/A
$CaCO_3$ (powder)	Average	N/A	N/A	N/A	957
	StDev	N/A	N/A	N/A	1.4
Flour-$CaCO_3$	Average	89	305	823	957
	StDev	1.1	1.0	3.2	1.4

General DSC-TGA Graphs Chosen at Random

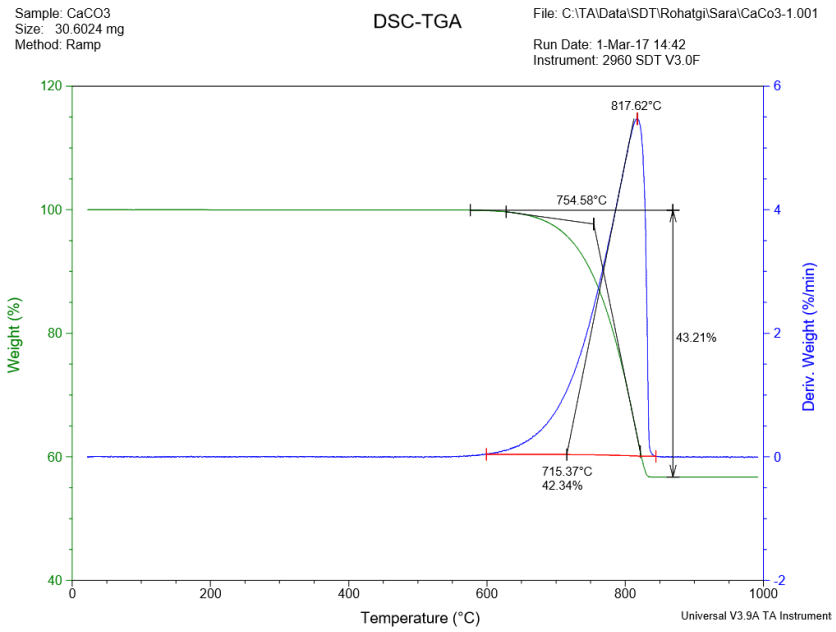

Figure 52: DSC-TGA graph of calcium carbonate powder in air atmosphere

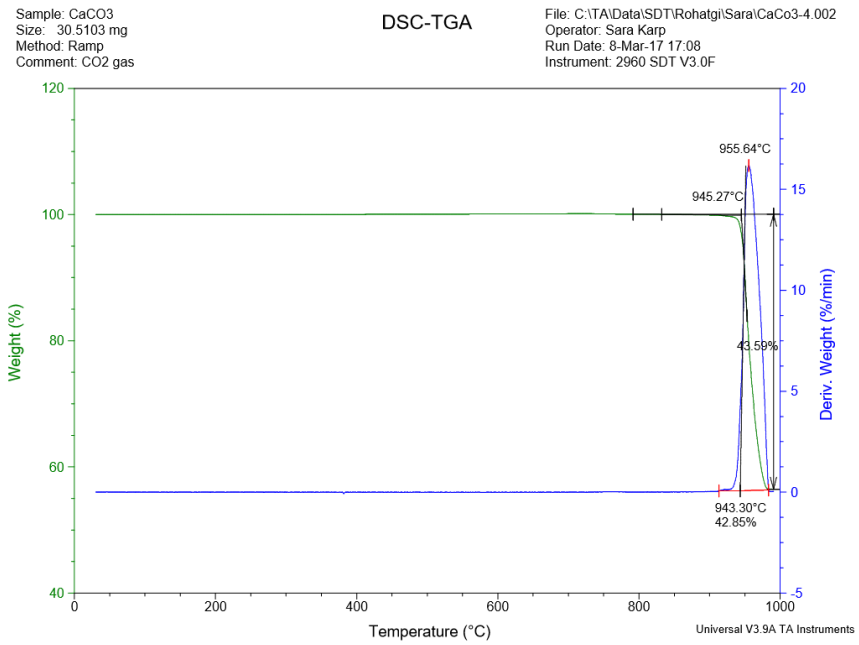

Figure 53: DSC-TGA graph of calcium carbonate powder in CO_2 atmosphere

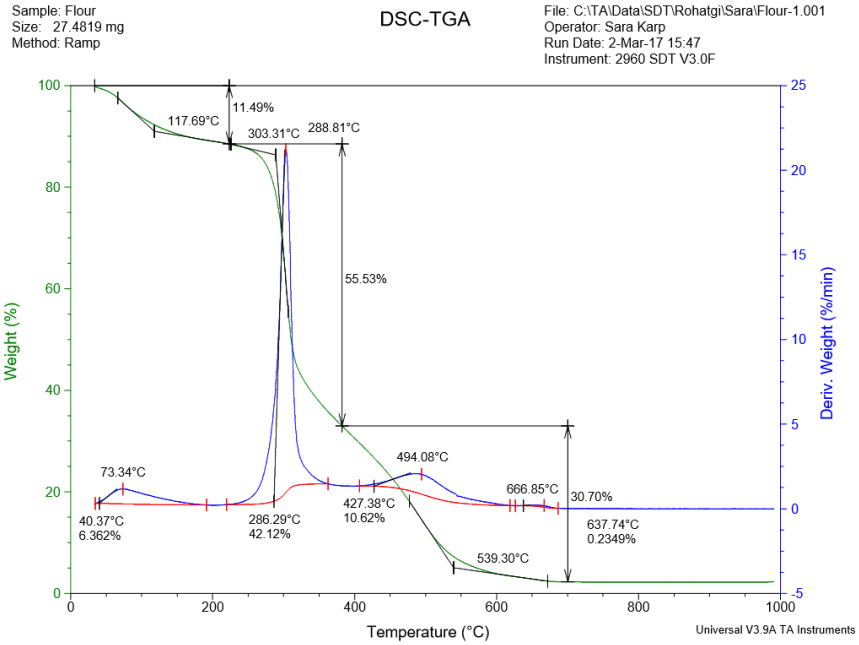

Figure 54: DSC-TGA graph of flour powder in air atmosphere

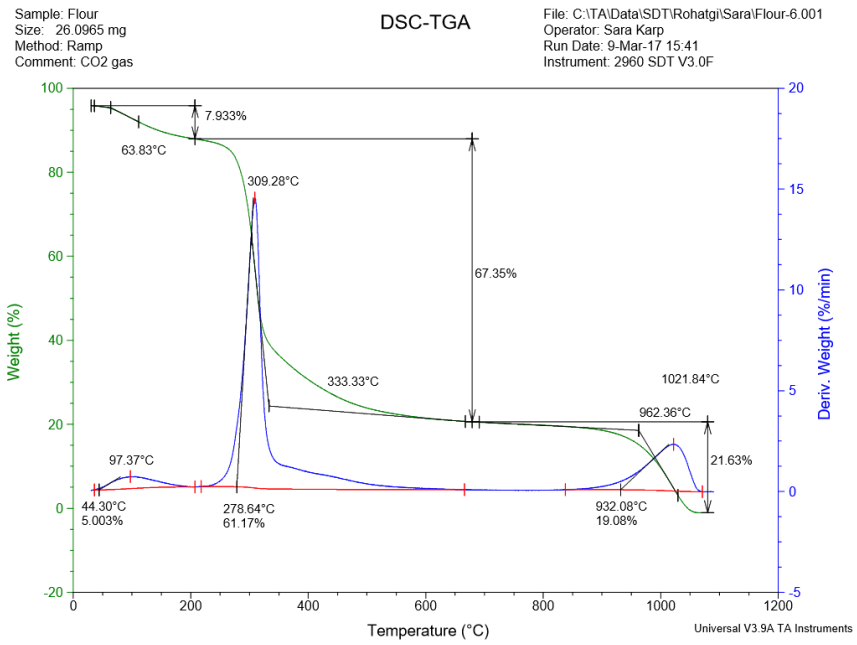

Figure 55: DSC-TGA graph of flour powder in CO_2 atmosphere

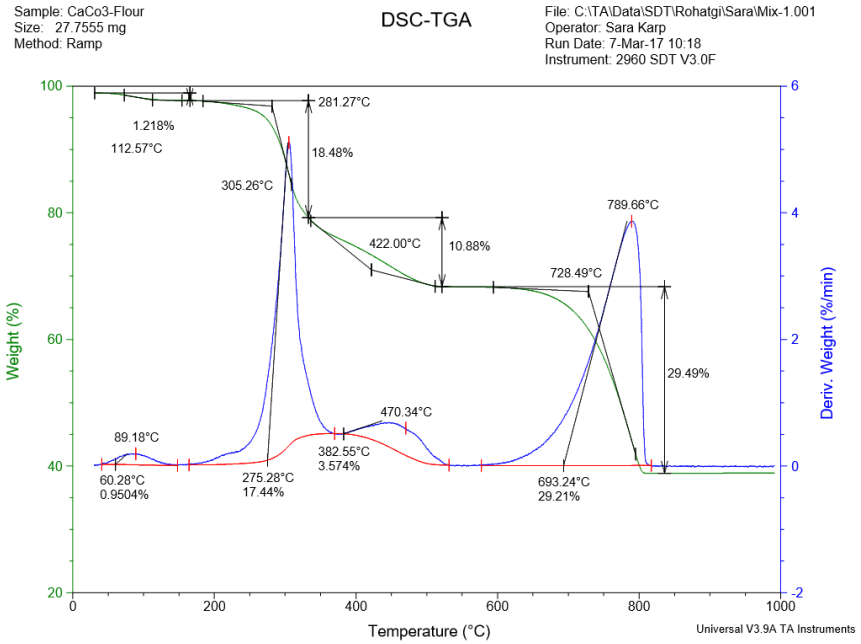

Figure 56: DSC-TGA graph of coarse crushed noodle mix in air atmosphere

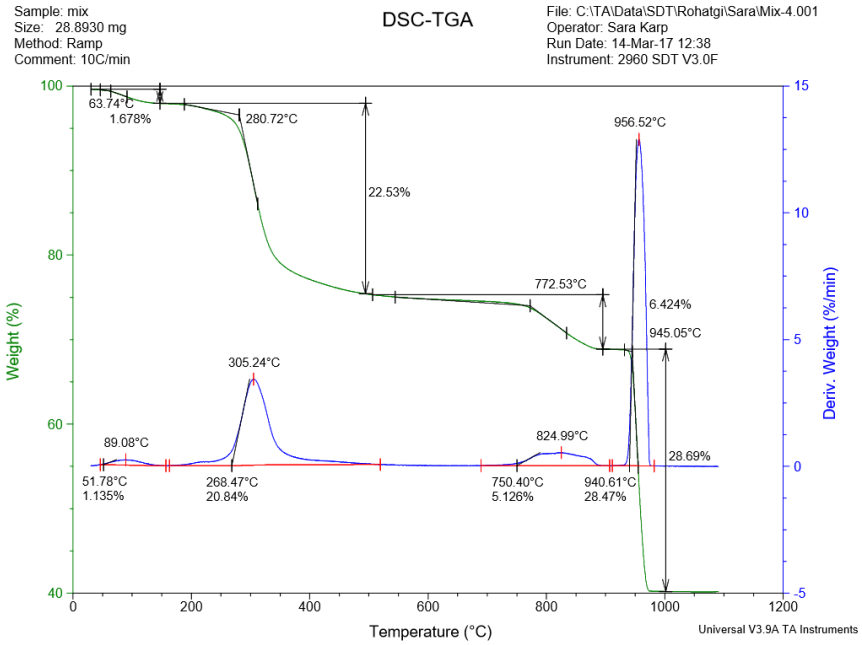

Figure 57:DSC-TGA graph of coarse crushed noodle mix in CO_2 atmosphere

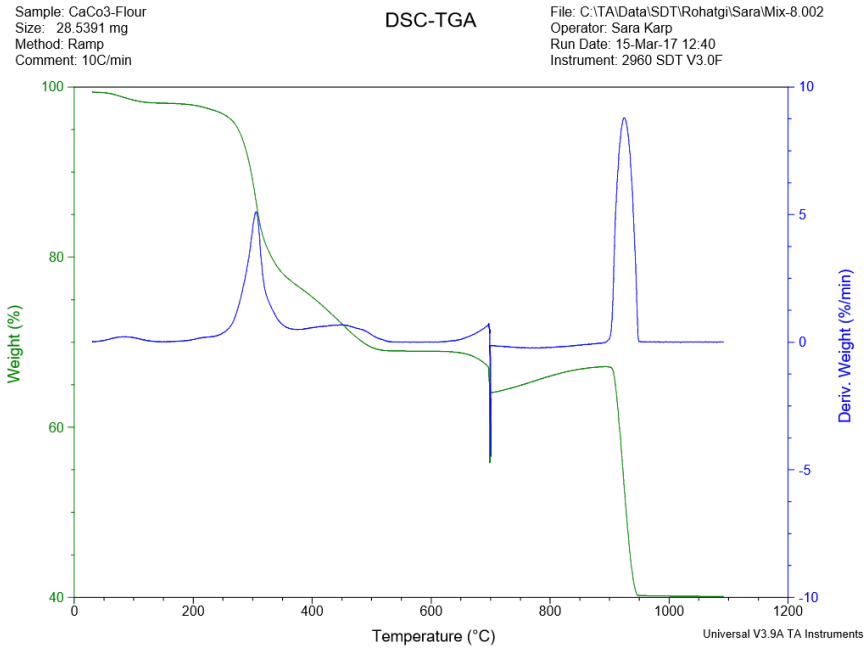

Figure 58: DSC-TGA graph of coarse crushed noodle mix in air atmosphere until 700ºC then switched to CO_2 atmosphere

APPENDIX B

SEM EDS

Below are the individual tables for the SEM-EDS samples with the images for each spectrum location.

Ingot Stock Magnesium Sample

Table 7: The EDS reading of the different spectrafrom the ingot magnesium.

Ingot	Type of spectrum	Phases	Mg	Al	Zn	Ca	O
1	Rectangular	γ+ε	84	12.26	-	0.68	0.18
2	Point	γ+ε	87.51	15.14	-	0.03	0.02
3	Point	γ+β	55.47	38.54	5.23	0.06	-
4	Point	γ+ε	95.68	3.39	-	-	-

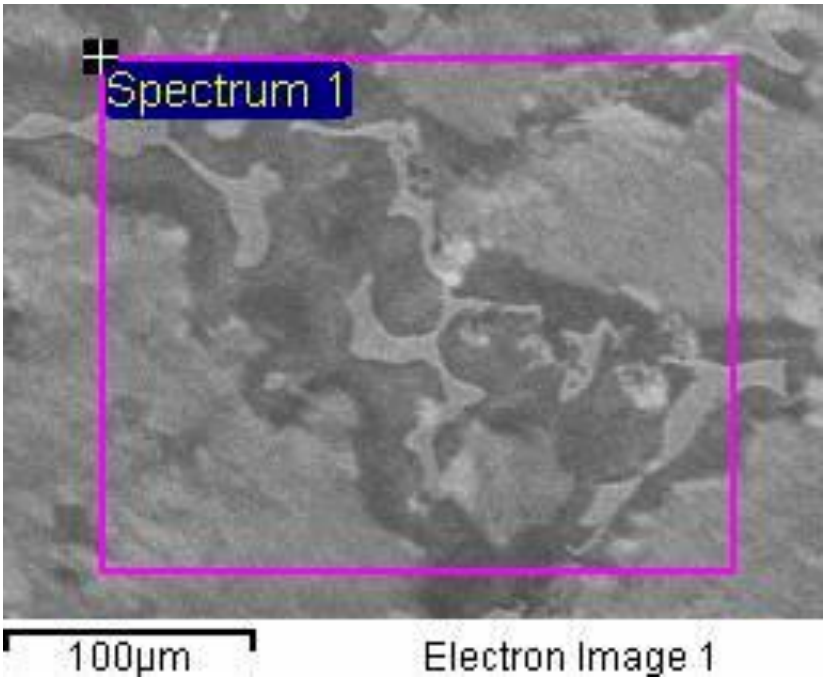

Figure 59:Ingot magnesium JEOL SEM 400x, WD 12 mm, 15 kV, showing spectrum 1.

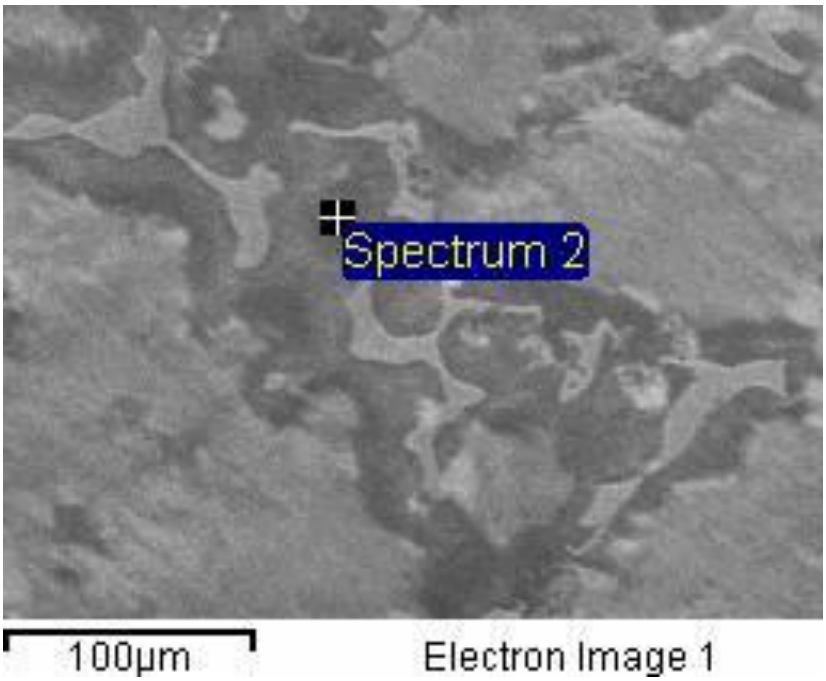

Figure 60: Ingot magnesium JEOL SEM 400x, WD 12 mm, 15 kV, showing spectrum 2.

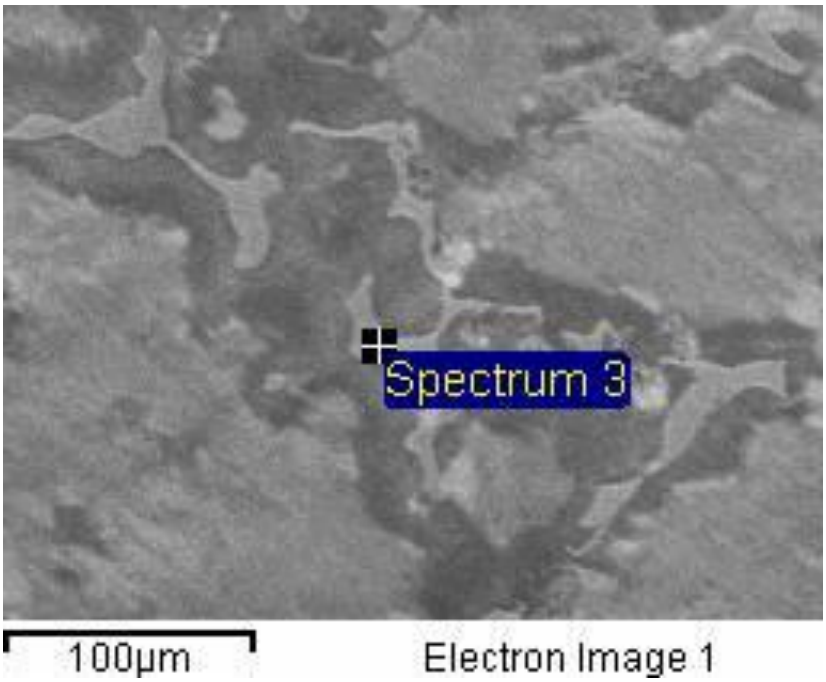

Figure 61: Ingot magnesium JEOL SEM 400x, WD 12 mm, 15 kV, showing spectrum 3.

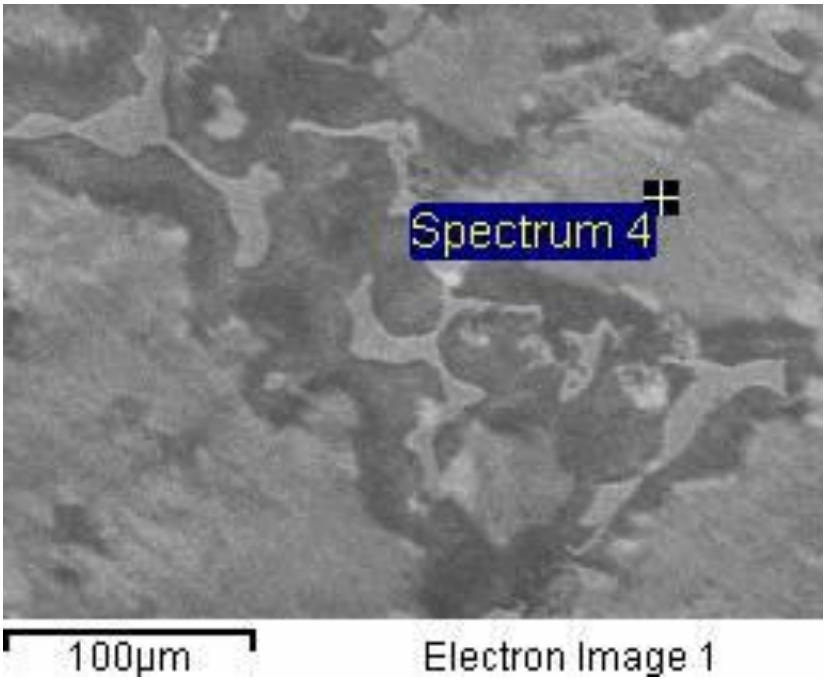

Figure 62: Ingot magnesium JEOL SEM 400x, WD 12 mm, 15 kV, showing spectrum 4.

Cast Magnesium Machined Tube Sample

Table 8: The EDS reading of the different spectrafrom the cast tube magnesium.

Tube	Type of spectrum	Phases	Mg	Al	Zn	Ca	O
1	Rectangular	γ+ε	85.81	15.02	-	-	-
2	Point	γ+ε	94.61	5.09	-	-	-
3	Point	γ+ε	81.11	17.88	-	-	1.46
4	Point	γ+ε	91.67	7.92	-	0.16	0.25

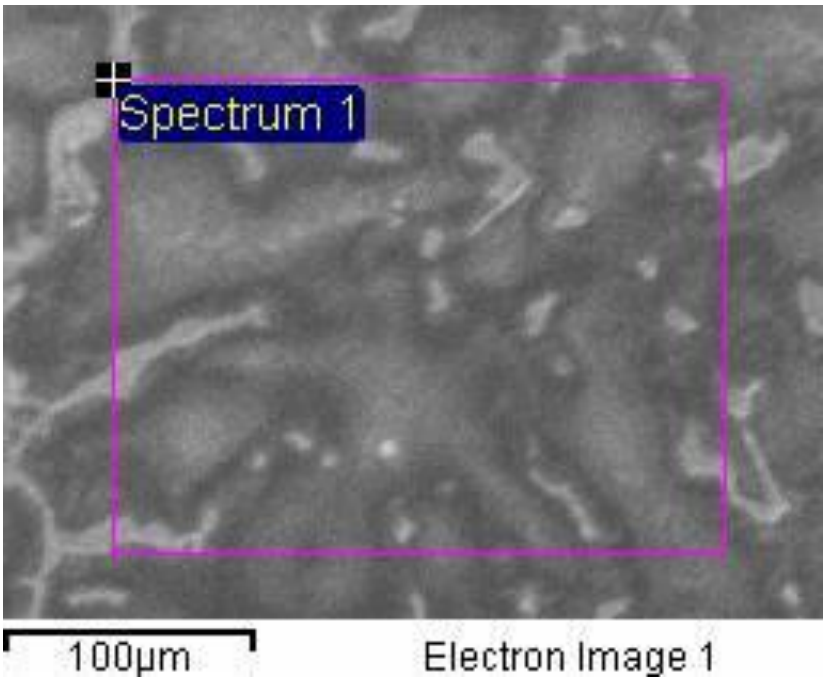

Figure 63: Tube magnesium JEOL SEM, 400x, WD 13mm, 15vK spectrum 1.

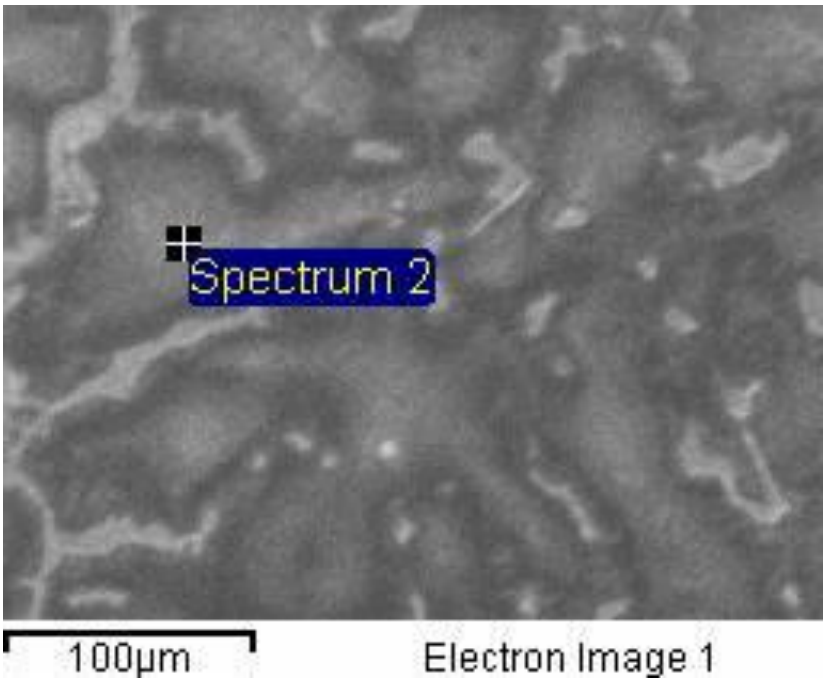

Figure 64: Tube magnesium JEOL SEM, 400x, WD 13mm, 15vK spectrum 2.

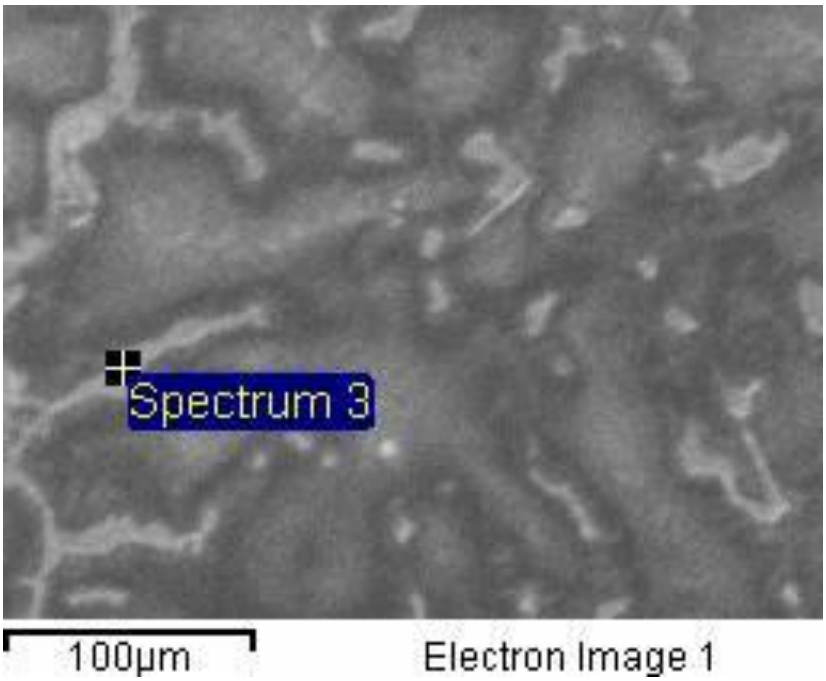

Figure 65: Tube magnesium JEOL SEM, 400x, WD 13mm, 15vK spectrum 3.

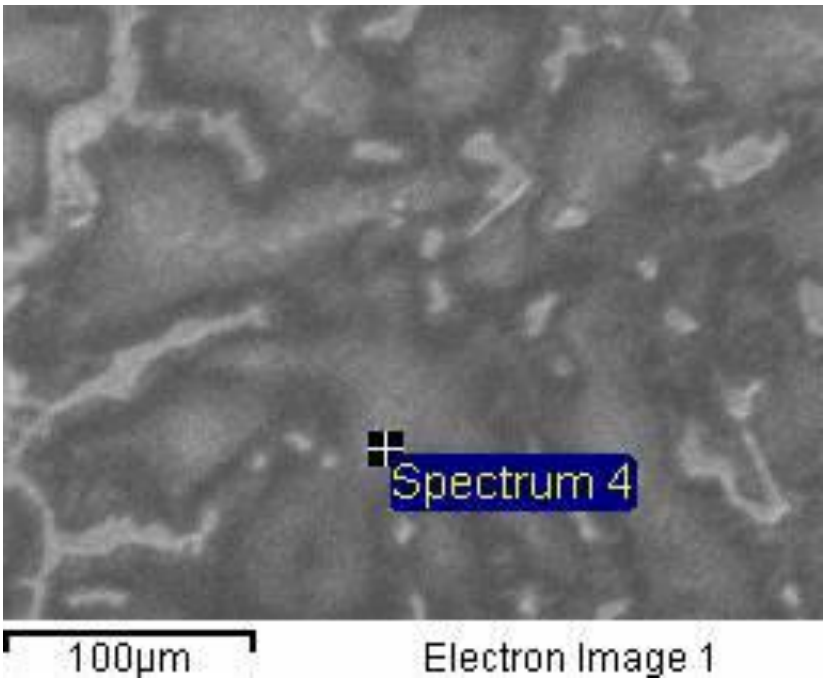

Figure 66: Tube magnesium JEOL SEM, 400x, WD 13mm, 15vK spectrum 4.

Cast Magnesium Sample

Table 9: The EDS reading of the different spectrafrom the cast magnesium.

Cast	Type of spectrum	Phases	Mg	Al	Zn	Ca	O
1	Rectangular	γ+ε	84.03	15.97	-	-	-
2	Point	γ+ε	83.87	16.13	-	-	-
3	Point	γ+ε	93.34	7.66	-	-	-
4	Point	γ+ε	83.45	16.55	-	-	-

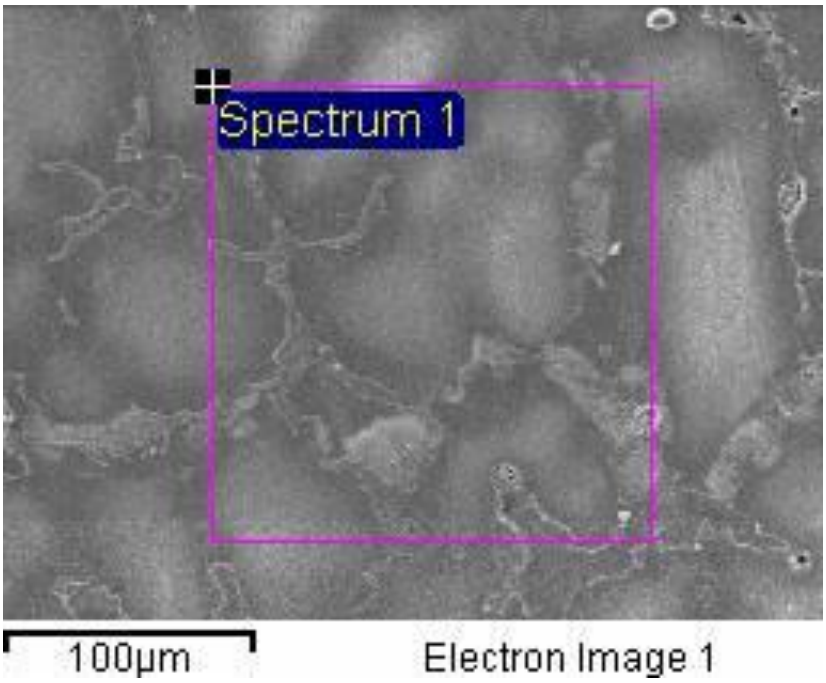

Figure 67: Cast magnesium, JEOL SEM, 400x, WD 12mm, 15vK spectrum 1.

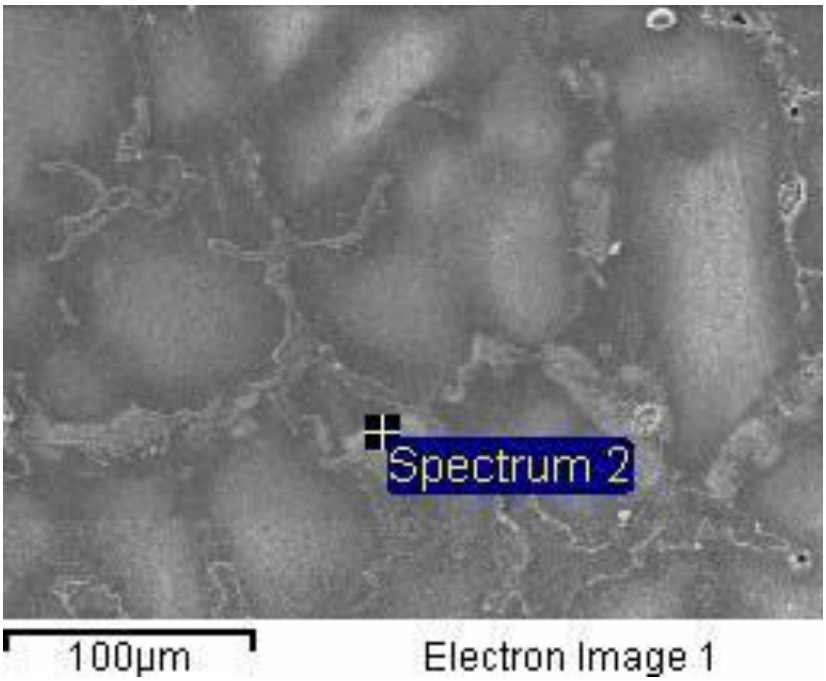

Figure 68: Cast magnesium, JEOL SEM, 400x, WD 12mm, 15vK spectrum 2.

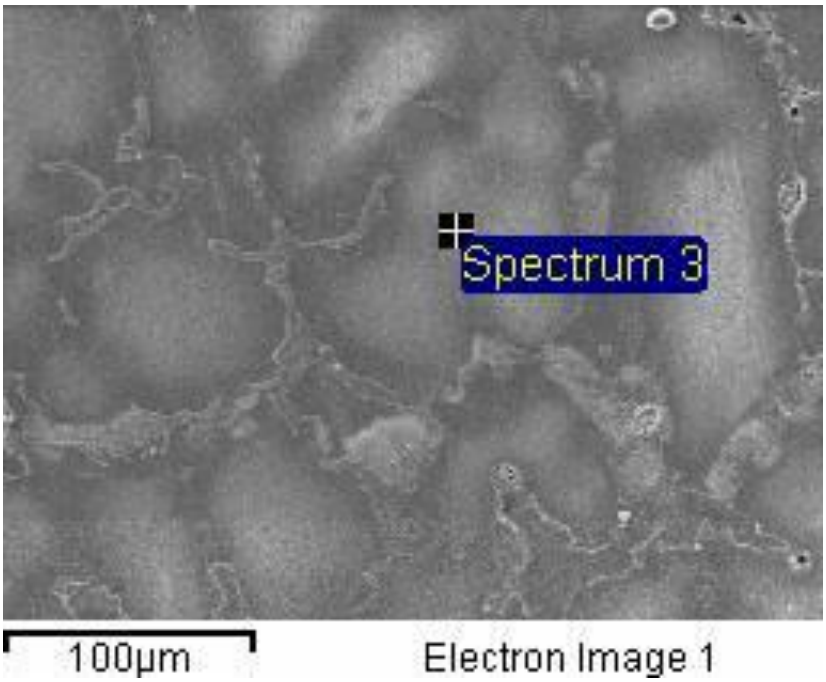

Figure 69: Cast magnesium, JEOL SEM, 400x, WD 12mm, 15vK spectrum 3.

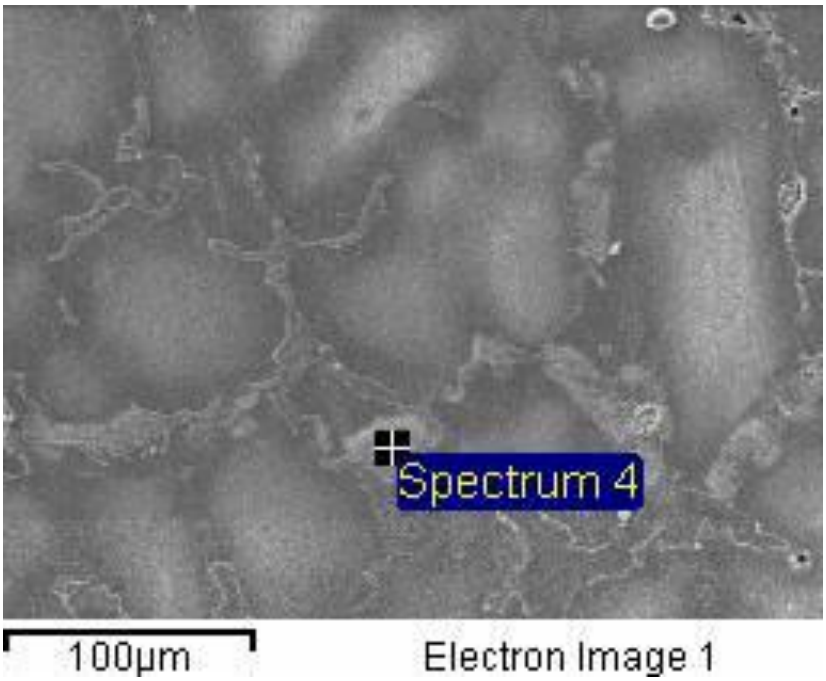

Figure 70: Cast magnesium, JEOL SEM, 400x, WD 12mm, 15vK spectrum 4.

Large Pore Size Magnesium Sample

Location One: Cell Wall

Table 10: The EDS reading of the different spectrafrom the pore large spacer magnesium sample.

Large Pore	Type of spectrum	Phases	Mg	Al	Zn	Ca	O
1	Rectangular	γ+ε	84.42	15.55	-	0.32	-
2	Point	γ+ε	84.69	13.98	-	0.012	0.41
3	Point	γ+ε	87.05	12.04	-	0.21	0.7
4	Point	γ+ε	87.3	12.52	-	0.48	-
5	Point	γ+ε	95.89	3.09	-	2.19	-

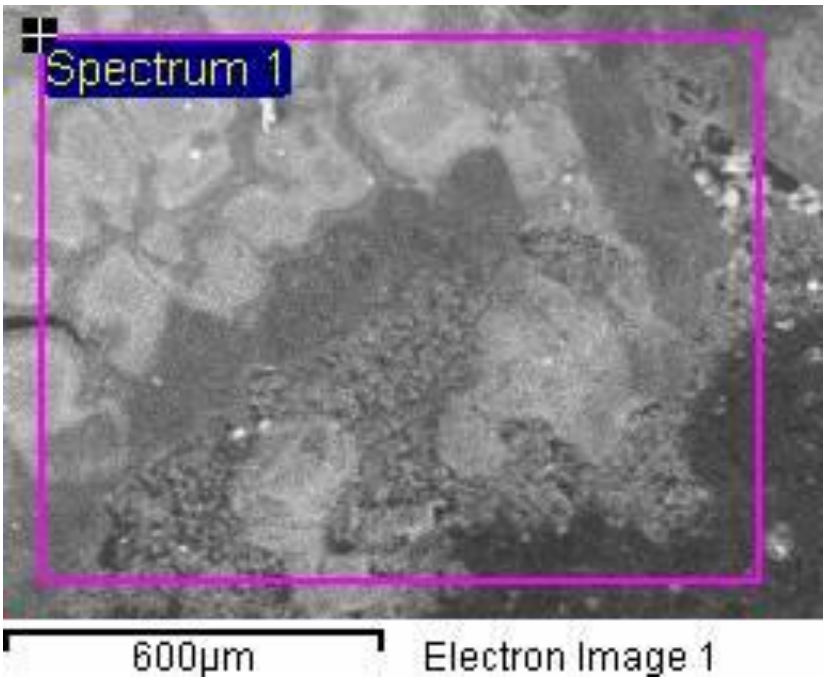

Figure 71: Large spacer foam magnesium JEOL SEM, 100x, WD 13mm, 15vK. Image is showing section of magnesium directly next to a pore and machined outer diameter spectrum 1.

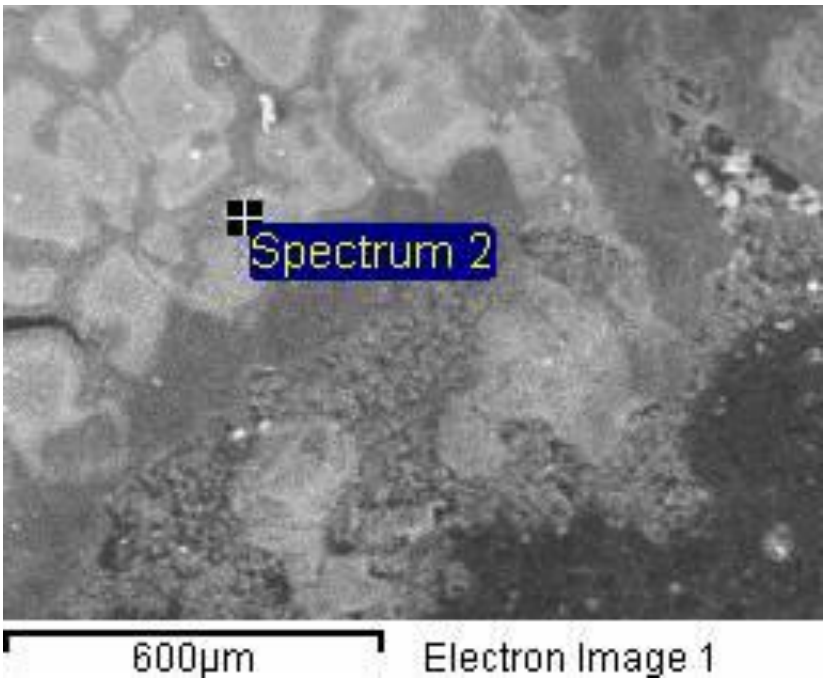

Figure 72: Large spacer foam magnesium JEOL SEM, 100x, WD 13mm, 15vK. Image is showing section of magnesium directly next to a pore and machined outer diameter spectrum 2.

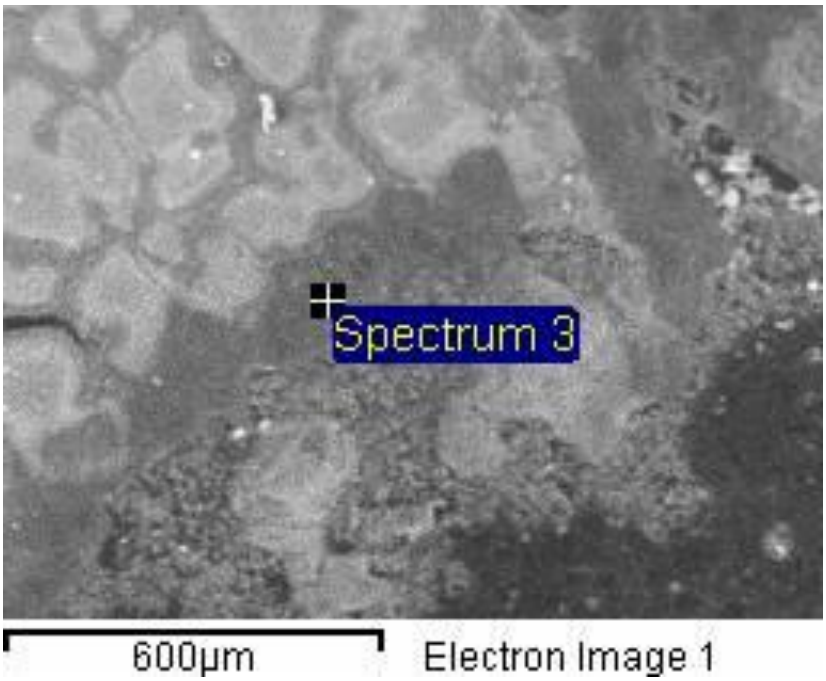

Figure 73: Large spacer foam magnesium JEOL SEM, 100x, WD 13mm, 15vK. Image is showing section of magnesium directly next to a pore and machined outer diameter spectrum 3.

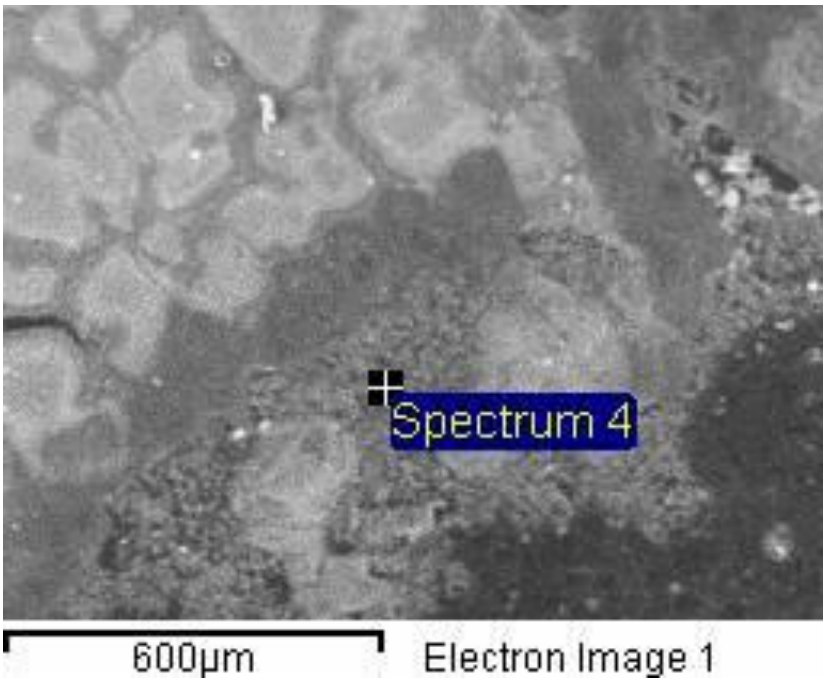

Figure 74: Large spacer foam magnesium JEOL SEM, 100x, WD 13mm, 15vK. Image is showing section of magnesium directly next to a pore and machined outer diameter spectrum 4.

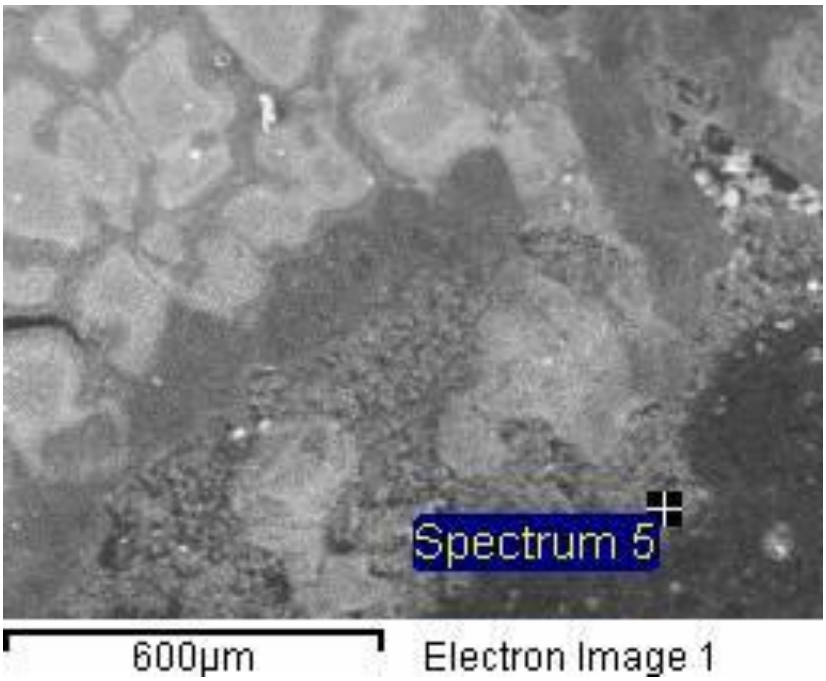

Figure 75: Large spacer foam magnesium JEOL SEM, 100x, WD 13mm, 15vK. Image is showing section of magnesium directly next to a pore and machined outer diameter spectrum 5.

Location Two: Outer Diameter

Table 11: The EDS reading of the different spectrafrom the outer diameter large spacer magnesium sample.

Large							
OD	Type of spectrum	Phases	Mg	Al	Zn	Ca	O
1	Recangular	γ+ε	75.58	11.2	-	13.01	0.2
2	Point	γ+ε	93.85	5.71	-	0.33	0.12
3	Point	γ+ ε	91.5	8.01	-	-	0.98
4	Point	Ca/C, ε	3.92	0.06	-	94.49	1.83
5	Point	Ca/C	35.83	1.16	-	69.66	-
6	Point	CaO, Al	-	20.8	-	36.02	48.73

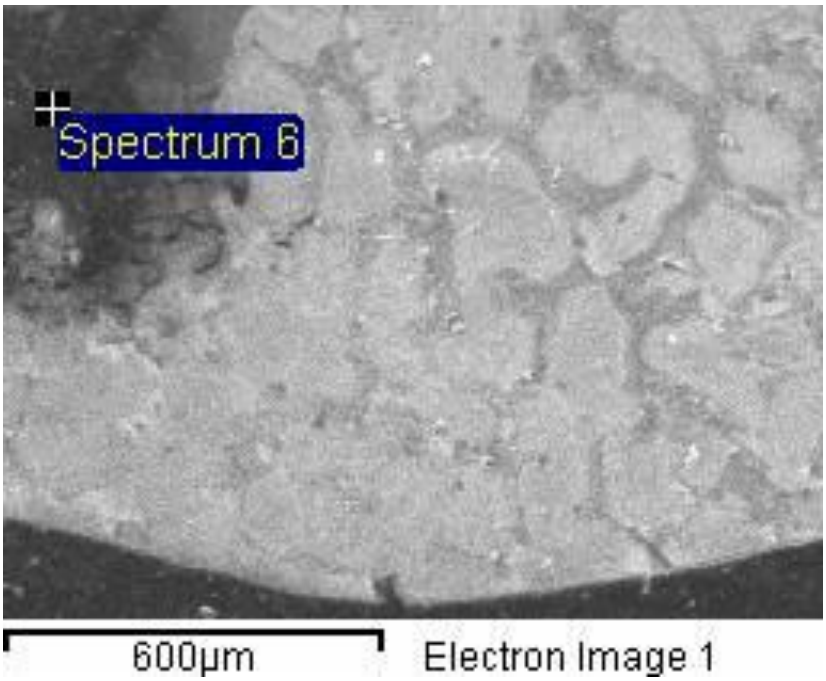

Figure 76: Large spacer foam magnesium JEOL SEM, 100x, WD 13mm, 15vK. Image is showing section of magnesium directly next to a pore and machined outer diameter spectrum 6.

Medium Pore Size Magnesium Sample

Location One: Center

Table 12: The EDS reading of the different spectrafrom the center of the middle spacer magnesium sample.

Medium							
Center	Type of spectrum	Phases	Mg	Al	Zn	Ca	O
1	Rectangular	γ+ε	84.05	15.53	-	0.42	-

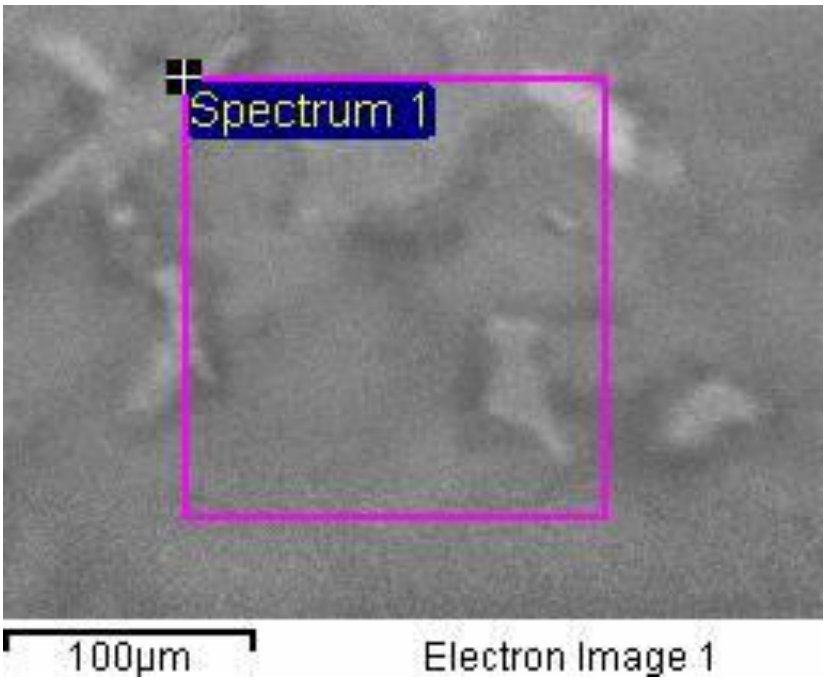

Figure 77: Medium spacer foam magnesium JEOL SEM, 400x, WD 16mm, 15vK. Image is showing the center section of magnesium spectrum 1.

Location Two: Cell Wall

Table 13: The EDS reading of the different spectrafrom the pore of the middle spacer magnesium sample.

Medium					
Pore	Type of spectrum	Phases	Mg	Al	Ca
1	Rectangular	γ+ε	88.34	11.31	0.35
2	Point	γ+ε	85.99	19.29	-
3	Point	γ+ε	93.3	6.4	0.3
4	Point	γ+ε	93.5	6.62	-

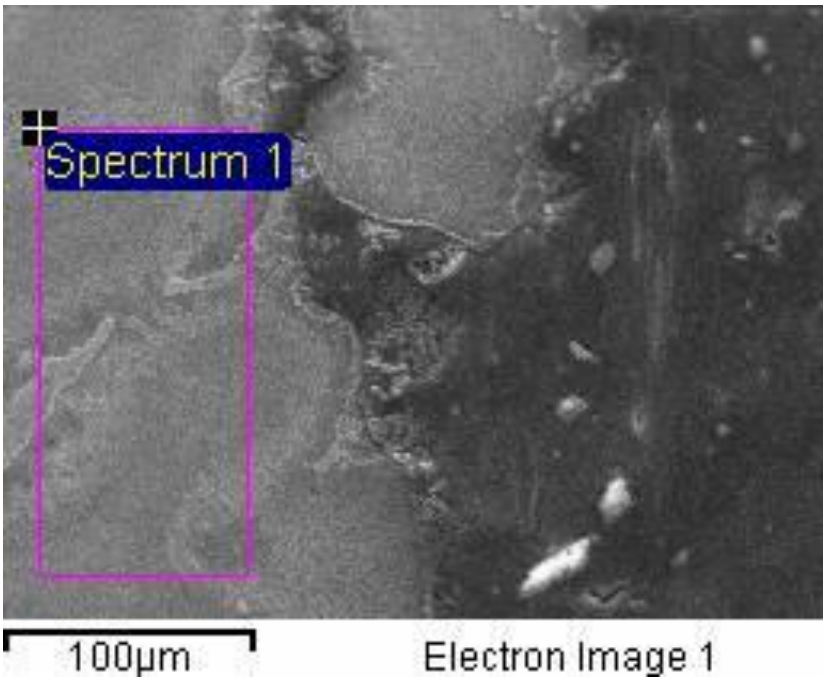

Figure 78: Medium spacer foam magnesium JEOL SEM, 400x, WD 15mm, 15vK. Image is showing a section of magnesium next to a pore spectrum 1.

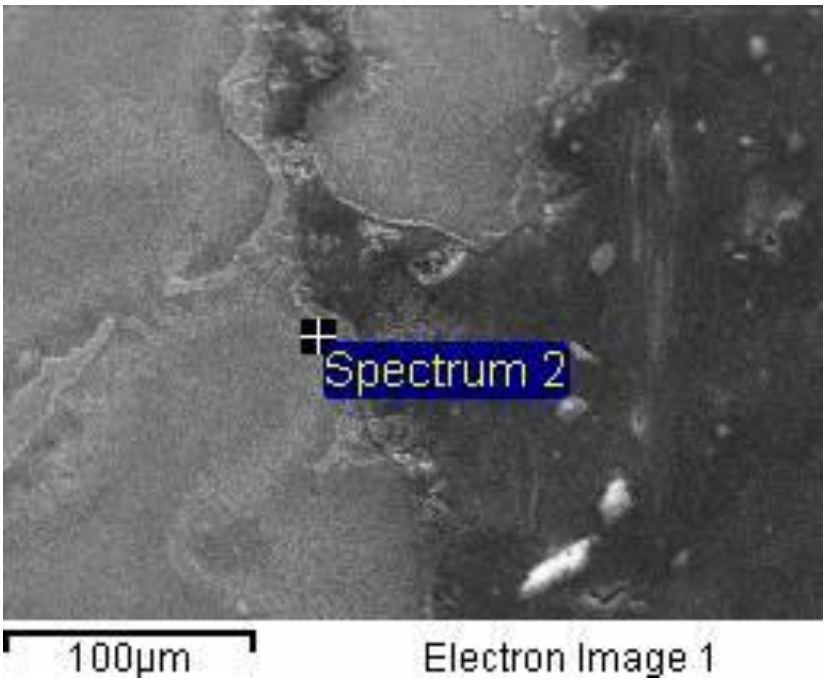

Figure 79: Medium spacer foam magnesium JEOL SEM, 400x, WD 15mm, 15vK. Image is showing a section of magnesium next to a pore spectrum 2.

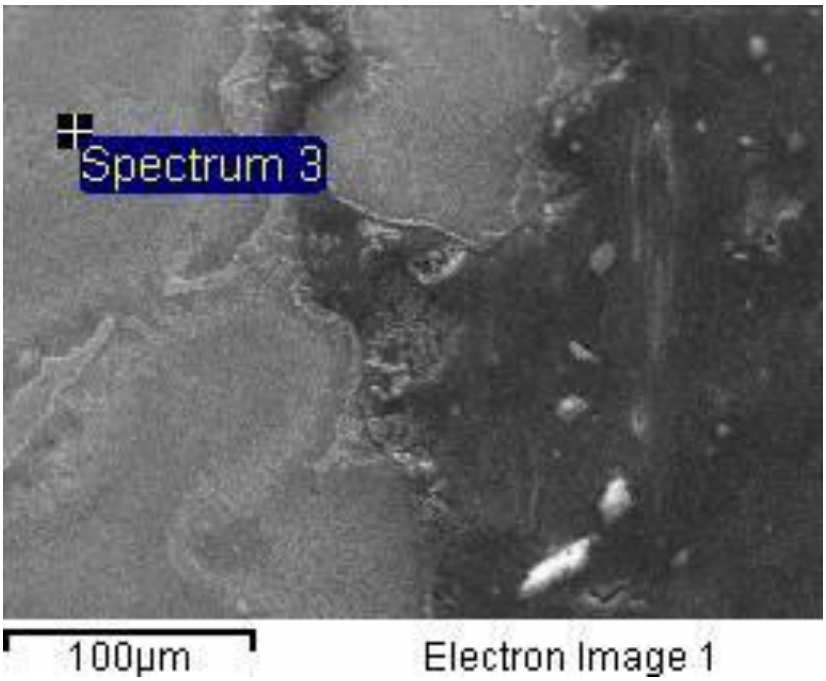

Figure 80: Medium spacer foam magnesium JEOL SEM, 400x, WD 15mm, 15vK. Image is showing a section of magnesium next to a pore spectrum 3.

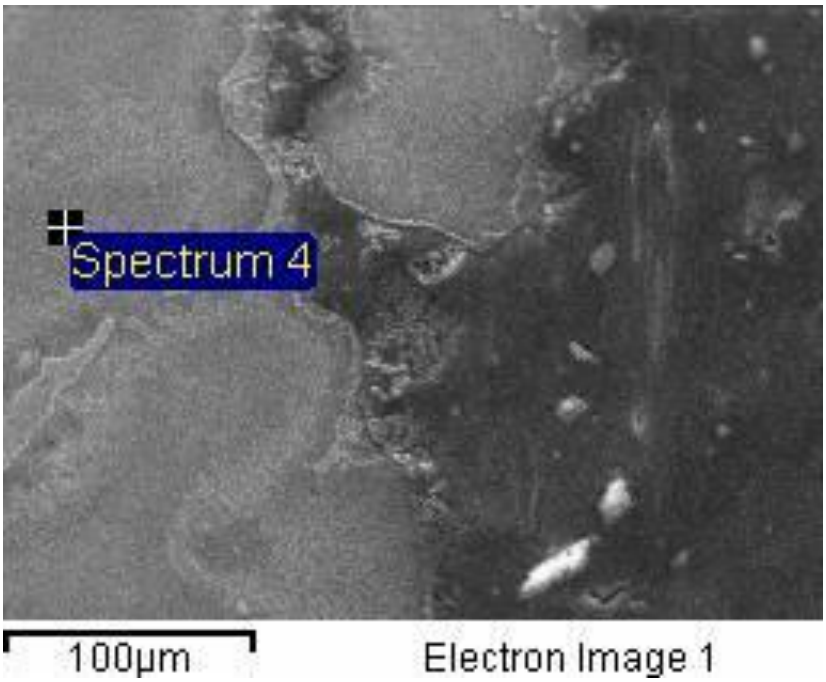

Figure 81: Medium spacer foam magnesium JEOL SEM, 400x, WD 15mm, 15vK. Image is showing a section of magnesium next to a pore spectrum 4.

Small Pore Size Magnesium Sample

Location One: Outer Diameter

Table 14: The EDS reading of the different spectrafrom the out diameter of a small spacer magnesium sample.

Small							
OD	Type of spectrum	Phases	Mg	Al	Ca	O	C
1	Rectangular	γ+ε	81.56	9.26	1.37	7.81	-
2	Point	Mount	-	-	3.48	24.64	71.88
3	Point	γ+ε	87.35	7.56	0.54	4.55	-
4	Point	γ+ε	92.07	7.93	-	-	-
5	Point	γ+ε	73.38	22.42	-	4.2	-

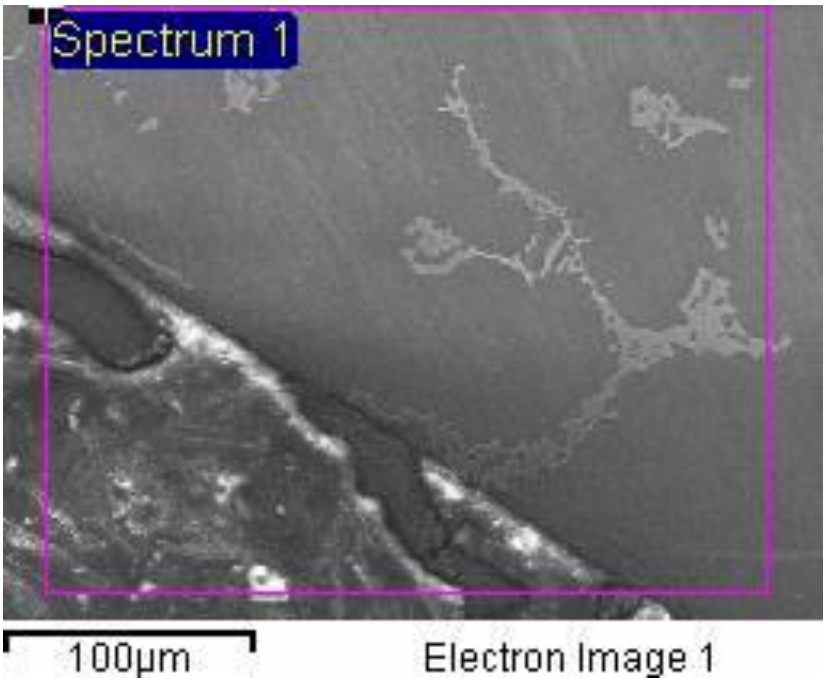

Figure 82: Small pore size foam magnesium JEOL SEM, 400x, WD 16mm, 15vK. Image is showing a section of magnesium next to outer diameter. Spectrum 1.

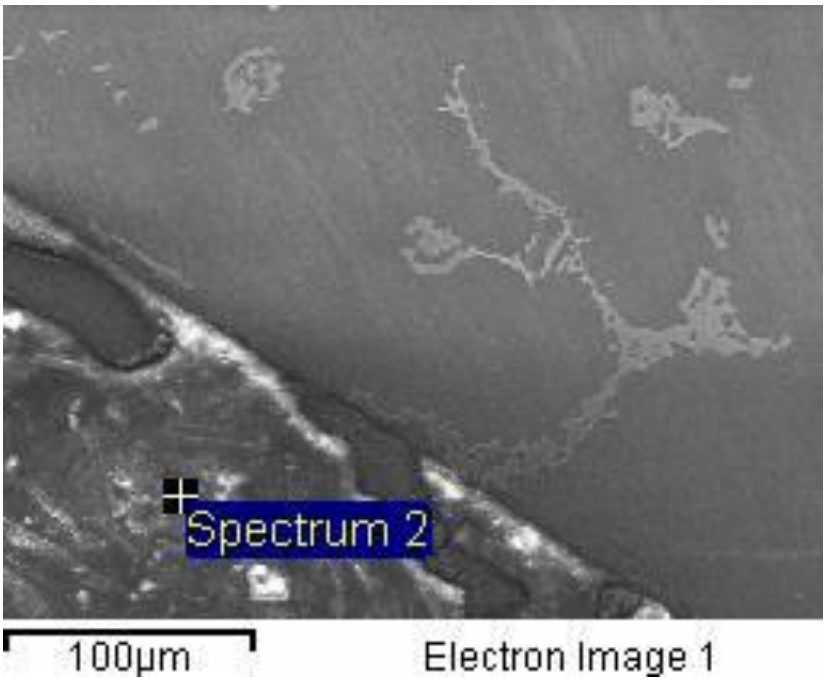

Figure 83: Small pore size foam magnesium JEOL SEM, 400x, WD 16mm, 15vK. Image is showing a section of magnesium next to outer diameter. Spectrum 2.

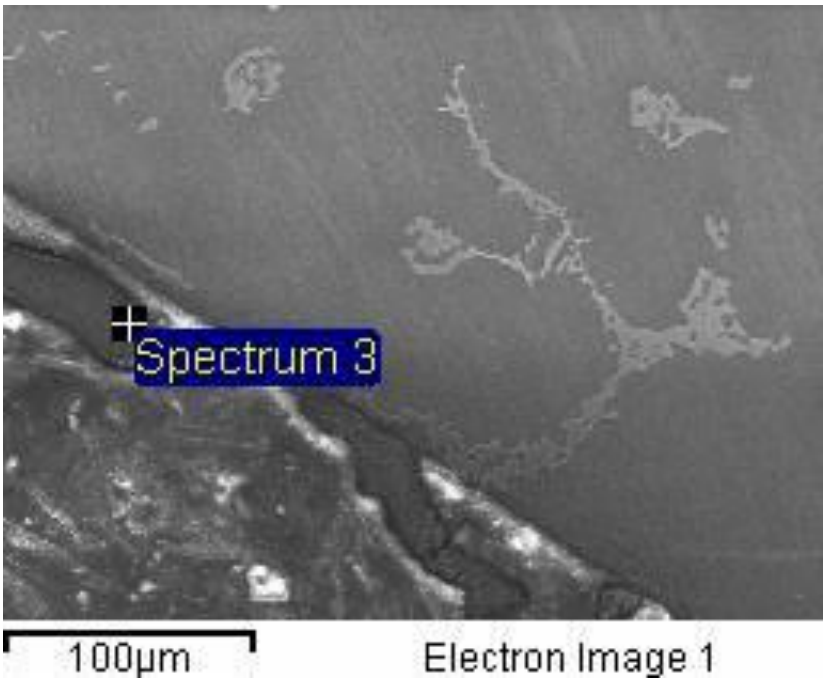

Figure 84: Small pore size foam magnesium JEOL SEM, 400x, WD 16mm, 15vK. Image is showing a section of magnesium next to outer diameter. Spectrum 3.

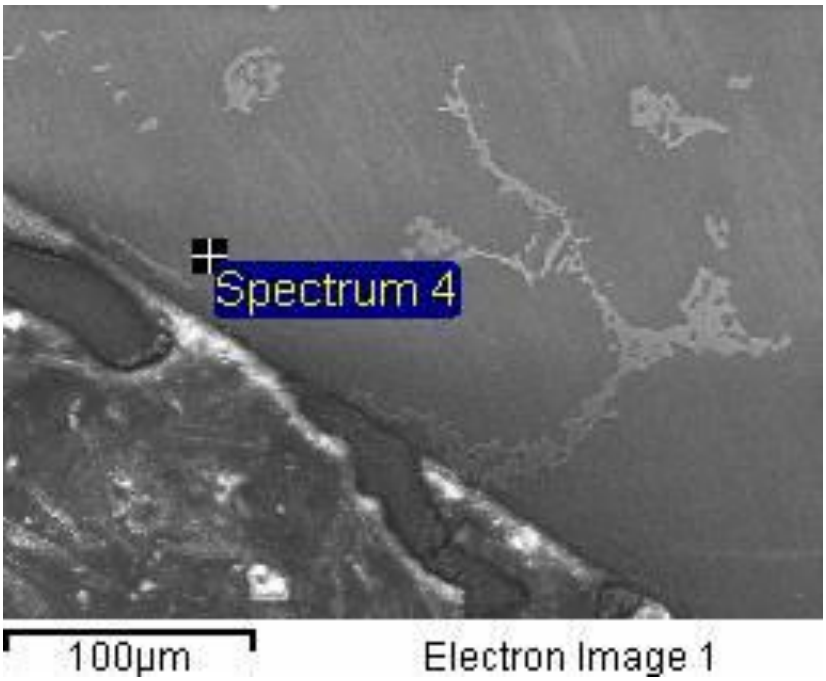

Figure 85: Small pore size foam magnesium JEOL SEM, 400x, WD 16mm, 15vK. Image is showing a section of magnesium next to outer diameter. Spectrum 4.

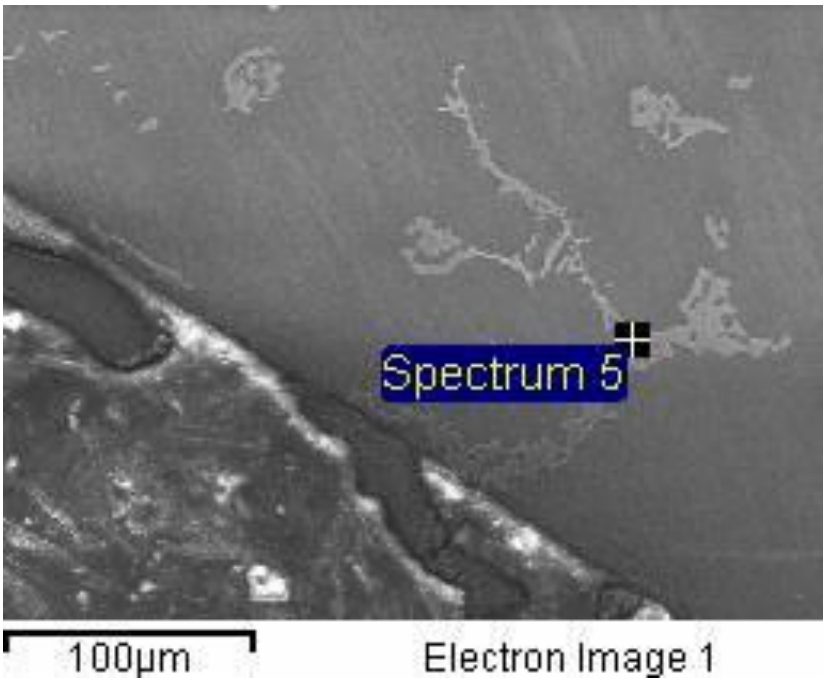

Figure 86: Small pore size foam magnesium JEOL SEM, 400x, WD 16mm, 15vK. Image is showing a section of magnesium next to outer diameter. Spectrum 5.

Location Two: Cell Wall Two

Table 15: The EDS reading of the different spectrafrom the pore of a small spacer magnesium sample.

Small								
Pore 1	Type of spectrum	Phases	Mg	Al	Zn	Ca	O	Cr
1	Rectangular	γ+ε	82.54	15.11	-	2.79	-	-
2	Point	CaO, Cr	-	-	-	16.28	82.4	1.31
3	Point	Al_4Ca	7.14	53.49	-	39.74	-	-
4	Point	γ+ε	93.19	7.72	-	0.17	0.13	-
5	Point	Al_4Ca,ε	27.95	48.95	-	23.56	-	-
6	Point	γ+ε	92.56	7.72	-	-	-	-
7	Point	γ, Al_4Ca, Zn	54.06	36.02	7.62	2.31	-	-

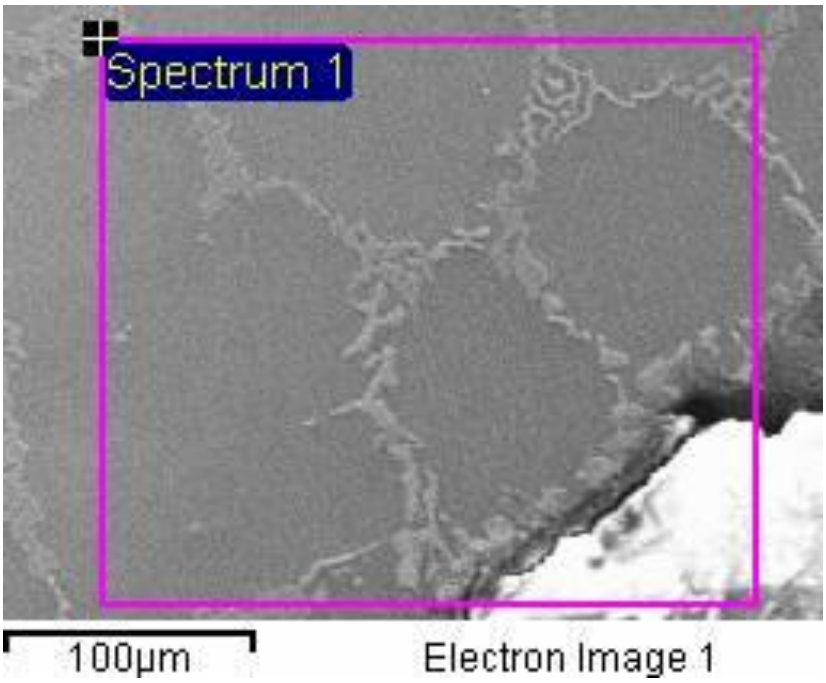

Figure 87: Small spacer foam magnesium JEOL SEM, 400x, WD 16mm, 15vK. Image is showing a section of magnesium next to a pore spectrum 1.

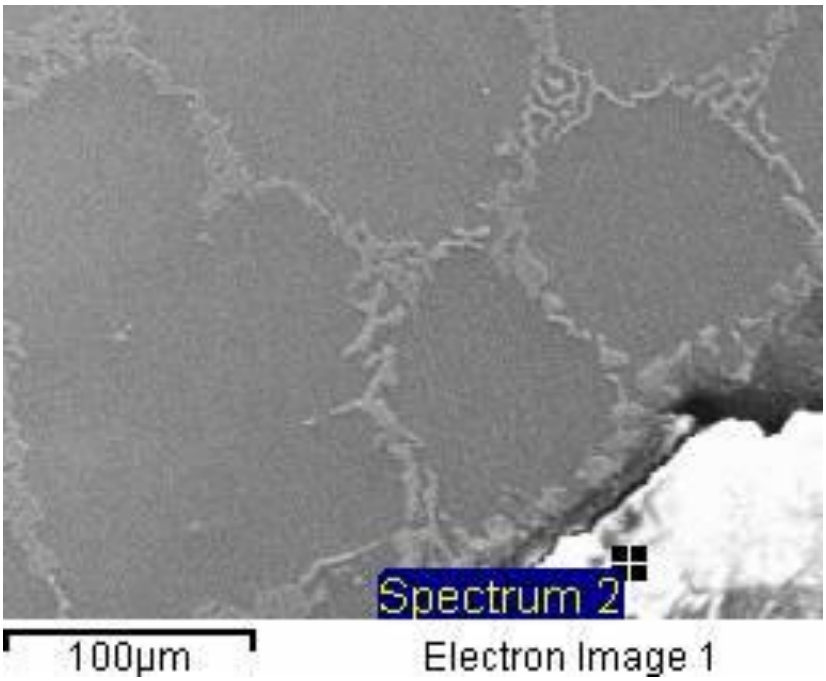

Figure 88: Small spacer foam magnesium JEOL SEM, 400x, WD 16mm, 15vK. Image is showing a section of magnesium next to a pore spectrum 2.

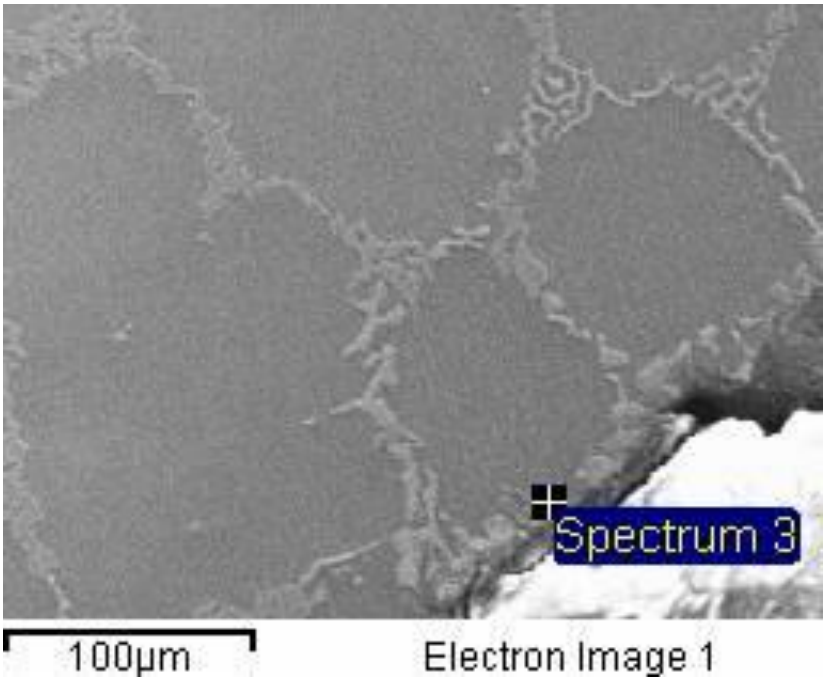

Figure 89: Small spacer foam magnesium JEOL SEM, 400x, WD 16mm, 15vK. Image is showing a section of magnesium next to a pore spectrum 3.

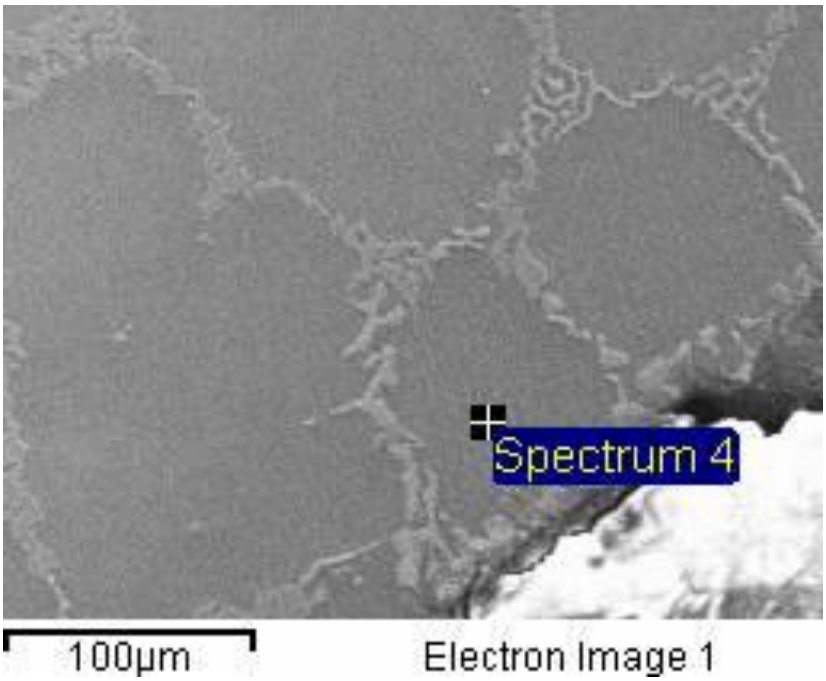

Figure 90: Small spacer foam magnesium JEOL SEM, 400x, WD 16mm, 15vK. Image is showing a section of magnesium next to a pore spectrum 4.

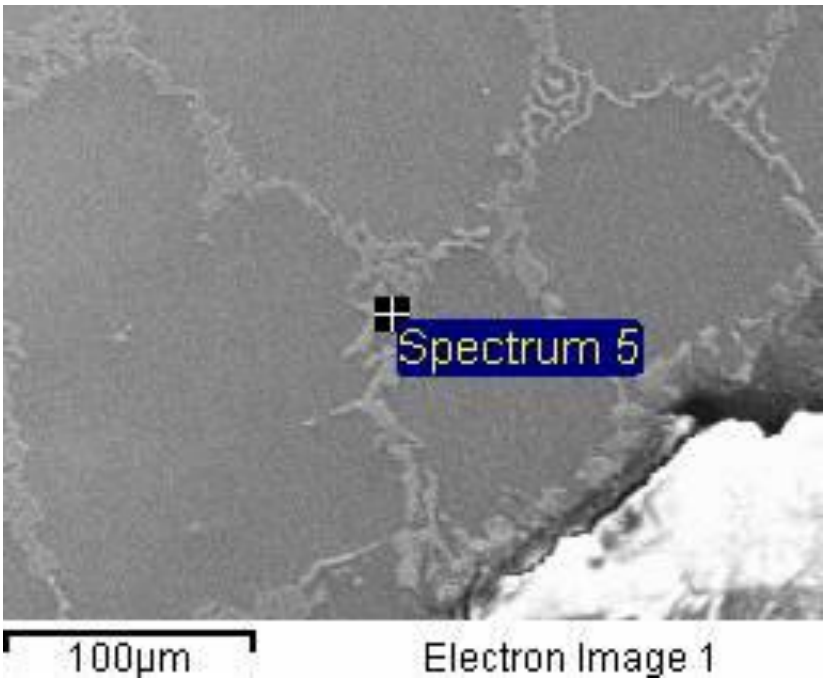

Figure 91: Small spacer foam magnesium JEOL SEM, 400x, WD 16mm, 15vK. Image is showing a section of magnesium next to a pore spectrum 5.

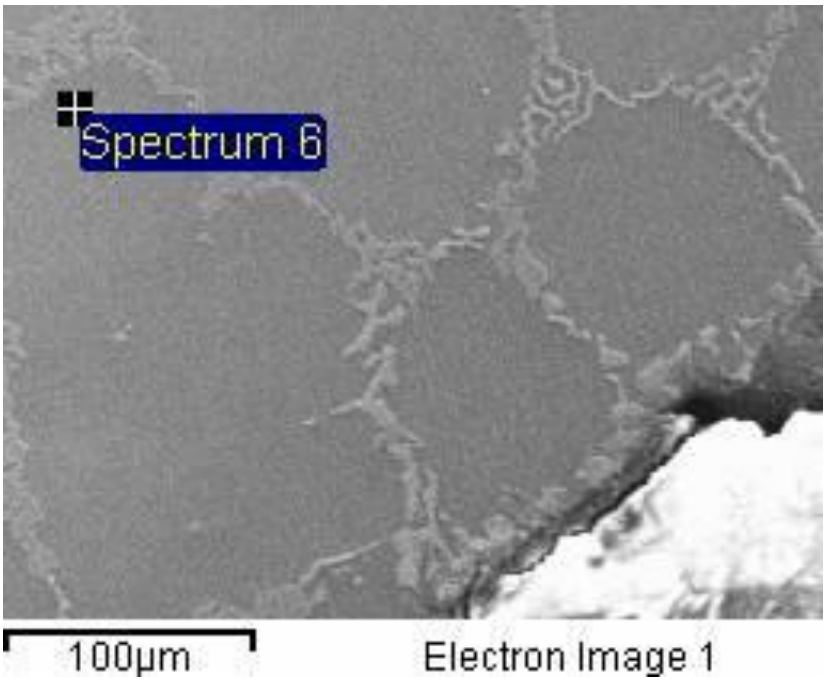

Figure 92: Small spacer foam magnesium JEOL SEM, 400x, WD 16mm, 15vK. Image is showing a section of magnesium next to a pore spectrum 6.

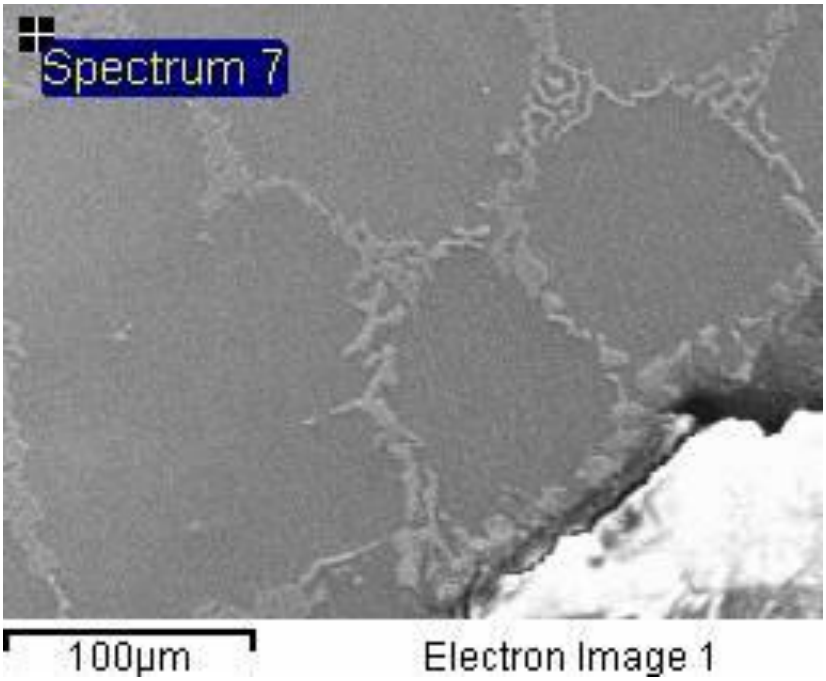

Figure 93: Small spacer foam magnesium JEOL SEM, 400x, WD 16mm, 15vK. Image is showing a section of magnesium next to a pore spectrum 7.

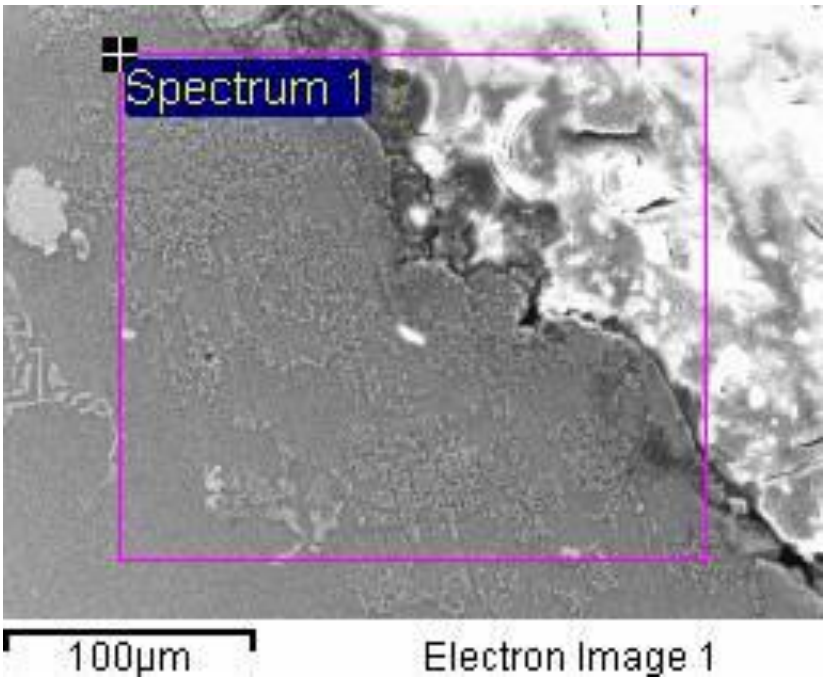

Figure 94: Small spacer foam magnesium JEOL SEM, 400x, WD 16mm, 15vK. Image is showing a section of magnesium next to a pore spectrum 1.

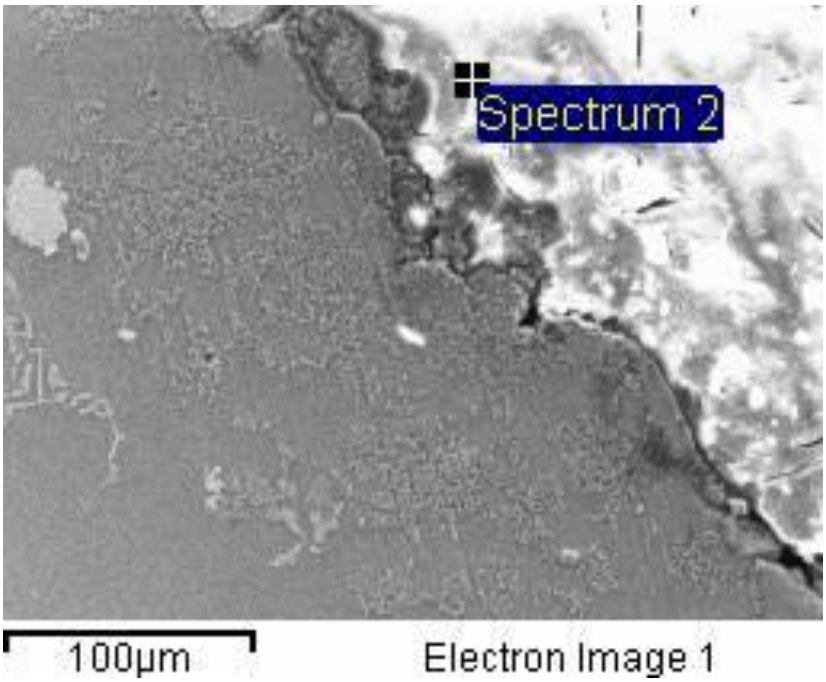

Figure 95: Small spacer foam magnesium JEOL SEM, 400x, WD 16mm, 15vK. Image is showing a section of magnesium next to a pore spectrum 2.

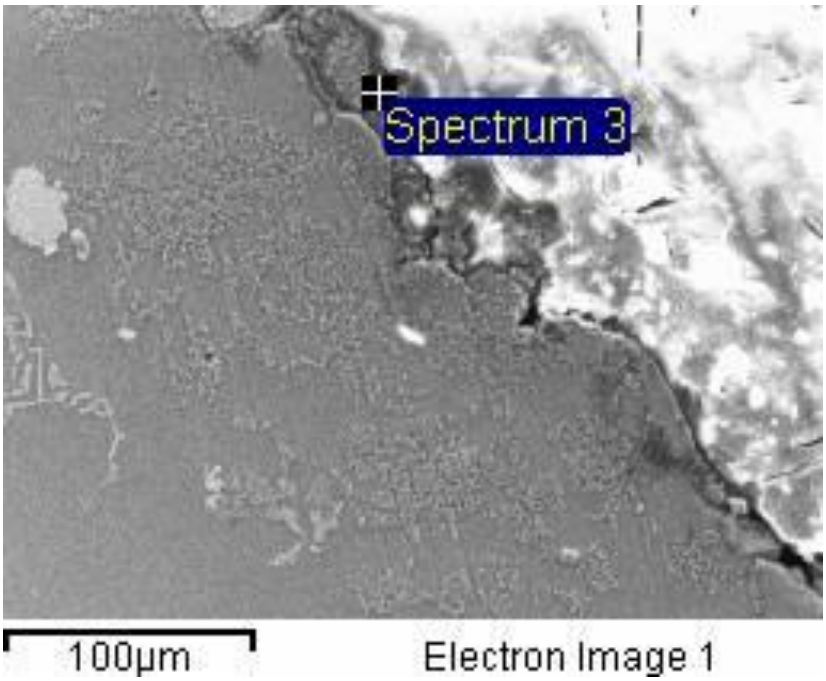

Figure 96: Small spacer foam magnesium JEOL SEM, 400x, WD 16mm, 15vK. Image is showing a section of magnesium next to a pore spectrum 3.

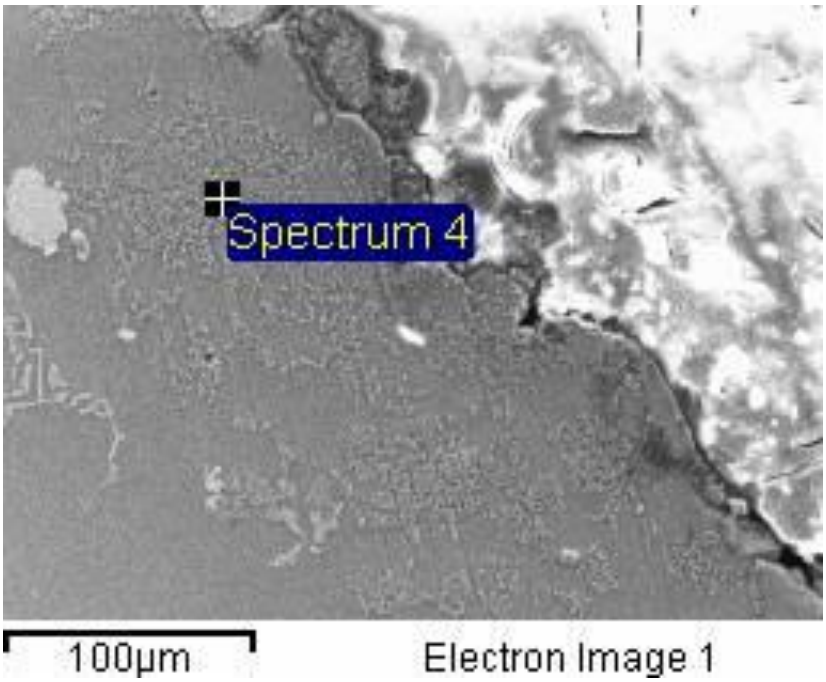

Figure 97: Small spacer foam magnesium JEOL SEM, 400x, WD 16mm, 15vK. Image is showing a section of magnesium next to a pore spectrum 4.

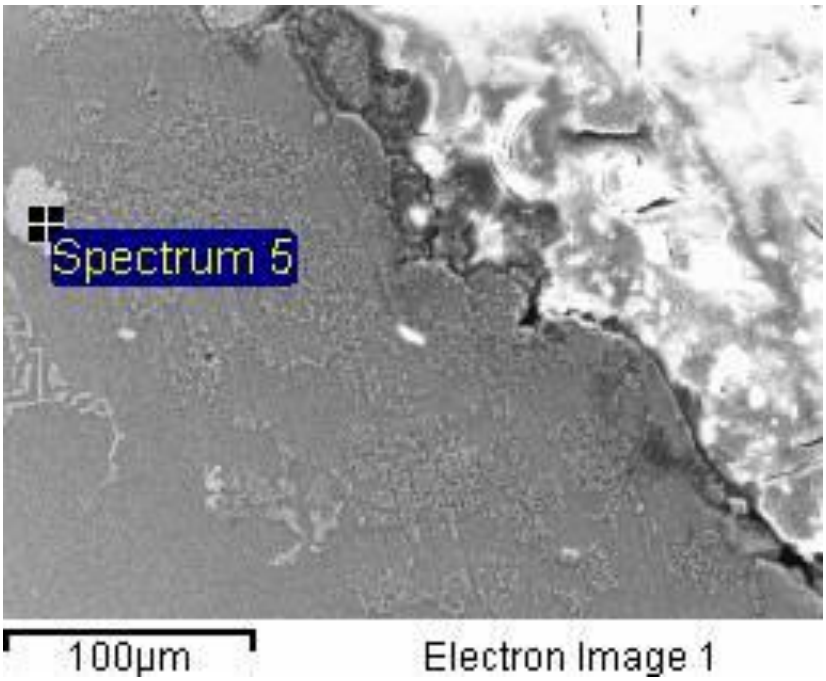

Figure 98: Small spacer foam magnesium JEOL SEM, 400x, WD 16mm, 15vK. Image is showing a section of magnesium next to a pore spectrum 5.

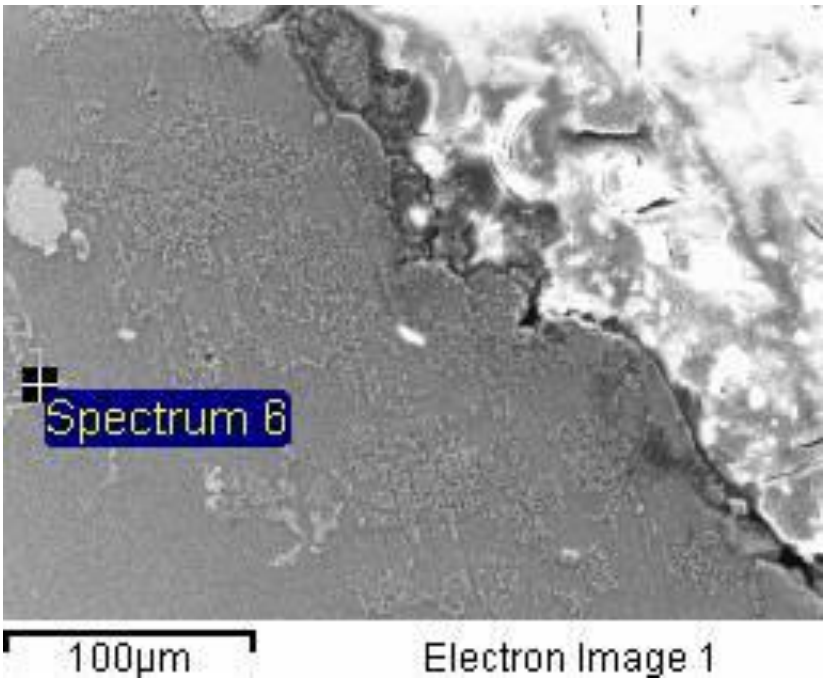

Figure 99: Small spacer foam magnesium JEOL SEM, 400x, WD 16mm, 15vK. Image is showing a section of magnesium next to a pore spectrum 6.